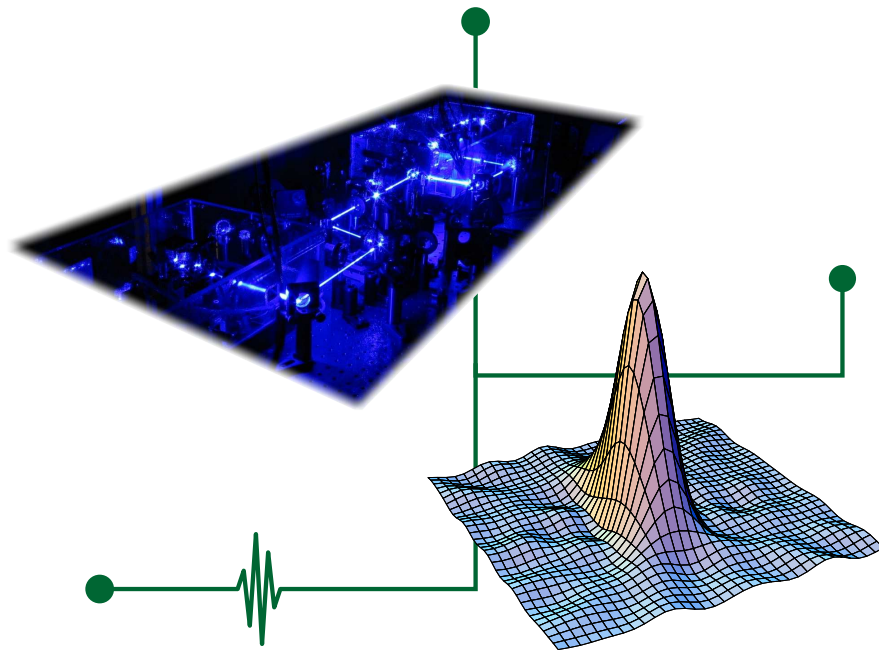


# Nonclassical light source for quantum networks



Master thesis  
by  
Jonas Schou Neergaard-Nielsen

February 2005  
University of Copenhagen





Thesis for the degree of  
Candidatus Scientiarum in Physics

Niels Bohr Institute  
Faculty of Science  
University of Copenhagen

Supervisor:  
Prof. Eugene S. Polzik,  
Danish National Research Foundation  
Center for Quantum Optics



# Preface

I started working on my master project in the QUANTOP lab at the Niels Bohr Institute in September 2003. The group had moved from Århus to Copenhagen early that year, and while the other experiments were rebuild from scratch, the EPR-light optical table was moved with all the optics still in place (see pictures below). The only thing missing was the experimentalists! So, having been out of operation for about a year, I got the task of revitalizing the experiment to its full glory as a prime source of frequency-tunable and narrowband (that is, atoms-friendly) squeezed and EPR-entangled light. In addition to that, a quite ambitious goal was to extend it to also produce atoms-friendly single photons.

Starting out as a rookie of experimental physics, all alone with an overwhelming optical setup - with plenty of helping assistance from other members of the group, though - things naturally progressed in a, well... natural pace, where I learned about many of the small intricacies of the experiment through true first-hand experience. After half a year I observed my first squeezing, and shortly after, in May 2004, Christian Hettich joined the experiment as a post.doc. This of course boosted the progress, but we were soon struck by bad luck; a broken main laser, causing no experiments for three months. This gave us time to think up the new single photon source, and after the laser got back, things speeded up again so that we are now close to having the EPR light back, the photon business is taking shape, and we have had time for characterizing the squeezed light by a method not used before in our group, namely quantum homodyne tomography. Thus, even though I did not accomplish everything I set out to do, it has still been a rather fruitful year and a half (barely), all things considered.

The level of the thesis is aimed at an audience with at least a Bachelor-level background in physics, and especially quantum mechanics. No knowledge of quantum optics is presupposed, but it would probably not hurt.

My project has been very experimental since most of the work is based on either known theory or formulas derived in earlier theses on this experiment. The present thesis reflects this fact, being quite descriptive with a limited amount of theory. An exception is the derivation of the output properties of the optical parametric oscillator which I have carried out in some detail based on a slightly shorter derivation in a classical paper on that subject. This I did because I have not been able to find an easily understandable but fulfilling treatment anywhere else. My hope is that I got a little closer to that end.

There are a number of people who deserve my acknowledgements for helping me through the 15 months in a dark basement and the last 2 months in an almost as dark office. I sincerely apologize to anyone I might have forgot in the following list.

First of all I would like to thank my supervisor Eugene Polzik for entrusting me with this fairly complex experiment and for creating a very lively and inspiring research environment with plenty of input from outside our little world in the basement. Secondly, I have really appreciated working together with all the people of the QUANTOP lab, with whom I have also enjoyed many entertaining hours of sport, games, good eating, partying - and not to forget, tons of cake! They are, in order of appearance (more or less): Brian Julsgaard, Plamen Petrov, Daniel Oblak, Jacob Sherson, Carlos Garrido Alzar, Jörg Müller, Andrew Hilliard, Aśka Dolińska, Christian Hettich, Christina Olausson, Rasmus Olsson and Bo Nielsen. Special thanks to Christina, Rasmus, Daniel and Christian for useful comments on my thesis - and also to Christian for teaching me experimental tricks and broadening my understanding of what is going on. Further thanks to a former member of the lab, Jens Lykke Sørensen in Århus, for lots of practical advice on the experiment. I would also like to thank the laserlab/cakelab/atomic physics group at the H. C. Ørsted Institute for various battles in a friendly atmosphere and for an excellent trip to Paris in February 2004, and in particular I am thankful to Jan Thomsen for introducing me in a very enthusiastic way to the field of experimental quantum optics. On a social level, life at the physics study was made a lot more interesting by the frequent lunch breaks together with Trine Facius and Toke Andersson, and by Christmas lunches, Rustur<sup>n</sup>, etc. with the rest of the students from year '99. Finally, I send my warmest thanks to my family who have always been very supportive of me - and who have at least *tried* to understand what crazy stuff I am doing in the dark basement.

*Jonas Schou Neergaard-Nielsen  
Copenhagen, February 2005*



*A portable source of nonclassical light  
Pictures from Århus*

**Work hard  
Get results  
No mistakes**

*QUANTOP motto,  
by Daniel Oblak*



# Contents

<b>1</b>	<b>Introduction</b>	<b>1</b>
<b>2</b>	<b>Quantum theory of light</b>	<b>5</b>
2.1	Quantization of the electromagnetic field . . . . .	5
2.1.1	The classical field . . . . .	5
2.1.2	The quantized electric field . . . . .	6
2.2	Formalized description of light . . . . .	7
2.2.1	Field quadratures . . . . .	7
2.2.2	Fock states . . . . .	8
2.2.3	Coherent states . . . . .	8
2.3	Representations of general quantum optical states . . . . .	9
2.3.1	The density matrix . . . . .	9
2.3.2	The Wigner function . . . . .	10
2.4	Squeezed states . . . . .	12
2.4.1	Formal description of squeezed states . . . . .	13
2.4.2	Wigner function . . . . .	14
2.4.3	Physical generation . . . . .	15
2.4.4	Photon number and statistics . . . . .	16
2.4.5	Brief historical overview . . . . .	16
<b>3</b>	<b>Squeezing tools</b>	<b>17</b>
3.1	Nonlinear interactions . . . . .	17
3.1.1	Nonlinear materials . . . . .	17
3.1.2	Phase matching . . . . .	18
3.1.3	Focused beams . . . . .	21
3.2	Optical parametric oscillator . . . . .	22
3.2.1	Cavity equations . . . . .	24
3.2.2	Broadband equations of motion for the cavity mode . . . . .	26
3.2.3	The output field . . . . .	27
3.2.4	Quadrature fluctuations . . . . .	29
<b>4</b>	<b>Squeezing experiment</b>	<b>33</b>
4.1	Overview . . . . .	33
4.2	Frequency doubling . . . . .	36
4.2.1	Cavity design . . . . .	36
4.2.2	Crystal nonlinearity . . . . .	37
4.2.3	Losses . . . . .	38
4.2.4	Phase matching, thermal problems . . . . .	39

4.2.5	Performance . . . . .	39
4.3	OPO . . . . .	40
4.3.1	Design . . . . .	40
4.3.2	Parametric gain . . . . .	42
4.4	Measuring squeezing . . . . .	42
4.4.1	Homodyne detector . . . . .	42
4.4.2	Inefficient detection . . . . .	44
4.4.3	Spectrum analyzer . . . . .	44
4.4.4	5 dB squeezed light . . . . .	45
4.4.5	Stability . . . . .	46
<b>5</b>	<b>Quantum state tomography</b>	<b>49</b>
5.1	Introduction . . . . .	49
5.1.1	Motivation . . . . .	49
5.1.2	Presentation of the idea . . . . .	50
5.2	Noise traces . . . . .	50
5.2.1	Electronic noise, coherent vacuum and bright coherent beam . . . . .	51
5.2.2	Squeezed vacuum . . . . .	52
5.2.3	Bright squeezed state . . . . .	54
5.3	Inverse Radon transformation . . . . .	55
5.3.1	The reconstruction method . . . . .	55
5.3.2	Gallery of reconstructions . . . . .	57
5.3.3	Optimization . . . . .	60
5.4	Density matrices . . . . .	63
5.4.1	Two reconstruction procedures . . . . .	63
5.4.2	Reconstructed density matrices . . . . .	64
<b>6</b>	<b>Future plans</b>	<b>69</b>
6.1	EPR entangled light beams . . . . .	69
6.1.1	NDOPO output . . . . .	70
6.1.2	Two-mode squeezing . . . . .	71
6.1.3	Entanglement . . . . .	72
6.1.4	Experimental setup . . . . .	74
6.2	Single photons . . . . .	76
6.2.1	Requirements . . . . .	76
6.2.2	Implementation: NDOPO far below threshold . . . . .	78
6.2.3	Planned setup . . . . .	80
<b>7</b>	<b>Summary and outlook</b>	<b>87</b>
<b>A</b>	<b>Properties of the squeezed states</b>	<b>89</b>
<b>B</b>	<b>Various OPO equations</b>	<b>93</b>

# Chapter 1

## Introduction

Throughout the second half of the last century, the increase in computing and communication speed and capacity has been explosive, powered by engineer's incredible ability to build ever smaller electronic circuits. With today's pace, however, the chips will soon become so small that they approach the quantum barrier where it will become basically impossible to decrease the size of traditional electronics further and with that the speed of information processing.

This is where quantum information enters the picture. Instead of just seeing the laws of quantum mechanics as an impassable obstacle, they can be employed for an altogether different way of treating information, which may eventually lead to faster-than-classical computing. The theory of quantum information is based on two fundamental concepts of quantum mechanics: Superposition and *entanglement*<sup>1</sup>. Analogous to the classical bit, the basic unit of quantum information is the *qubit*, but whereas the former can be in a state of *either* 0 or 1, the qubit can be in *both* 0 and 1 at the same time, by the principle of superposition. Exploitation of this fact can in some cases yield computations which are exponentially faster than what is possible classically.

The theory of quantum information is rather new and it is being developed rapidly. On the experimental side, many different branches of physics see progress towards the ultimate goal of building a useful quantum computer, and even though its realization may still be many years ahead of us, it is certainly not science fiction anymore. For a nice review of quantum computation and information, see Bennett and DiVincenzo [2000].

Once we have a quantum computer, the next item on our wish list will of course be a quantum internet! For that, it should be possible to efficiently transfer quantum information over large distances; we need *quantum communication*, and it will be necessary to have a way of storing the information for some time to process it; we need a *quantum memory*. Having several separated quantum memory nodes interconnected by quantum communication channels would constitute a *quantum network*.

A fundamental issue in quantum information is *decoherence*. Coherent quantum superpositions are fragile and may easily decohere into classical states through interaction with the environment, which destroys the information encoded in the superposition state. One of the greatest technical challenges in building a quantum network

---

<sup>1</sup>More on entanglement in section 6.1 of this thesis.

is thus to battle such decoherence in all parts of the network; in the transmission channel, in the memory unit, and in the interface between them.

As for the physical implementation, the obvious way of transmitting qubits is by encoding them into quantum states of light, since for light the decoherence per traveled distance is low, plus there is an already extensive established infrastructure. A scheme for all-optical quantum computation has been devised [Knill et al., 2001], but the timescale of coherence for light is short, so, with a slower decoherence, matter will be better suited for long lived memory. At present, the physical systems that appear to be most feasible for a quantum memory involves atoms, either individually [Cirac et al., 1997] or in larger ensembles [Kozhekin et al., 2000], because of the well-controlled interaction between light and atoms and the possibility to isolate the atoms from the environment to a certain extent [Monroe, 2002].

Techniques that might be essential for a quantum network include *quantum teleportation* [Bennett et al., 1993] and *quantum repeaters* [Briegel et al., 1998]. Teleportation is an alternative to using “flying qubits” for the quantum information transfer. It requires an entanglement connection to be set up between the two nodes, which mediates the information transfer in cooperation with classical communication. Such a distant entanglement can be created between large atomic ensembles, as demonstrated by Julsgaard et al. [2001]. Because of decoherence it is hard to establish entanglement directly between widely separated nodes, but quantum repeaters can reinforce the entanglement, allowing for larger-scale networks. A scheme for quantum repeaters involving atomic ensembles has been proposed [Duan et al., 2001]. For more complex quantum networks, also the connection through entanglement between more than just two parties might prove useful [van Loock and Braunstein, 2000].

An operating quantum computer or communication network may not be realizable in the near future, but crucial advances towards that end are the development and testing of the individual elements. The research of the QUANTOP lab is heading for the development of quantum memories in macroscopic atomic ensembles - more specifically in the collective spin states of the atoms - and for quantum interfaces between light and atoms. A quantum memory for coherent (classical) light states has recently been demonstrated [Julsgaard et al., 2004]. Nonclassical light states, however, are a lot more fragile and susceptible to decoherence than coherent states. so to truly claim a quantum memory viable for any quantum state of light, it must be proven to be capable of the coherent storage and the subsequent reversible readout of a nonclassical light state.

The experimental work underlying this thesis is aimed at the production of such nonclassical states of light with the specific purpose of testing such light-atom interfaces. The main subject of the thesis is *squeezed light*, a nonclassical state which in a certain sense is more “quiet” than classical states such as those of laser light or the vacuum field. Besides a fundamental relevance in quantum mechanics, squeezed light states can have several practical applications, and many interesting experiments on squeezing has been and are still being carried out [Bachor and Ralph, 2004]. For our purpose, however, with experiments on quantum memory and communication in mind, our primary interest in the squeezed light is as a (major) step on the road towards even more interesting and highly nonclassical light states such as entangled beams and single photons. These will in turn be invaluable for the testing of the devices developed elsewhere in the lab.

The thesis is organized as follows. Chapter 2 introduces the most basic theory about the quantum description of light and squeezed light in particular. The theoretical foundations of the experiment continues in chapter 3, describing nonlinear interactions and the optical parametric oscillator - the tools used for squeezing the field. The experimental setup is discussed in chapter 4 as well as some of the measurements performed. Further measurements are presented in chapter 5, which is devoted to a special technique called *optical homodyne tomography* for determining the full quantum state of the probed light. A fairly extensive final chapter 6 describes in detail the immediate extensions of the experiment that are already underway, which will make it capable of producing entangled beams and single photons. The outlook towards future interplay with other experiments of the group to test light-atom interfaces is briefly discussed after the summary in chapter 7.



## Chapter 2

# Quantum theory of light

A thesis within the field of quantum optics should naturally begin by describing the quantum theory of light, which is the basis of most of the interesting effects we observe and discuss here. Special emphasis is put on the Wigner function representation and squeezed states of the electromagnetic field, but we will start out with the fundamentals:

### 2.1 Quantization of the electromagnetic field

#### 2.1.1 The classical field

The steps taken in this section are following Scully and Zubairy [1997].

The wave equation for an electric field in vacuum, derived from Maxwell's equations is

$$\nabla^2 \mathbf{E}(\mathbf{r}, t) - \frac{1}{c^2} \frac{\partial^2 \mathbf{E}(\mathbf{r}, t)}{\partial t^2} = 0. \quad (2.1)$$

A solution to this is given by

$$\mathbf{E}(\mathbf{r}, t) = \sum_{\mathbf{k}} \hat{\epsilon}_{\mathbf{k}} E_{0,\mathbf{k}} \left( \alpha_{\mathbf{k}} e^{-i(\omega_{\mathbf{k}} t - \mathbf{k} \cdot \mathbf{r})} + \alpha_{\mathbf{k}}^* e^{i(\omega_{\mathbf{k}} t - \mathbf{k} \cdot \mathbf{r})} \right), \quad (2.2)$$

where the spatial mode of the field is an expansion of plane waves with wave vector  $\mathbf{k}$ , polarization vector  $\hat{\epsilon}_{\mathbf{k}}$ , mode amplitude  $\alpha_{\mathbf{k}}$ , and angular frequency  $\omega_{\mathbf{k}} = 2\pi/\lambda_{\mathbf{k}} = kc$ , with  $k = |\mathbf{k}|$ . The direction of the wave vector is the direction of propagation of that individual plane wave. Gauss's law implies that  $\mathbf{k} \cdot \hat{\epsilon}_{\mathbf{k}} = 0$ , which means that the field is transverse; it is polarized in the plane perpendicular to the direction of propagation.  $E_{0,\mathbf{k}}$  is a factor extracted from the field strength, leaving the  $\alpha$ 's dimensionless, and, anticipating the quantization, we assign it the value

$$E_{0,\mathbf{k}} = \sqrt{\frac{\hbar \omega_{\mathbf{k}}}{2\epsilon_0 V}}. \quad (2.3)$$

Here  $V$  is the volume of the cavity in which the field is defined. The definition of the electric field in terms of discrete cavity modes is an important technicality, but not something we want to delve further into. Instead we will simplify things a bit

by restricting ourselves to a monochromatic plane wave, that is, a single-mode field, thus getting rid of the summation and mode indices in (2.2):

$$\mathbf{E}(\mathbf{r}, t) = \varepsilon E_0 \left( \alpha e^{-i(\omega t - \mathbf{k} \cdot \mathbf{r})} + \alpha^* e^{i(\omega t - \mathbf{k} \cdot \mathbf{r})} \right). \quad (2.4)$$

The field also has a magnetic component which we disregard in this context, except when calculating the total energy of the field: For a plane wave, the magnetic field is simply [Griffiths, 1999, sect. 9.2.2]

$$\mathbf{B}(\mathbf{r}, t) = \frac{1}{c} \frac{\mathbf{k}}{k} \times \mathbf{E}(\mathbf{r}, t). \quad (2.5)$$

The energy of the electromagnetic field is given by

$$H = \int_V \left( \frac{\epsilon_0}{2} \mathbf{E}^2 + \frac{1}{2\mu_0} \mathbf{B}^2 \right) dV, \quad (2.6)$$

which for the plane wave becomes

$$H = \epsilon_0 \int_V \mathbf{E}^2 dV \quad (2.7)$$

$$= \epsilon_0 \int_V E_0^2 \left( \alpha^* \alpha + \alpha \alpha^* + (\alpha^*)^2 e^{i(\omega t - \mathbf{k} \cdot \mathbf{r})} + \alpha^2 e^{-i(\omega t - \mathbf{k} \cdot \mathbf{r})} \right) dV \quad (2.8)$$

$$= \frac{\hbar\omega}{2} (\alpha^* \alpha + \alpha \alpha^*) = \hbar\omega \alpha^* \alpha. \quad (2.9)$$

Here we have used that the optical frequencies are so high that any measurement of the field intensity will average over several optical cycles, yielding the last two terms in (2.8) zero.

### 2.1.2 The quantized electric field

The quantization of the field is performed by identifying the mode amplitudes in (2.4) with the annihilation and creation operators of the quantum mechanical harmonic oscillator:<sup>1</sup>

$$E(\mathbf{r}, t) = E_0 \left[ \hat{a} e^{-i(\omega t - \mathbf{k} \cdot \mathbf{r})} + \hat{a}^\dagger e^{i(\omega t - \mathbf{k} \cdot \mathbf{r})} \right]. \quad (2.10)$$

For simplicity we are now only considering the scalar value of the field. The annihilation and creation operators serve to decrease and increase the excitation of the field mode, respectively. They obey the commutation relation

$$[\hat{a}, \hat{a}^\dagger] = 1. \quad (2.11)$$

From (2.9) the Hamiltonian of the field becomes:

$$\hat{H} = \frac{\hbar\omega}{2} (\hat{a}^\dagger \hat{a} + \hat{a} \hat{a}^\dagger) = \hbar\omega \left( \hat{a}^\dagger \hat{a} + \frac{1}{2} \right). \quad (2.12)$$

The  $\hat{a}^\dagger \hat{a}$  is the number operator  $\hat{n}$ , giving the number of quanta (photons) of energy  $\hbar\omega$  in the field. In the case of vacuum ( $\langle \hat{n} \rangle = 0$ ), there is still a small energy present

<sup>1</sup>The proper way of quantizing the field is by introducing the canonical variables  $q$  and  $p$  of the classical harmonic oscillator and then quantize through these, but this is a more lengthy affair. Mandel and Wolf [1995], for instance, addresses this in detail.

- the zero point contribution. This term reflects the fact that according to the Heisenberg uncertainty principle there must be a minimum of fluctuations of a field, even for vacuum. The vacuum fluctuations are what really sets the quantum description of light apart from the classical one. They are responsible for such effects as the spontaneous emission of light from atoms, the Lamb shift, and the Casimir Force [Scully and Zubairy, 1997], and they play the leading role in this thesis.

## 2.2 Formalized description of light

### 2.2.1 Field quadratures

The annihilation and creation operators are very useful for the description of many quantum phenomena. However, they are not themselves Hermitian and therefore not observables. We will need the two linear superpositions

$$\hat{q} = \frac{\hat{a} + \hat{a}^\dagger}{\sqrt{2}}, \quad \hat{p} = \frac{\hat{a} - \hat{a}^\dagger}{i\sqrt{2}}, \quad (2.13)$$

which are the dimensionless position and momentum operators of the harmonic oscillator, respectively. These operators are Hermitian and for states of light they can be observed with relative ease using homodyne detection - see section 4.4.1.

The electric field (2.10) can be rewritten in terms of these new operators:

$$\mathbf{E}(\mathbf{r}, t) = \sqrt{2}E_0 [\hat{q} \cos(\omega t - \mathbf{k} \cdot \mathbf{r}) + \hat{p} \sin(\omega t - \mathbf{k} \cdot \mathbf{r})]. \quad (2.14)$$

Thus,  $\hat{q}$  and  $\hat{p}$  are the amplitudes of the two components of the electric field having a  $90^\circ$  phase difference - the so-called quadratures of the field. Hence  $\hat{q}$  and  $\hat{p}$  are termed the *quadrature operators*. In the literature there are several other notations for them:  $X_1/X_2$ ,  $X^+/X^-$ ,  $X1/X2$ ,  $X/Y$ ,  $X/P$ , sometimes in small instead of capital letters. Also, they can be defined with a factor of 1 or  $1/2$  instead of  $1/\sqrt{2}$ . It will be useful to introduce the generalized quadrature operator  $\hat{q}_\theta$ :

$$\hat{q}_\theta = \frac{1}{\sqrt{2}}(\hat{a}e^{-i\theta} + \hat{a}^\dagger e^{i\theta}) = \hat{q} \cos \theta + \hat{p} \sin \theta, \quad (2.15)$$

which is just a rotation through the angle  $\theta$  of the standard quadratures  $\hat{q} = \hat{q}_0$ ,  $\hat{p} = \hat{q}_{\pi/2}$ .

The commutator relation for  $\hat{q}$  and  $\hat{p}$  is

$$[\hat{q}, \hat{p}] = i, \quad (2.16)$$

so the uncertainty relation becomes

$$\langle (\Delta \hat{q})^2 \rangle \langle (\Delta \hat{p})^2 \rangle \geq \frac{1}{4} |\langle [\hat{q}, \hat{p}] \rangle|^2 = \frac{1}{4}. \quad (2.17)$$

The variances occurring in (2.17) are defined for an observable  $\hat{A}$  as

$$\text{Var} \hat{A} \equiv \langle (\Delta \hat{A})^2 \rangle = \langle (\hat{A} - \langle \hat{A} \rangle)^2 \rangle = \langle \hat{A}^2 \rangle - \langle \hat{A} \rangle^2, \quad (2.18)$$

and is also called the uncertainty, dispersion or noise. A quantum state for which the equal sign applies is called a *minimum uncertainty state*. If the uncertainties are equally distributed among the quadratures, the minimum variance is  $1/2$ , known as the *standard quantum limit* (SQL).

### 2.2.2 Fock states

Two of the most important examples of quantum states of light are the *coherent states* and the *Fock states* (or number states, as they are also called).

The Fock states are the eigenstates of the number operator  $\hat{n}$  and therefore also energy eigenstates, cf. (2.12):

$$\hat{n} |n\rangle = n |n\rangle, \quad \hat{H} |n\rangle = \hbar\omega(\hat{n} + \frac{1}{2}) |n\rangle = \hbar\omega(n + \frac{1}{2}) |n\rangle = E_n |n\rangle. \quad (2.19)$$

For  $n = 0$  we have the vacuum state  $|0\rangle$  which is the ground state of the energy. The actions of the annihilation and creation operators on a Fock state are

$$\hat{a} |n\rangle = \sqrt{n} |n-1\rangle, \quad \hat{a}^\dagger |n\rangle = \sqrt{n+1} |n+1\rangle, \quad (2.20)$$

that is, lowering or raising the excitation of the field as already mentioned. This excitation of the field is commonly referred to as the number of photons when interpreting the field in a particle picture.

The photon number and the phase are conjugate variables, so since the energy (photon number) in a Fock state is exactly determined, the phase is completely undetermined - the state is rotationally invariant in phase space, the space with coordinates  $\alpha = |\alpha|e^{i\theta} = (q+ip)/\sqrt{2}$ . However, the Fock state is not a minimum uncertainty state:

$$\langle(\Delta\hat{q}_\theta)^2\rangle = \langle n|\hat{q}_\theta^2|n\rangle - \langle n|\hat{q}_\theta|n\rangle^2 = \frac{2n+1}{2}, \quad (2.21)$$

which is greater than  $1/2$ , except for vacuum.

### 2.2.3 Coherent states

The Fock state is highly non-classical; the classical description of light knows nothing about quanta of energy. In contrast to this is the coherent state, which is the quantum state that most resembles ordinary, low noise laser light, which in this context is classical.

One definition of the coherent state  $|\alpha\rangle$  is that it is an eigenstate of the annihilation operator with eigenvalue  $\alpha$ ,

$$\hat{a} |\alpha\rangle = \alpha |\alpha\rangle \quad (2.22)$$

- the removal of a single photon from a laser beam does not alter its state.

It is possible to write  $|\alpha\rangle$  as an expansion in Fock states (they form a complete set) with the result

$$|\alpha\rangle = e^{-|\alpha|^2/2} \sum_{n=0}^{\infty} \frac{\alpha^n}{\sqrt{n!}} |n\rangle. \quad (2.23)$$

The expression can be rewritten as

$$|\alpha\rangle = \hat{D}(\alpha) |0\rangle, \quad \text{with } \hat{D}(\alpha) \equiv e^{\alpha\hat{a}^\dagger - \alpha^*\hat{a}} \quad (2.24)$$

being a unitary operator called the displacement operator with the action of displacing the vacuum into the coherent state. [Mandel and Wolf, 1995, sect. 11.2,3]

The photon number probability in a coherent state is a Poissonian distribution

$$p_n = |\langle n|\alpha\rangle|^2 = \frac{|\alpha|^{2n}}{n!} e^{-|\alpha|^2}, \quad (2.25)$$

which has mean value and variance

$$\langle \hat{n} \rangle = \langle (\Delta \hat{n})^2 \rangle = |\alpha|^2 . \quad (2.26)$$

This mean photon number is also the intensity of the classical field with complex mode amplitude  $\alpha$  (2.4) except for a prefactor. In the same way, the expectation value of for instance the  $\hat{q}$  quadrature operator is the classical counterpart of the quadrature:

$$\langle \hat{q} \rangle = \langle \alpha | \frac{\hat{a} + \hat{a}^\dagger}{\sqrt{2}} | \alpha \rangle = \frac{\alpha + \alpha^*}{\sqrt{2}} . \quad (2.27)$$

This goes to show how the coherent state simulates the classical field. The variance of the quadrature operators is, using (2.11)

$$\begin{aligned} \langle (\Delta \hat{q}_\theta)^2 \rangle &= \langle \alpha | \hat{q}_\theta^2 | \alpha \rangle - \langle \alpha | \hat{q}_\theta | \alpha \rangle^2 = \\ &= \frac{1}{2} [1 + \alpha^2 e^{-2i\theta} + \alpha^{*2} e^{2i\theta} + 2|\alpha|^2] - \frac{1}{2} [\alpha^2 e^{-2i\theta} + \alpha^{*2} e^{2i\theta} + 2|\alpha|^2] = \frac{1}{2} , \end{aligned} \quad (2.28)$$

so the coherent state is always a minimum uncertainty state, irrespectively of the amplitude of the state. Furthermore, the uncertainty is equal for all quadrature phases.

## 2.3 Representations of general quantum optical states

### 2.3.1 The density matrix

From basic quantum mechanics, we know that a pure quantum state can be described by its wave function  $|\psi\rangle$ , while in general, a mixed state (a statistical mixture of pure states) is described by the *density operator*

$$\hat{\rho} = \sum_i p_i |\psi_i\rangle \langle \psi_i| , \quad (2.29)$$

where  $p_i$  is the contribution (in terms of probability) of the pure state  $|\psi_i\rangle$  to the total state. For a pure state, the density operator is simply  $|\psi\rangle \langle \psi|$ . The density operator contains all information obtainable about the state - it is a complete description [Sakurai, 1994]. The expectation value of any operator  $\hat{A}$  is given by  $\langle \hat{A} \rangle = \text{Tr} \hat{\rho} \hat{A}$ .

The density operator can be represented in any basis. For our purpose, the representation in terms of Fock states is the most relevant:

$$\hat{\rho} = \sum_{m,n} |m\rangle \langle m| \hat{\rho} |n\rangle \langle n| = \sum_{m,n} \rho_{mn} |m\rangle \langle n| . \quad (2.30)$$

$\rho_{mn} = \langle m | \hat{\rho} | n \rangle$  is the *density matrix* in the Fock state representation. The diagonal elements of this matrix are the probabilities  $p_n$  of observing  $n$  photons in the state (in the quantum optics context):

$$p_n = \langle n | \hat{\rho} | n \rangle = \rho_{nn} . \quad (2.31)$$

### 2.3.2 The Wigner function

Another way of representing quantum mechanical states, very useful for our purpose, are representations in phase space by distribution functions. We will pay particular attention to the *Wigner function*, which is a phase space distribution function that behaves almost like a classical probability distribution. It is defined in the basis of position wavefunctions<sup>2</sup> as [Wigner, 1932]

$$W(q, p) = \frac{1}{2\pi} \int dy e^{iyp} \left\langle q - \frac{y}{2} \left| \hat{\rho} \left| q + \frac{y}{2} \right. \right. \right\rangle, \quad (2.32)$$

that is, it can be calculated from the density matrix, and conversely, the density matrix can be calculated from the Wigner function - there is a one-to-one correspondence between them [Leonhardt, 1997, sect. 3.1.2], and thus also the Wigner function is a complete description of the state in question.

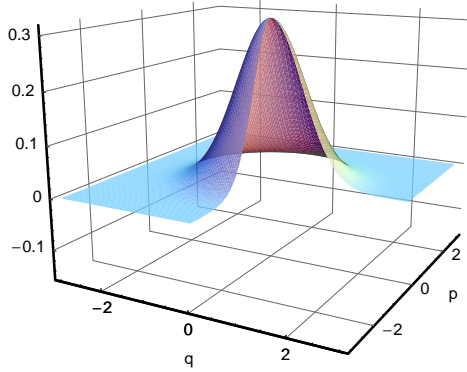


**Figure 2.1:** Wigner function for the vacuum state,  $W(q, p) = \frac{1}{\pi} e^{-(q^2+p^2)}$ .

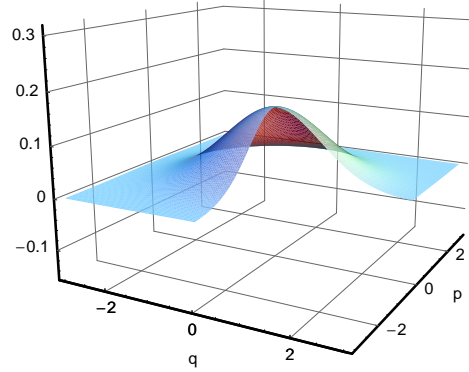


**Figure 2.2:** Wigner function for a thermal state,  $W(q, p) = \frac{1}{\pi} \tanh(\beta/2) e^{-(q^2+p^2) \tanh(\beta/2)}$  with  $\beta = \hbar\omega/k_B T$  (here  $\beta = 1$ ).

It can become negative for certain non-classical states such as the Fock states or a Schrödinger cat state [Monroe et al., 1996].<sup>3</sup> This of course disqualifies it as a proper probability distribution, however a number of other properties earns it its tag as a quasi-probability distribution. The most prominent feature is that it yields the correct *marginal distributions* for the quadratures:

$$\int_{-\infty}^{\infty} W(q, p) dp = \langle q | \hat{\rho} | q \rangle = \text{Pr}(q), \quad (2.33)$$

$$\int_{-\infty}^{\infty} W(q, p) dq = \langle p | \hat{\rho} | p \rangle = \text{Pr}(p). \quad (2.34)$$

$\text{Pr}(X)$  denotes the probability density of the variable  $X$ . The Wigner function itself is impossible to measure since we cannot measure the two quadratures simultaneously, but the marginal distributions are perfectly attainable through homodyne detection.

<sup>2</sup>The position wavefunctions obey  $\hat{q}|q\rangle = q|q\rangle$ .

<sup>3</sup>In fact, the Wigner function will have negative parts for all non-Gaussian pure states [Lütkenhaus and Barnett, 1995]

We are of course not limited to the  $q$  and  $p$  quadratures but can get the marginal distribution of any quadrature by rotating the coordinate system [Leonhardt, 1997, Bertrand and Bertrand, 1987]:

$$\Pr_{\theta}(q') = \int_{-\infty}^{\infty} W(q' \cos \theta - p' \sin \theta, q' \sin \theta + p' \cos \theta) dp'. \quad (2.35)$$

This means that we can measure the marginal distributions in a number of different directions and with a sufficient statistical material it is possible to obtain the Wigner function by the inversion of (2.35), called the *inverse Radon transformation*. It requires that we can produce a large number of identically prepared samples of the quantum state under inspection. We will do this in chapter 5 for our engineered states.

Another important property, reminiscent of a classical phase space probability density, is its potential for calculating expectation values for any operator by the overlap formula [Leonhardt, 1997]:

$$\langle \hat{A} \rangle = \text{Tr}(\hat{\rho} \hat{A}) = 2\pi \int_{-\infty}^{\infty} \int_{-\infty}^{\infty} W(q, p) W_A(q, p) dq dp, \quad (2.36)$$

where  $W_A(q, p)$  is the Wigner function obtained by replacing  $\hat{\rho}$  with  $\hat{A}$  in (2.32).

As a basic example of the calculation of a Wigner function, we can look at the vacuum state  $|0\rangle$ . We need the wavefunction in the coordinate ( $q$ ) representation. This is given by [Sakurai, 1994, sect. 2.3]

$$\psi_{vac}(q) = \frac{1}{\pi^{1/4}} \exp\left(-\frac{q^2}{2}\right). \quad (2.37)$$

The density operator is then  $\hat{\rho} = |\psi_{vac}\rangle \langle \psi_{vac}|$  and the Wigner function becomes

$$\begin{aligned} W(q, p) &= \frac{1}{2\pi} \int_{-\infty}^{\infty} dy e^{iyp} \left\langle q - \frac{y}{2} \middle| \psi_{vac} \right\rangle \left\langle \psi_{vac} \middle| q + \frac{y}{2} \right\rangle \\ &= \frac{1}{2\pi} \int_{-\infty}^{\infty} dy e^{iyp} \frac{1}{\pi^{1/4}} e^{-(q - \frac{y}{2})^2/2} \frac{1}{\pi^{1/4}} e^{-(q + \frac{y}{2})^2/2} \\ &= \frac{1}{2\pi^{3/2}} e^{-q^2} \int_{-\infty}^{\infty} dy e^{-(\frac{y^2}{4} - iyp)}. \end{aligned} \quad (2.38)$$

The last integral can be looked up in a table<sup>4</sup> to give  $2\sqrt{\pi}e^{-p^2}$ , so

$$W(q, p) = \frac{1}{\pi} e^{-q^2 - p^2}, \quad (2.39)$$

which is a Gaussian centered at (0,0) with variance 1/2.<sup>5</sup> A plot of the vacuum Wigner function is shown in figure 2.1. Other examples of Wigner functions are given with plots and formulas in figures 2.2, 2.3, 2.4; a thermal, a coherent, and a single-photon Fock state. The coherent and the thermal states are both members of the important class of Gaussian states, but where the coherent state is a pure state

<sup>4</sup>  $\int_{-\infty}^{\infty} e^{-(ax^2+bx+c)} dx = \sqrt{\frac{\pi}{a}} e^{(b^2-4ac)/4a}$ , [Spiegel and Liu, 1999].

<sup>5</sup> Remember the formula for a Gaussian function:  $f(q) = \frac{1}{\sqrt{2\pi\sigma^2}} e^{-(q-q_0)^2/2\sigma^2}$  in one dimension, and  $f(q, p) = \frac{1}{2\pi\sigma^2} e^{-[(q-q_0)^2+(p-p_0)^2]/2\sigma^2}$  in two dimensions, with center  $(q_0, p_0)$  and variance  $\sigma^2$ .

with minimum uncertainty, the thermal state is a mixed state with increasingly high noise for larger temperatures. The single-photon state is clearly non-Gaussian and also negative near the origin. The vacuum state can be considered as either a coherent state with no displacement, a thermal state with zero temperature or a Fock state with  $n = 0$ . Even more exotic states can be seen for example in Leonhardt [1997].

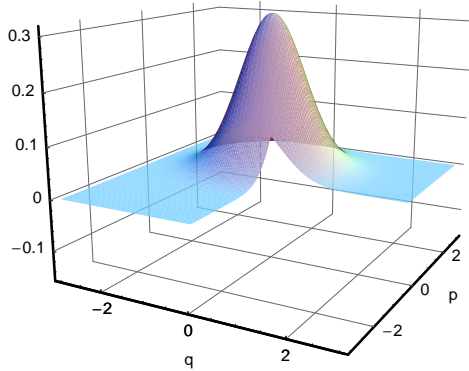


**Figure 2.3:** Wigner function for a weak coherent state,  $W(q, p) = \frac{1}{\pi} e^{-((q-q_0)^2 + (p-p_0)^2)}$ , centered at  $(q_0, p_0)$ .

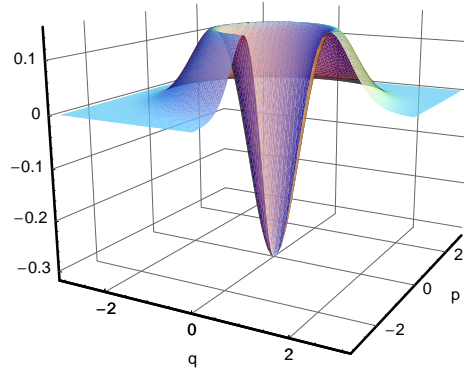


**Figure 2.4:** Wigner function for a one-photon Fock state,  $W(q, p) = \frac{1}{\pi} e^{-(q^2+p^2)}(2q^2 + 2p^2 - 1)$ . The negativity of the central part is a clear sign of a non-classical state.

Phase space distributions are often illustrated in a two-dimensional  $(q, p)$  diagram by a contour line or a gradient showing the extent of the Wigner function - figure 2.5. This gives the clearest picture of especially Gaussian states, including the squeezed states which will be discussed next. The width of a Gaussian Wigner function is the square-root of the variance, the standard deviation.

Finally, it should be mentioned, that the Wigner function is part of a larger class of distribution functions, called the  $s$ -parameterized quasi-probability functions which can be used for calculating expectation values for operators of different orderings in  $\hat{a}$  and  $\hat{a}^\dagger$ , determined by the parameter  $s$ . For  $s = 0$  we have the Wigner function (symmetrical ordering), while  $s = 1$  and  $s = -1$  give the also quite useful P- (normal ordering) and Q-distributions (anti-normal ordering), respectively [Cahill and Glauber, 1969].

## 2.4 Squeezed states

As shown in (2.28) the uncertainty of a coherent state is  $1/2$  in all quadratures. That is the noise of the vacuum, and it is the noise of a laser beam if all classical noise has been eradicated; the laser is then said to be *shot noise limited*<sup>6</sup>. The coherent state displays the minimum attainable amount of quadrature fluctuations, and all quadratures are “equally good”. However, this is not the end of the story, as should be suspected by now. The uncertainty relation (2.17) only sets a bound for the product of the variances of two conjugate quadratures, not for the individual quadratures, so it should be possible to construct a state for which the variance of one quadrature is

<sup>6</sup>The term comes - as many other terms in quantum optics - from electronics, where it is used for the fluctuations of a current originating from the discreteness of the charge carriers (electrons).

below the SQL at the expense of the conjugate observable whose variance must increase correspondingly. Such states are what we name *squeezed states*. Actually, a state does not need to be a minimum uncertainty state to be called squeezed - it is enough that one of the quadratures is below the SQL.

In the  $(q, p)$  diagram, where the coherent states appear as circles, the squeezed states will be ellipses - see figure 2.5.

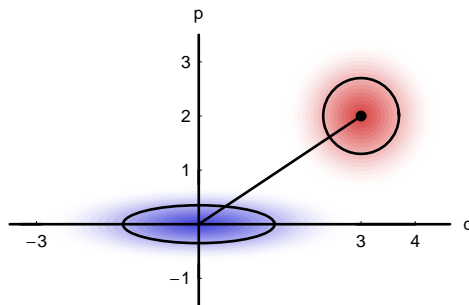


**Figure 2.5:** A squeezed vacuum and a coherent state depicted in a 2D  $(q, p)$  diagram, where the Wigner functions show up as contour plots.

### 2.4.1 Formal description of squeezed states

So far we have only considered single-mode fields. One state of light that is not covered by the single-mode approach is the two-mode squeezed state which is very important for us as it is the basis for our production of entangled beams, described in section 6.1. However the extension to two modes is pretty simple, so we will stick to just a single mode for the rest of this chapter.

We introduce the *squeezing operator*:

$$\hat{S}(\zeta) = \exp\left(\frac{1}{2}\zeta^* \hat{a}^2 - \frac{1}{2}\zeta \hat{a}^{\dagger 2}\right), \quad (2.40)$$

with  $\zeta = -re^{i\varphi}$  where  $r$  is the *squeezing parameter* and  $\varphi/2$  is the orientation of the squeezing.<sup>7</sup> By acting with the squeezing operator on the vacuum state we get the squeezed vacuum. The general squeezed states with non-zero amplitude (called *squeezed coherent states*) are achieved by operating the displacement operator from (2.24) on the squeezed vacuum:

$$|\alpha, \zeta\rangle = \hat{D}(\alpha)\hat{S}(\zeta)|0\rangle. \quad (2.41)$$

In appendix A it is shown that the quadrature variance of a squeezed state is

$$\langle(\Delta\hat{q}_\theta)^2\rangle = \frac{1}{2} [\cosh(2r) + \sinh(2r) \cos(2(\theta - \varphi/2))] \quad (2.42)$$

$$= \frac{1}{2} [e^{-2r} \sin^2(\theta - \varphi/2) + e^{2r} \cos^2(\theta - \varphi/2)], \quad (2.43)$$

<sup>7</sup>The negative  $\zeta$  used here is just an arbitrary choice of phase, made to fit the standard phase choice of the OPO Hamiltonian, (3.12)

which becomes for  $\theta = \varphi/2$  and  $\theta = \varphi/2 + \pi/2$ , respectively:

$$\langle(\Delta\hat{q}_{\varphi/2})^2\rangle = \frac{1}{2}e^{2r}, \quad (2.44)$$

$$\langle(\Delta\hat{q}_{\varphi/2+\pi/2})^2\rangle = \frac{1}{2}e^{-2r}. \quad (2.45)$$

The uncertainty is less than the SQL in the squeezed quadrature  $q_{\varphi/2+\pi/2}$  and greater than the SQL in the anti-squeezed quadrature  $q_{\varphi/2}$ , which was what we were looking for.

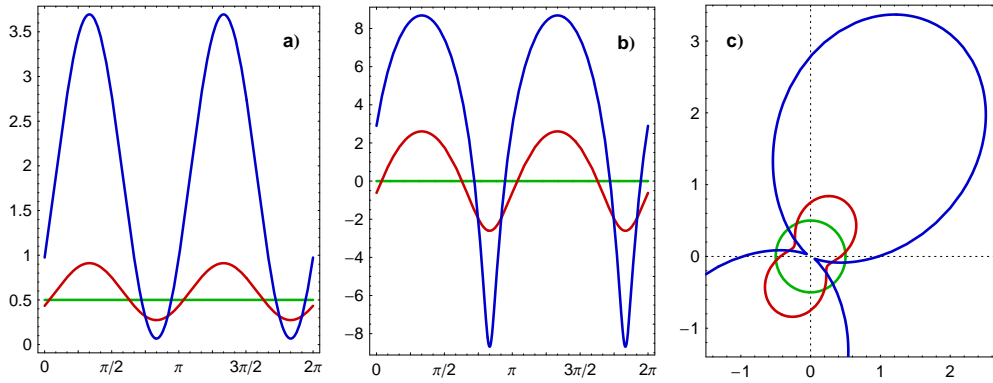


**Figure 2.6:** Three different plots of the quadrature variance (2.43) for three different states with  $r = 1$  (blue),  $r = 0.3$  (red), and  $r = 0$  (green). The squeezing phase is  $\varphi/2 = \pi/3$ . **a)** Regular linear plot of the variance of all quadratures. **b)** The more common decibel-plot, with variances given in dB relative to the SQL. This enhances the clarity of the sub-SQL values. **c)** Polar plot. This is rarely used, but it also gives a nice impression of how narrow the squeezing region is.

Figure 2.6 shows both linear, linear/log and polar plots of the variance versus angle for various squeezing parameters. Note that the low-noise peaks are comparatively narrow - at most angles the noise is actually larger than the SQL. Note also that the polar plot does not look at all like the usual way of depicting the noise in phase space, which is the Wigner function contour of figure 2.5. The Wigner function cannot as such be used to directly read off the noise for any given direction, since the marginal distributions (which will give the noise) are obtained from integrating over all points in the orthogonal direction (eqs. (2.33)-(2.35)). See also figure 5.7.

## 2.4.2 Wigner function

As already implied the Wigner function of a squeezed state is an elliptical Gaussian. For simplicity we set the squeezing phase  $\varphi = 0$ . Then the Wigner function is [Leonhardt, 1997]

$$W(q, p) = \frac{1}{\pi} \exp[-e^{-2r}(q - q_0)^2 - e^{2r}(p - p_0)^2]. \quad (2.46)$$

It is plotted in figure 2.7.

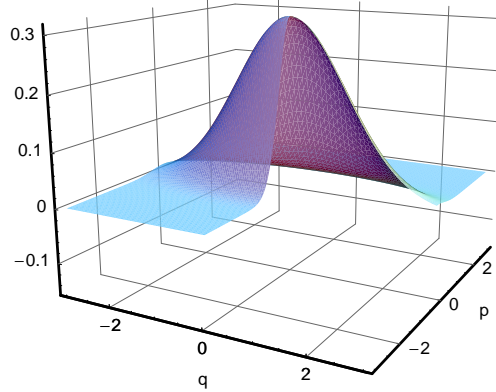


**Figure 2.7:** Wigner function for a squeezed state (2.46) with  $r = 0.5$ .

To see that it has the right quadrature variance, we can calculate the marginal distributions (we set  $q_0, p_0 = 0$  - the displacement does not change the variance):

$$\begin{aligned}
 \Pr(q_\theta) &= \int_{-\infty}^{\infty} W(q \cos \theta - p \sin \theta, q \sin \theta + p \cos \theta) dp \\
 &= \frac{1}{\pi} \int_{-\infty}^{\infty} \exp[-e^{-2r}(q \cos \theta - p \sin \theta)^2 - e^{2r}(q \sin \theta + p \cos \theta)^2] dp \\
 &= \frac{1}{\pi} \int_{-\infty}^{\infty} \exp[-(p^2(e^{-2r} \sin^2 \theta + e^{2r} \cos^2 \theta) - 2qp(e^{-2r} - e^{2r}) \cos \theta \sin \theta \\
 &\quad + q^2(e^{-2r} \cos^2 \theta + e^{2r} \sin^2 \theta))] dp .
 \end{aligned} \tag{2.47}$$

Using the same integration formula as in (2.39) and doing a little arithmetics this becomes

$$\Pr(q_\theta) = \frac{1}{\sqrt{\pi(e^{-2r} \sin^2 \theta + e^{2r} \cos^2 \theta)}} \exp \left[ \frac{-q^2}{e^{-2r} \sin^2 \theta + e^{2r} \cos^2 \theta} \right] , \tag{2.48}$$

which is a one-dimensional Gaussian with the variance given in (2.43).

### 2.4.3 Physical generation

According to the time-dependent Schrödinger equation, the evolution of a state  $|\alpha\rangle$  in time is given by the unitary time-evolution operator  $\hat{U}(t)$  [Sakurai, 1994, sect. 2.1]:

$$|\alpha, t\rangle = \hat{U}(t) |\alpha, 0\rangle , \quad \text{with} \quad \hat{U}(t) = \exp \left( \frac{-i\hat{H}t}{\hbar} \right) \tag{2.49}$$

for initial times  $t_0 = 0$ . If we could find a Hamiltonian that makes the time-evolution operator equal to the squeezing operator, then a physical system having this Hamiltonian should be able to produce squeezed states.

If we let the squeezing parameter include the interaction time,  $r = gt$ , where  $g$  will turn out to be an interaction strength, then the necessary Hamiltonian is read off from (2.40) and (2.49):

$$\hat{H} = \frac{i\hbar g}{2}(e^{i\varphi}\hat{a}^{\dagger 2} - e^{-i\varphi}\hat{a}^2), \quad \text{so that} \quad (2.50)$$

$$\hat{U}(t) = \exp\left[\frac{r}{2}(e^{i\varphi}\hat{a}^{\dagger 2} - e^{-i\varphi}\hat{a}^2)\right] = \exp\left(\frac{1}{2}\zeta^*\hat{a}^2 - \frac{1}{2}\zeta\hat{a}^{\dagger 2}\right) = \hat{S}(\zeta). \quad (2.51)$$

Such an interaction Hamiltonian, quadratic in the field operators, is supplied by the mechanisms of nonlinear optics.

#### 2.4.4 Photon number and statistics

In appendix A it is shown that the mean photon number in a squeezed state  $|\alpha, \zeta\rangle$  is

$$\langle \hat{n} \rangle = |\alpha|^2 + \sinh^2 r, \quad (2.52)$$

that is, the squeezing increases the number of photons in the state. Regarding the individual photon number probabilities, there is an alternating pattern between odd and even numbers [Leonhardt, 1997]:

$$p_n = \begin{cases} 0 & \text{for } n \text{ odd} \\ \binom{n}{n/2} \frac{1}{\cosh r} \left(\frac{1}{2} \tanh r\right)^n & \text{for } n \text{ even} \end{cases}. \quad (2.53)$$

The reason for this pairing of the photons will become clear in the next chapter.

#### 2.4.5 Brief historical overview

Squeezed states of light was first discussed by Stoler [1970] and in detail by Yuen [1976]. Based on a proposal by Yuen and Shapiro [1979], the first experimental demonstration of squeezed light was carried out by Slusher et al. [1985] using four-wave-mixing in a beam of Na-atoms inside an optical cavity. The amount of squeezing was very low, though. A considerably better result was achieved by Wu et al. [1986] using an optical parametric oscillator, which soon became the tool of choice for producing highly squeezed light - it is used in our own experiment and by the current holders of the "squeezing world record", Lam et al. [1999]. Early review articles of squeezed light exist (for instance Henry and Glotzer [1988]) but a much more comprehensive and updated overview of the field is given in the book by Bachor and Ralph [2004]<sup>8</sup>.

<sup>8</sup>Which is very experimentalist-friendly as well!

## Chapter 3

# Squeezing tools

In this chapter we will take a look at our tools at hand for producing squeezed light. In general, for generating squeezing we need nonlinear optical processes, and specifically, in our experiment the nonlinear device employed is the optical parametric oscillator (OPO). In section 3.1 we introduce the field of nonlinear optics with emphasis on the process of second harmonic generation and the phase matching conditions for efficient conversion. In section 3.2 we consider the OPO and give a detailed calculation of the properties of its output field.

### 3.1 Nonlinear interactions

#### 3.1.1 Nonlinear materials

For electromagnetic waves traveling in a dielectric medium, the wave equation (2.1) will include the polarization of the medium:

$$\nabla^2 \mathbf{E} - \frac{1}{c^2} \frac{\partial^2 \mathbf{E}}{\partial t^2} = \frac{1}{\mu_0} \frac{\partial^2 \mathbf{P}}{\partial t^2}. \quad (3.1)$$

The polarization is in general dependent on the field strength, expressed by the Taylor expansion

$$\mathbf{P} = \epsilon_0 (\chi \mathbf{E} + \chi^{(2)} \mathbf{E}^2 + \chi^{(3)} \mathbf{E}^3 + \dots), \quad (3.2)$$

with the various susceptibilities  $\chi^{(n)}$ . For most materials, the higher-order coefficients are so small that for available light intensities only the first linear term matters. For such *linear dielectrics*, inserting  $\mathbf{P} = \epsilon_0 \chi \mathbf{E}$  in (3.1) and using  $\mu_0 \epsilon_0 = c^{-2}$ , we retrieve the wave equation for vacuum (2.1), only with the speed of light in vacuum,  $c$ , exchanged by the reduced speed of light  $c/n$ , where  $n = \sqrt{1 + \chi}$  is the refractive index of the medium. Thus, electric fields behave in linear dielectrics more or less like the free propagation in vacuum.

For certain materials, however, the nonlinear terms start to become significant when applying fields of laser strength. For these *nonlinear materials*, a bunch of new effects come into play. For our purpose we are only interested in the second-order term. This term is responsible for processes involving mixing of fields at three different frequencies. To see this, look at the second-order polarization  $P_{\text{NL}}^{(2)}$  induced

by a superposition of two electric fields at different frequencies with real amplitudes  $E_{\omega_1}$ ,  $E_{\omega_2}$  and the same phase for simplicity:

$$\begin{aligned}
 P_{\text{NL}}^{(2)} &= \epsilon_0 \chi^{(2)} E(t)^2 \\
 &= \epsilon_0 \chi^{(2)} (E_{\omega_1} \cos \omega_1 t + E_{\omega_2} \cos \omega_2 t)^2 \\
 &= \frac{\epsilon_0 \chi^{(2)}}{2} [E_{\omega_1}^2 + E_{\omega_2}^2 + E_{\omega_1}^2 \cos 2\omega_1 t + E_{\omega_2}^2 \cos 2\omega_2 t \\
 &\quad + 2E_{\omega_1} E_{\omega_2} (\cos(\omega_1 - \omega_2)t + \cos(\omega_1 + \omega_2)t)].
 \end{aligned} \tag{3.3}$$

The nonlinear polarization thus have a DC term plus terms at the double frequencies  $2\omega_1$ ,  $2\omega_2$ , the difference frequency  $\omega_1 - \omega_2$ , and the sum frequency  $\omega_1 + \omega_2$ . This means that it is also possible to produce electric fields at these new frequencies through the interaction between the entering fields and the nonlinear material (crystal). These frequency mixing processes are known as *second harmonic generation*, SHG, *difference frequency generation*, DFG, and *sum frequency generation*, SFG, respectively.

In the photon picture, SFG, for instance, can be visualized as two photons at frequencies  $\omega_1$  and  $\omega_2$  combining to produce a single, more energetic photon which, to obey energy conservation, must have frequency  $\omega_3 = \omega_1 + \omega_2$ . The opposite process is also possible - an  $\omega_3$  photon splitting into two less energetic photons. This process, called *down-conversion*, is what we utilize in our OPO to produce squeezed light. A lot more on that in section 3.2. The other nonlinear process important for us is SHG which we use for producing the pump beam for the OPO.

### 3.1.2 Phase matching

For efficient frequency conversion, the interacting fields need not only fulfill the energy conservation criterium but also momentum conservation. Restricting ourselves to the case of SHG and assuming plane wave propagation of the *fundamental* ( $E_\omega$ ) and *harmonic*<sup>1</sup> ( $E_{2\omega}$ ) fields, the wave equation for the harmonic becomes [Saleh and Teich, 1991, sect. 19.4]

$$\frac{dE_{2\omega}}{dy} = \frac{i\omega\chi^{(2)}}{2cn} E_\omega^2 e^{i\Delta ky}, \tag{3.4}$$

with propagation through the crystal in the y-direction and

$$\Delta k = k_{2\omega} - 2k_\omega = \frac{4\pi}{\lambda_\omega} (n_{2\omega} - n_\omega) \tag{3.5}$$

is the *wave vector mismatch*<sup>2</sup> which is usually non-zero for dispersive materials (frequency dependent refractive index). This mismatch has a huge influence on the amount of second harmonic produced through the crystal. We assume a weak coupling between the fields and therefore no depletion of the pump,  $dE_\omega/dy \approx 0$ . Integrating (3.4) over the crystal length  $L$  then gives

$$E_{2\omega}(L) = \frac{\omega\chi^{(2)}}{2cn} E_\omega(0)^2 \frac{e^{i\Delta kL} - 1}{\Delta k}. \tag{3.6}$$

<sup>1</sup>We will loosely use these terms to refer to the two wavelengths used: Fundamental = pump field, main laser = infrared, and harmonic = second harmonic field = blue.

<sup>2</sup>In general  $\Delta \mathbf{k}$  is a vector mismatch, but we only consider collinear propagation of the fields, that is, scalar wave numbers.

We want to calculate the conversion in terms of power or intensity, since the field itself is not directly observable. The intensity is related to the field amplitude through [Griffiths, 1999]

$$I_\omega = \frac{1}{2} \epsilon_0 c n |E_\omega|^2 . \quad (3.7)$$

Using this, and manipulating (3.6) a little, we get the following relationship between the fundamental and harmonic intensities:

$$\frac{I_{2\omega}(L)}{I_\omega(0)^2} = \frac{8\pi^2 d_{\text{eff}}^2 L^2}{\epsilon_0 c n_\omega^2 n_{2\omega} \lambda_\omega^2} \frac{\sin^2 \Delta k L / 2}{(\Delta k L / 2)^2} , \quad (3.8)$$

where  $d_{\text{eff}} = \chi^{(2)}/2$  is the value of the *effective nonlinearity* normally tabulated. It is called an effective value, because  $\chi_{ijk}^{(2)}$  is in general a tensor of second rank, but for a given polarization and direction of propagation through the crystal of the fundamental it is possible to calculate the effective nonlinearity - see for instance Dmitriev et al. [1997].

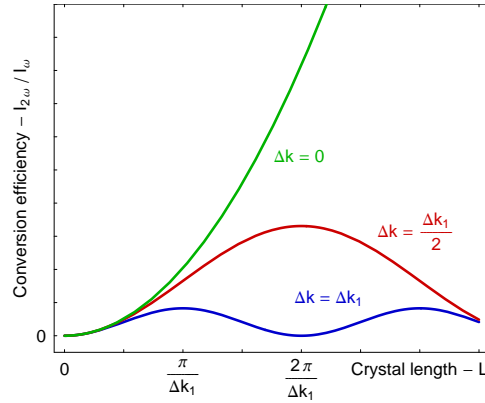


**Figure 3.1:** The effect of wave vector mismatch on the second harmonic conversion efficiency, eq. (3.8), here plotted as a function of crystal length. The lesser the mismatch, the longer it takes before the fundamental and the harmonic gets out of phase causing a decrease in the harmonic field. (after Arie [2004])

This result is plotted in figure 3.1 where we see that non-zero wave vector mismatch causes the converted harmonic intensity to grow and decrease back to zero throughout the crystal. This is because the fundamental and the harmonic acquire a phase shift of  $\pi$  with respect to each other after a propagation distance of  $\pi/\Delta k$ , and so the new harmonic field generated after this distance starts to interfere destructively with the formerly generated field. Only if  $\Delta k = 0$ , the last fraction in (3.8) becomes 1 and the harmonic intensity grows by the square of the interaction length. So, to get an efficient frequency conversion, the wave vectors must fulfill the *phase matching condition*:

$$\Delta k = k_{2\omega} - 2k_\omega = 0 . \quad (3.9)$$

The phase matching is usually accomplished by taking advantage of *birefringent* crystals, that is, crystals with different indices of refraction for different polarizations. In our case the fundamental beam is traveling along the y-axis (crystallographic a-axis),

polarized in the x-direction (horizontal, b-axis). The harmonic beam is then polarized in the z-direction (vertical, c-axis). Conversely, in the process of down-conversion the pump is z-polarized while the two down-converted fields are both x-polarized. This combination of polarizations is known as *Type I phase matching*. Type II phase matching is when the two low-frequency beams are orthogonally polarized.

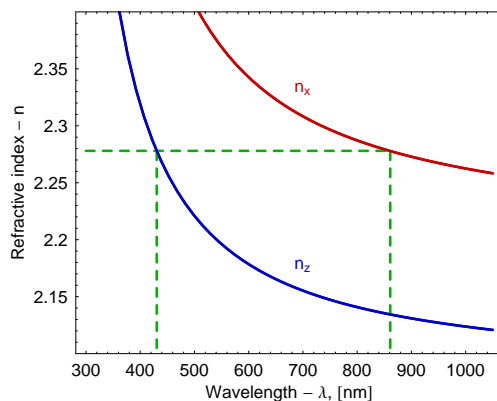


**Figure 3.2:** The refractive indices in the x- and z-directions of the crystal in use,  $\text{KNbO}_3$ , at a temperature of  $30^\circ\text{C}$ . For  $\lambda_\omega = 861\text{nm}$  we have  $n_x(\omega) = n_z(2\omega)$ . All refractive indices are calculated from the Sellmeier equations for  $\text{KNbO}_3$  in Dmitriev et al. [1997].

For a given wavelength the refractive index in the x-direction,  $n_x$ , is quite a bit larger than the corresponding  $n_z$ , but since the refractive index increases for decreasing wavelength, there will be a set of fundamental/harmonic wavelengths for which  $n_x(\omega) = n_z(2\omega)$ , thus fulfilling the phase matching condition. See figure 3.2. Besides the wavelength dependence of the refractive indices, the angle of incidence and the crystal temperature also play a role, so the wavelength for which phase matching occurs can be tuned by either tilting or heating/cooling the crystal. We use the latter method which is depicted in figure 3.3.

A completely different approach to the problem of phase matching is the *quasi phase matching* (QPM) method, thought of first by Armstrong et al. [1962]. This method employs periodically poled crystals, that is, crystals where the polarization of the crystal changes sign with intervals of  $\pi/\Delta k$ , causing a phase shift of  $\pi$  (cf. (3.4)) with the effect that the field generated at  $y = y' + \pi/\Delta k$  will now be *in* phase with the field generated at  $y = y'$  instead of completely out of phase, and so the blue and red conversion efficiency curves in figure 3.1 will continue to rise in a stepwise fashion. This can also be understood from the point of view that the periodic grating of the crystal introduces a lattice structure where the reciprocal lattice vectors can make up for the missing momentum from the wave vector mismatch.

The total conversion efficiency is not as high as for normal birefringent phase matching (the green curve), but on the other hand it is possible to choose the best direction of propagation through the crystal for optimal nonlinearity, while birefringent phase matching is restricted to certain specific directions which may have lower nonlinearity. An even greater advantage of QPM is the possibility of designing the crystal for phase matching of a specific process at a specific wavelength by choosing the grating period to match the given wave vector mismatch. This hugely widens the

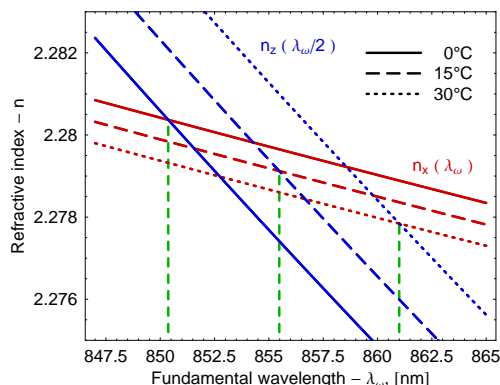


**Figure 3.3:** Temperature and wavelength dependence of  $n_z$  (evaluated at half the specified  $\lambda$ ) and  $n_x$ . We see that for  $0^\circ\text{C}$ ,  $15^\circ\text{C}$ , and  $30^\circ\text{C}$ , phase matching takes place at  $\lambda_\omega = 850.5\text{nm}$ ,  $855.5\text{nm}$ ,  $861.0\text{nm}$ , respectively.

range of efficient nonlinear interaction processes attainable.<sup>3</sup>

For our purpose, though, standard birefringent phase matching with temperature tuning is perfectly suitable, since potassium niobate ( $\text{KNbO}_3$ ) is a highly nonlinear material with phase matching for the wavelengths of interest ( $\sim 852\text{-}860\text{nm}$ ) at experimentally handy temperatures (figure 3.3).

### 3.1.3 Focused beams

So far we have been considering only plane waves, but from (3.8) we see that the conversion efficiency  $I_{2\omega}/I_\omega$  depends linearly on the intensity of the fundamental beam,  $I_\omega$ . This fact calls for us to focus the beam inside the crystal, and even as hard as possible! An extremely hard focusing would however cause heavy heating, which is undesirable, and might even destroy the crystal, and there is another reason as well for not wanting too tight focusing. A focused beam is described by a Gaussian intensity profile (which is a solution of the wave equation in the paraxial approximation, [Milonni and Eberly, 1988]) with beam radius  $w_0$  at the waist and the confocal parameter  $b = k_\omega w_0^2$  - the range around the waist in which the beam radius is less than  $\sqrt{2}w_0$ . A tight focus will lead to a short confocal range, meaning that the beam will diverge faster, and if it diverges too much while inside the crystal, the intensity gets too low at the ends so that the full potential of the crystal is not exploited.

This problem was investigated in detail by Boyd and Kleinman [1968] who found for the *power* conversion (the powers are what we actually measure in practice):

$$\frac{P_{2\omega}}{P_\omega^2} = \frac{16\pi^2 d_{\text{eff}}^2 L}{\epsilon_0 c n_\omega n_{2\omega} \lambda_\omega^3} h(\sigma, \xi), \quad (3.10)$$

<sup>3</sup>During the work on this project I was given the opportunity to investigate a periodically poled KTP crystal, designed for room temperature phase matching at  $843\text{nm}$ , with the goal of determining the applicability of such a crystal to our experiment. However, the measurements, performed together with Martin Sørensen, were unfortunately terminated by the crash of our Verdi laser before any conclusions were reached. I would like to thank Prof. Majid Ebrahim-Zadeh and Gholam Reza Fayaz of ICFO, Barcelona for lending us the crystal.

with the *Boyd-Kleinman h-function*

$$h(\sigma, \xi) = \frac{1}{2\sqrt{\pi}\xi} \int_{-\infty}^{\infty} e^{-4s^2} \left| \int_{-\xi}^{\xi} \frac{e^{i\sigma\tau}}{1+i\tau} d\tau \right|^2 ds. \quad (3.11)$$

$\sigma = \frac{1}{2}b\Delta k$  is a scaling of the wave vector mismatch and  $\xi = L/b$  is the ratio of the crystal length to the confocal parameter. The expression (3.10) disregards absorption in the crystal and assumes the focus of the beam to be centered within the crystal. The h-function is plotted versus both  $\xi$  and  $\sigma$  in figure 3.4, and it is seen to have a unique maximum with a value slightly above 1. This maximum occurs for a focusing parameter of  $\xi_{\text{opt}} = 2.84$  and for a  $\sigma > 0$ , that is, for a non-zero wave vector mismatch. The existence of an optimum focusing parameter gives us a good guideline for designing devices for efficient frequency conversion.

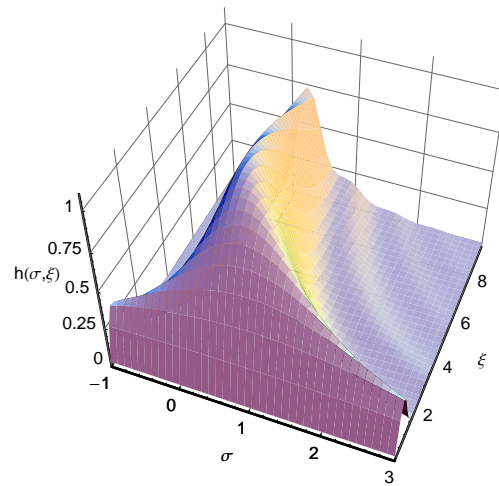


**Figure 3.4:** The Boyd-Kleinman h-function, (3.11), plotted for both parameters: the scaled wave vector mismatch  $\sigma$  and the focusing parameter  $\xi$ . We clearly see a maximum near  $\xi = 2.84$ , but this maximum is actually fairly broad along the  $\xi$ -direction, so the focusing is not extremely critical for the conversion efficiency. As for the mismatch, this is far more critical. We see also a hint of a weak oscillatory behaviour as  $\sigma$  increases (or decreases). This will be investigated further in chapter 4.2.4.

## 3.2 Optical parametric oscillator

The *degenerate optical parametric oscillator* (DOPO) is probably the most widely used tool for generating squeezed light and has been the most efficient so as well ever since the first DOPO squeezed light experiment was carried out by Wu et al. [1986]. Theoretically, already before the term “squeezed state” was coined, Mollow and Glauber [1967] showed that the process of parametric amplification, very closely related to the OPO, will lead to a Wigner function of the field which is narrowed in one direction

and broadened in the other. But Milburn and Walls [1981] were the first to really look into the squeezing properties of the DOPO.

An OPO is in principle a very simple device; it consists of a nonlinear crystal placed inside an optical resonator which can be either standing-wave (2 mirrors) or running-wave (3 or more mirrors). The crystal is then pumped by an intense laser beam, part of which will be down-converted into light at lower frequencies obeying the energy conservation. Because of the cavity buildup of the down-converted field at resonance, we can say that the down-conversion is into discrete modes of the cavity instead of a continuous spectrum. So, a pump photon of frequency  $2\omega_0$  splits into two photons at  $\omega_0 \pm n\omega_{\text{FSR}}$ , where  $n = 0, 1, 2, \dots$  and  $\omega_{\text{FSR}}$  is the *free spectral range*, the spectral distance between two resonances. The cavity is resonant on  $\omega_0$ . There will always be down-conversion into all modes lying within the phase matching bandwidth (figure 3.5), but we can decide to only consider very particular modes and disregard the rest. We therefore choose a specific value of  $n$ ; for  $n = 0$  we talk about a DOPO, otherwise we call it *non-degenerate*, NDOPO. In a NDOPO the down-converted fields are called the signal and idler, respectively; in a DOPO the signal and idler are the same. We can mention here that the bandwidth of phase matching is a lot larger for down-conversion than for SHG - in our case around 20 nm. This is because there is an extra degree of freedom in the down-conversion where only the blue wavelength is fixed while the down-converted wavelengths can vary, whereas in SHG both the red and blue wavelengths are fixed.

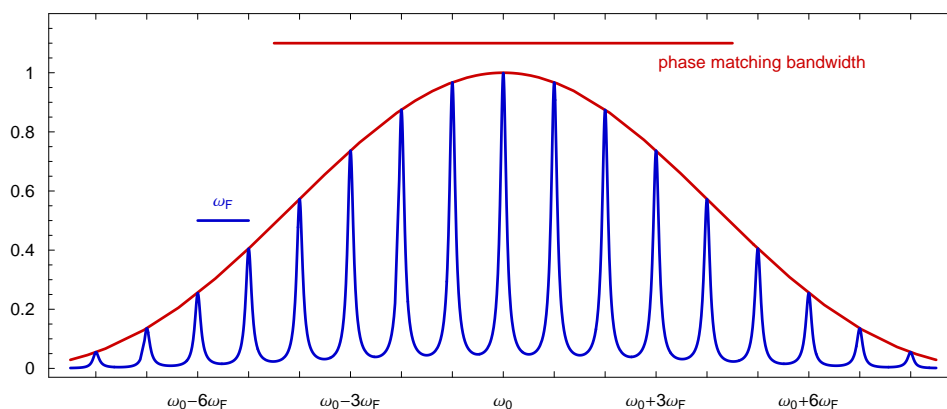


**Figure 3.5:** Spectrum of the OPO when phase matched for optimal down-conversion into  $\omega_0$  - half the pump frequency. The down-converted photons will appear in pairs at frequencies separated by a number of free spectral ranges ( $\omega_{\text{FSR}}$ ) to either side of the central frequency  $\omega_0$ . The phase matching bandwidth is not to scale - in reality it is a lot wider; tens of thousands times the free spectral range.

We can in principle treat the DOPO as single-mode. We will soon see that this is not exactly the case, but for starters it is okay. The two down-converted fields have the same frequency (and same polarization as well), so we can assign them the same operator,  $\hat{a}$ . The interaction Hamiltonian of the down-conversion process is

$$\hat{H}_{\text{int}} = \frac{i\hbar g}{2} (\beta e^{i\varphi} \hat{a}^{\dagger 2} - \beta^* e^{-i\varphi} \hat{a}^2), \quad (3.12)$$

where  $g$  is the interaction strength and  $\varphi$  is a relative phase of the pump field  $\beta =$

$|\beta|e^{-i2\omega_0 t}$  which is so intense that it can be treated classically - it is assumed that it is not depleted by the down-conversion process. This Hamiltonian is the one from (2.50), except that the pump field has now been extracted from the interaction parameter. Thus we already know that the field produced in the crystal should be squeezed, but we do not yet know anything about the effect of the cavity. This will be investigated shortly.

Before that, some words on the name of the device we are using: It is called an ‘oscillator’ because it has a certain threshold value for the pump field, above which the gain surpasses the losses, causing the OPO to produce a coherent output field, much like a laser. This makes it a very suitable device for e.g. spectroscopy, since it is tunable in a very broad range of wavelengths when being run in nondegenerate mode. However, it is very difficult to get a stable output above threshold, and this is not what we are interested in either. We always run the OPO below threshold, in which case the output is an amplification or de-amplification (depending on the relative phase) of the input field which in most cases is vacuum. The ‘parametric’ part of the name comes from the process of parametric amplification which is a general effect also known from electronics and mechanics (e.g. a playground swing<sup>4</sup>), where a fast oscillation can induce amplification or de-amplification of oscillations at half the frequency. Sometimes our machine is called an optical parametric amplifier, OPA, but this name is also used for single pass down-converters without a surrounding cavity<sup>5</sup>, so to emphasize the cavity enhancement, we usually use the name (sub-threshold) OPO for our device. Cavity-enhanced parametric down-conversion is another term in use.

### 3.2.1 Cavity equations

The model of our cavity is as depicted in figure 3.6: A running-wave cavity with one mirror having intensity transmission  $T_1$  and the rest of the mirrors being 100% reflecting for the down-converted wavelength, so that we have the cavity field  $\hat{a}$ , and the incoming and outgoing fields  $\hat{a}_{\text{in}}$  and  $\hat{a}_{\text{out}}$ . The internal intensity losses  $\mathcal{L}$  in the cavity are modeled by a beamsplitter with transmission  $1 - \mathcal{L}$  which also introduces noise (vacuum fluctuations) indicated by the auxiliary field  $\hat{b}_{\text{in}}$ . The losses could also be taken as evenly distributed throughout the length of the cavity, but since the majority of the losses take place in the crystal, the beamsplitter is a better model. The pump field  $\beta$  is not resonant in the cavity.

The cavity round-trip time is  $\tau = l/c$ , with  $l$  the length of the cavity. The free spectral range in ordinary frequency units is  $\nu_{\text{FSR}} = 1/\tau$ . In one round-trip, the field amplitude (square root of the intensity) is attenuated by the factor

$$r = \sqrt{1 - T_1} \sqrt{1 - \mathcal{L}} \approx 1 - \frac{1}{2}T_1 - \frac{1}{2}\mathcal{L}, \quad (3.13)$$

where the approximation holds for  $T_1 \ll 1$ ,  $\mathcal{L} \ll 1$ . The intensity profile of the cavity

<sup>4</sup>As suggested in Buchhave [2004]. A field study was proposed but never carried out, so we gained no experimental verification of this claim.

<sup>5</sup>These devices consisting of just a pumped crystal producing spontaneously parametric down-converted photon pairs are widely used in e.g. quantum cryptography experiments and fundamental tests of quantum mechanics.

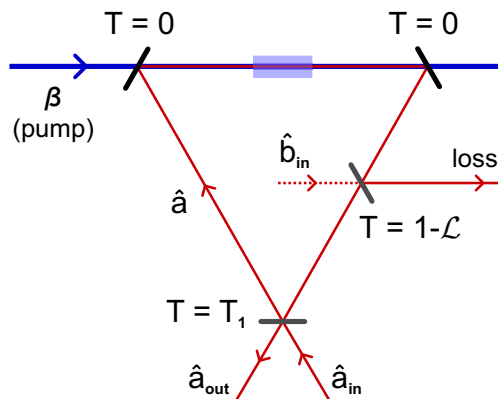


**Figure 3.6:** Our cavity model. Only one mirror is transparent for the down-converted wavelength. The internal losses are modeled by the fictitious beamsplitter, letting vacuum noise into the cavity field.

mode is given by

$$I(\nu) = \frac{I_{\max}}{1 + \left(\frac{2\pi}{\mathcal{F}}\right)^2 \sin^2\left(\frac{\pi\nu}{\nu_{\text{FSR}}}\right)}, \quad (3.14)$$

which has a maximum for every integer multiple of the free spectral range;  $\nu_{\text{resonance}} = m\nu_{\text{FSR}}$ .  $I_{\max}$  is the intensity on resonance and the *finesse* is

$$\mathcal{F} \equiv \frac{\pi\sqrt{r}}{1-r} \approx \frac{2\pi}{T_1 + \mathcal{L}}. \quad (3.15)$$

The full-width-half-maximum (FWHM) of the intensity profile is  $\Delta\nu_{\text{cav}} \approx \nu_{\text{FSR}}/\mathcal{F}$ .

For a slow decay of the cavity field (high finesse), we can associate exponential decay rates individually with the output coupler ( $\kappa_1$ ) and the losses ( $\kappa_L$ ). These are then given by

$$\kappa_1 = \frac{1 - \sqrt{1 - T_1}}{\tau} \approx \frac{T_1}{2\tau}, \quad \kappa_L = \frac{1 - \sqrt{1 - \mathcal{L}}}{\tau} \approx \frac{\mathcal{L}}{2\tau}. \quad (3.16)$$

Thus, the total decay rate  $\kappa_1 + \kappa_L$  corresponds to the half-width-half-maximum spectral width of the cavity in angular frequency units:

$$\kappa_1 + \kappa_L = \frac{T_1 + \mathcal{L}}{2\tau} = \pi\Delta\nu_{\text{cav}} = \frac{\Delta\omega_{\text{cav}}}{2}. \quad (3.17)$$

References for the cavity equations are Saleh and Teich [1991] and Bachor and Ralph [2004].

### 3.2.2 Broadband equations of motion for the cavity mode

Our goal is to find an expression for the squeezing of the output field in terms of the cavity parameters. A detailed derivation will find that this expression has the form of a spectrum of squeezing; there will be a certain bandwidth within which squeezing can be observed. The treatment in this and the following subsection is in great part based on the paper by Collett and Gardiner [1984], which, together with Yurke [1984], was one of the first to thoroughly investigate the output properties of a degenerate OPO. There are several other ways to get to the output spectrum of the OPO, but Collett and Gardiner's approach is rather intuitive.

One way to find the properties of the cavity field is by using the so-called Langevin equations [Risken, 1989], which are essentially the Heisenberg equations of motion for the cavity mode operators with some decay and noise terms added. For the system in question, the Langevin equation for the  $\hat{a}$  operator becomes

$$\frac{d\hat{a}}{dt} = -\frac{i}{\hbar}[\hat{a}, \hat{H}] - (\kappa_1 + \kappa_L)\hat{a} + \sqrt{2\kappa_1}\hat{a}_{\text{in}} + \sqrt{2\kappa_L}\hat{b}_{\text{in}}, \quad (3.18)$$

where  $\hat{H}$  is the full Hamiltonian of the internal cavity mode,  $\hat{H} = \hat{H}_{\text{free}} + \hat{H}_{\text{int}}$  with  $\hat{H}_{\text{free}} = \hbar\omega_0\hat{a}^\dagger\hat{a}$  being the usual Hamiltonian of the free cavity mode (2.12). The first term of the right hand side is the usual Heisenberg equation of motion, the second term is the decay of the cavity mode through outcoupler and loss, and the last part is the incoupling of external modes which is always vacuum for  $\hat{b}_{\text{in}}$  and most often also vacuum for  $\hat{a}_{\text{in}}$  unless we specifically inject an auxiliary field.

In a frame rotating at the optical frequency  $\omega_0$ , the equation of motion for the annihilation operator becomes (see appendix, (B.4))

$$\frac{d\hat{a}}{dt} = g|\beta|e^{i\varphi}\hat{a}^\dagger - (\kappa_1 + \kappa_L)\hat{a} + \sqrt{2\kappa_1}\hat{a}_{\text{in}} + \sqrt{2\kappa_L}\hat{b}_{\text{in}}. \quad (3.19)$$

We now move ahead from our previous single-mode description to a more detailed one, which takes account of the fact that the cavity mode into which the down-converted photons are produced has a finite linewidth.<sup>6</sup> Thus, the down-converted photons are produced pairwise at frequencies  $\omega_0 + \omega$  and  $\omega_0 - \omega$ , where  $\pm\omega$  represents relatively small frequency sidebands within the linewidth  $\kappa_1 + \kappa_L$  of the cavity.

We start by changing to the frequency domain by Fourier transformation of the field operators. Let the frequency components of the operators be denoted by a tilde instead of a hat:

$$\tilde{a}(\omega) = \frac{1}{\sqrt{2\pi}} \int_{-\infty}^{\infty} e^{i\omega t} \hat{a}(t) dt, \quad (3.20)$$

with the commutation relation (B.6)  $[\tilde{a}(\omega), \tilde{a}^\dagger(\omega')] = \delta(\omega - \omega')$ . In the equations of motion the dagger operator will appear with the negative frequency,  $\tilde{a}^\dagger(-\omega)$ .<sup>7</sup>

<sup>6</sup>In a discussion of the partial failure of some of the first calculations on the degenerate OPO [Milburn and Walls, 1981], H.J. Carmichael writes [Carmichael, 1987]: "The resolution comes with the recognition that two traps are laid for any calculation that focuses on the cavity mode alone [...] First, we should strictly speak of a cavity *quasi-mode*, not a cavity mode. If there is to be an output, the cavity must have at least one partially transmitting mirror, and its modes then acquire a linewidth; these are *quasi-monochromatic*. Thus one might well ask for the frequency decomposition of the squeezing. In a single- (quasi)-mode formulation, this is a question that we are tempted to overlook."

<sup>7</sup>Looking at the inverse Fourier transforms,  $\hat{a}(t) = \frac{1}{\sqrt{2\pi}} \int_{-\infty}^{\infty} e^{-i\omega t} \tilde{a}(\omega) d\omega$ , which gives for the daggered version  $\hat{a}^\dagger(t) = \frac{1}{\sqrt{2\pi}} \int_{-\infty}^{\infty} e^{i\omega t} \tilde{a}^\dagger(\omega) d\omega = \frac{1}{\sqrt{2\pi}} \int_{-\infty}^{\infty} e^{-i\omega t} \tilde{a}^\dagger(-\omega) d\omega$  so that the Fourier partner to  $\hat{a}^\dagger$  is  $\tilde{a}^\dagger(-\omega)$ .

The equation of motion in frequency space becomes

$$-i\omega\tilde{a}(\omega) = g|\beta|e^{i\varphi}\tilde{a}^\dagger(-\omega) - (\kappa_1 + \kappa_L)\tilde{a}(\omega) + \sqrt{2\kappa_1}\tilde{a}_{\text{in}}(\omega) + \sqrt{2\kappa_L}\tilde{b}_{\text{in}}(\omega), \quad (3.21)$$

with the solution for  $\tilde{a}(\omega)$  ( $\tilde{a}^\dagger(-\omega)$  is the same, only with negative pump phase  $\varphi$  and creation and annihilation operators interchanged):

$$\tilde{a}(\omega) = \frac{1}{(\kappa_1 + \kappa_L - i\omega)^2 - g^2|\beta|^2} \left[ (\kappa_1 + \kappa_L - i\omega) [\sqrt{2\kappa_1}\tilde{a}_{\text{in}}(\omega) + \sqrt{2\kappa_L}\tilde{b}_{\text{in}}(\omega)] + g|\beta|e^{i\varphi} [\sqrt{2\kappa_1}\tilde{a}_{\text{in}}^\dagger(-\omega) + \sqrt{2\kappa_L}\tilde{b}_{\text{in}}^\dagger(-\omega)] \right]. \quad (3.22)$$

### 3.2.3 The output field

The net leakage from the cavity through the output coupler must be equal to the sum of the fields outside the cavity entering and exiting through the coupler, so the boundary condition for the output coupler is

$$\sqrt{2\kappa_1}\tilde{a}(\omega) = \tilde{a}_{\text{in}}(\omega) + \tilde{a}_{\text{out}}(\omega). \quad (3.23)$$

Inserting (3.22), we get an expression for the output field (B.9):

$$\tilde{a}_{\text{out}}(\omega) = \frac{1}{(1 - i\Omega)^2 - \epsilon^2} \times \left\{ [\eta_{\text{esc}}^2 - (1 - \eta_{\text{esc}} - i\Omega)^2 + \epsilon^2] \tilde{a}_{\text{in}}(\omega) + 2\eta_{\text{esc}} \epsilon e^{i\varphi} \tilde{a}_{\text{in}}^\dagger(-\omega) + 2\sqrt{\eta_{\text{esc}}(1 - \eta_{\text{esc}})} (1 - i\Omega) \tilde{b}_{\text{in}}(\omega) + 2\sqrt{\eta_{\text{esc}}(1 - \eta_{\text{esc}})} \epsilon e^{i\varphi} \tilde{b}_{\text{in}}^\dagger(-\omega) \right\}, \quad (3.24)$$

with the new variables

$$\Omega = \frac{\omega}{\kappa_1 + \kappa_L}, \quad (3.25)$$

$$\eta_{\text{esc}} = \frac{\kappa_1}{\kappa_1 + \kappa_L}, \quad (3.26)$$

$$\epsilon = \frac{g|\beta|}{\kappa_1 + \kappa_L}. \quad (3.27)$$

While  $\Omega$  is just a scaling of the detection frequency,  $\epsilon$  and  $\eta_{\text{esc}}$  are more fundamental parameters.  $\eta_{\text{esc}} \approx T_1/(T_1 + \mathcal{L})$  is the *escape efficiency*, that is, the probability that a photon escaped from the cavity goes into the output field and not into losses.  $\epsilon$  is a scaled *pump parameter*: Taking the expectation values of (3.19) gives

$$\frac{d\langle\hat{a}\rangle}{dt} = g|\beta|e^{i\varphi}\langle\hat{a}^\dagger\rangle - (\kappa_1 + \kappa_L)\langle\hat{a}\rangle + \sqrt{2\kappa_1}\langle\hat{a}_{\text{in}}\rangle + \sqrt{2\kappa_L}\langle\hat{b}_{\text{in}}\rangle. \quad (3.28)$$

With no fields injected but the pump ( $\langle\hat{a}_{\text{in}}\rangle = \langle\hat{b}_{\text{in}}\rangle = 0$ ), the oscillation threshold is reached when the cavity field is at steady state, that is, when  $d\langle\hat{a}\rangle/dt = 0$ . This requires a pump field  $|\beta_{\text{thr}}|$  fulfilling

$$(\kappa_1 + \kappa_L)\langle\hat{a}\rangle = g|\beta_{\text{thr}}|e^{i\varphi}\langle\hat{a}^\dagger\rangle, \quad (\kappa_1 + \kappa_L)\langle\hat{a}^\dagger\rangle = g|\beta_{\text{thr}}|e^{-i\varphi}\langle\hat{a}\rangle, \quad (3.29)$$

that is,  $g|\beta_{\text{thr}}| = \kappa_1 + \kappa_L$ , so  $\epsilon = 1$  is the threshold condition for oscillation. For smaller pump fields,  $\epsilon = |\beta|/|\beta_{\text{thr}}|$ .

What would be interesting now is to find the variance of the quadrature operators, since we know that they should show squeezed behaviour. However, since the noise reduction (or amplification) comes about because of correlations between the sidebands at  $\omega$  and  $-\omega$ , we need a measure for the correlation between the fields at different frequencies. This is the covariance, defined for arbitrary operators as

$$\langle \hat{A}, \hat{B} \rangle \equiv \langle \Delta \hat{A} \Delta \hat{B} \rangle = \langle \hat{A} \hat{B} \rangle - \langle \hat{A} \rangle \langle \hat{B} \rangle. \quad (3.30)$$

For a single operator the covariance becomes the usual variance.<sup>8</sup>

Let us take the input fields to be coherent (which they always are in practice). Then because of the coherent state being an eigenstate of the annihilation operator, (2.22), we get that three of the four possible covariances of different frequency components of the input operators become zero:

$$\langle \tilde{a}_{\text{in}}(\omega), \tilde{a}_{\text{in}}(\omega') \rangle = \langle \tilde{a}_{\text{in}}(\omega) \tilde{a}_{\text{in}}(\omega') \rangle - \langle \tilde{a}_{\text{in}}(\omega) \rangle \langle \tilde{a}_{\text{in}}(\omega') \rangle = 0, \quad (3.31)$$

and similarly

$$\langle \tilde{a}_{\text{in}}^\dagger(\omega), \tilde{a}_{\text{in}}^\dagger(\omega') \rangle = 0, \quad \langle \tilde{a}_{\text{in}}^\dagger(\omega), \tilde{a}_{\text{in}}(\omega') \rangle = 0. \quad (3.32)$$

Only the anti-normally ordered covariance becomes non-zero:

$$\begin{aligned} \langle \tilde{a}_{\text{in}}(\omega), \tilde{a}_{\text{in}}^\dagger(\omega') \rangle &= \langle \tilde{a}_{\text{in}}(\omega) \tilde{a}_{\text{in}}^\dagger(\omega') \rangle - \langle \tilde{a}_{\text{in}}(\omega) \rangle \langle \tilde{a}_{\text{in}}^\dagger(\omega') \rangle \\ &= \delta(\omega - \omega') + \langle \tilde{a}_{\text{in}}^\dagger(\omega') \tilde{a}_{\text{in}}(\omega) \rangle - \langle \tilde{a}_{\text{in}}(\omega) \rangle \langle \tilde{a}_{\text{in}}^\dagger(\omega') \rangle \\ &= \delta(\omega - \omega'). \end{aligned} \quad (3.33)$$

When we then turn to the correlations in the output field, most of the terms vanish when inserting (3.31)-(3.33):

$$\begin{aligned} \langle \tilde{a}_{\text{out}}^\dagger(\omega), \tilde{a}_{\text{out}}(\omega') \rangle &= \frac{1}{[(1+i\Omega)^2 - \epsilon^2][(1-i\Omega')^2 - \epsilon^2]} \left\{ (2\eta_{\text{esc}} \epsilon)^2 \langle \tilde{a}_{\text{in}}(-\omega), \tilde{a}_{\text{in}}^\dagger(-\omega') \rangle \right. \\ &\quad \left. + (2\sqrt{\eta_{\text{esc}}(1-\eta_{\text{esc}})} \epsilon)^2 \langle \tilde{b}_{\text{in}}(-\omega), \tilde{b}_{\text{in}}^\dagger(-\omega') \rangle \right\} \\ &= \frac{4\eta_{\text{esc}} \epsilon^2 \delta(\omega - \omega')}{[(1+i\Omega)^2 - \epsilon^2][(1-i\Omega')^2 - \epsilon^2]}, \end{aligned} \quad (3.34)$$

$$\begin{aligned} \langle \tilde{a}_{\text{out}}(\omega), \tilde{a}_{\text{out}}(\omega') \rangle &= \frac{1}{[(1-i\Omega)^2 - \epsilon^2][(1-i\Omega')^2 - \epsilon^2]} \times \\ &\quad \left\{ 2\eta_{\text{esc}} \epsilon e^{i\varphi} [\eta_{\text{esc}}^2 - (1-\eta_{\text{esc}} - i\Omega')^2 + \epsilon^2] \langle \tilde{a}_{\text{in}}(\omega), \tilde{a}_{\text{in}}^\dagger(-\omega') \rangle \right. \\ &\quad \left. + 4\eta_{\text{esc}}(1-\eta_{\text{esc}}) \epsilon e^{i\varphi} (1-i\Omega') \langle \tilde{b}_{\text{in}}(\omega), \tilde{b}_{\text{in}}^\dagger(-\omega') \rangle \right\} \\ &= \frac{2\eta_{\text{esc}} \epsilon e^{i\varphi} (1 + \Omega'^2 + \epsilon^2) \delta(\omega + \omega')}{[(1-i\Omega)^2 - \epsilon^2][(1-i\Omega')^2 - \epsilon^2]}. \end{aligned} \quad (3.35)$$

<sup>8</sup>For operators with zero expectation value,  $\langle \hat{A}, \hat{B} \rangle = \langle \hat{A} \hat{B} \rangle$ . This could for instance be creation and annihilation operators evaluated for a vacuum state.

The *spectral densities*, which we will denote by  $\langle \cdot, \cdot \rangle_\omega$ <sup>9</sup>, are defined as [Mandel and Wolf, 1995, sect. 2.4]

$$\begin{aligned}\langle \tilde{a}^\dagger, \tilde{a} \rangle_\omega \delta(\omega - \omega') &\equiv \langle \tilde{a}^\dagger(\omega), \tilde{a}(\omega') \rangle \\ \langle \tilde{a}, \tilde{a} \rangle_\omega \delta(\omega + \omega') &\equiv \langle \tilde{a}(\omega), \tilde{a}(\omega') \rangle.\end{aligned}\quad (3.36)$$

Taking the spectral densities corresponding to (3.34) and (3.35) and doing a little algebra yields

$$\langle \tilde{a}_{\text{out}}^\dagger, \tilde{a}_{\text{out}} \rangle_\omega = \eta_{\text{esc}} \epsilon \left[ \frac{1}{(1 - \epsilon)^2 + \Omega^2} - \frac{1}{(1 + \epsilon)^2 + \Omega^2} \right], \quad (3.37)$$

$$\langle \tilde{a}_{\text{out}}, \tilde{a}_{\text{out}} \rangle_\omega = \eta_{\text{esc}} \epsilon e^{i\varphi} \left[ \frac{1}{(1 - \epsilon)^2 + \Omega^2} + \frac{1}{(1 + \epsilon)^2 + \Omega^2} \right]. \quad (3.38)$$

### 3.2.4 Quadrature fluctuations

When we measure squeezed light we always use homodyning which gives an electric current proportional to the measured quadrature variable  $\hat{q}_\theta$  at a specific relative angle  $\theta$  between signal and local oscillator. This will be shown loosely in section 4.4.1. The current is fed into a spectrum analyzer that measures the power spectrum (spectral density) of the current, and therefore effectively of the quadrature. In Ou et al. [1987] it is shown rigorously that this power spectrum is given by

$$\chi_\theta(\omega) = K [1 + \eta_{\text{de}} \langle : \tilde{q}_\theta, \tilde{q}_\theta : \rangle_\omega], \quad (3.39)$$

where  $::$  denotes normal ordering of the operators,  $\eta_{\text{de}}$  is the detection efficiency (the probability of one photon to produce one photoelectron), and  $K$  is a factor including the local oscillator intensity and the detection bandwidth. In the aforementioned paper the scaling of the quadrature operators is such as to yield a SQL of 1, whereas in our scaling the SQL is  $1/2$ .<sup>10</sup> The first term in (3.39) corresponds to this SQL, so we should instead use

$$\chi_\theta(\omega) = \frac{1}{2} + \eta_{\text{de}} \langle : \tilde{q}_\theta, \tilde{q}_\theta : \rangle_\omega, \quad (3.40)$$

where we omit  $K$  to scale to the SQL. The normal ordered quadrature spectrum is, by (3.37) and (3.38),

$$\begin{aligned}\langle : \tilde{q}_\theta, \tilde{q}_\theta : \rangle_\omega &= \langle : \frac{1}{\sqrt{2}}(\tilde{a}_{\text{out}} e^{-i\theta} + \tilde{a}_{\text{out}}^\dagger e^{i\theta}), \frac{1}{\sqrt{2}}(\tilde{a}_{\text{out}} e^{-i\theta} + \tilde{a}_{\text{out}}^\dagger e^{i\theta}) : \rangle_\omega \\ &= \langle \tilde{a}_{\text{out}}^\dagger, \tilde{a}_{\text{out}} \rangle_\omega + \frac{1}{2} e^{-2i\theta} \langle \tilde{a}_{\text{out}}, \tilde{a}_{\text{out}} \rangle_\omega + \frac{1}{2} e^{2i\theta} \langle \tilde{a}_{\text{out}}^\dagger, \tilde{a}_{\text{out}}^\dagger \rangle_\omega \\ &= \eta_{\text{esc}} \epsilon \left\{ \left[ \frac{1}{(1 - \epsilon)^2 + \Omega^2} - \frac{1}{(1 + \epsilon)^2 + \Omega^2} \right] \right. \\ &\quad \left. + \left( \frac{e^{-i(2\theta - \varphi)} + e^{i(2\theta - \varphi)}}{2} \right) \left[ \frac{1}{(1 - \epsilon)^2 + \Omega^2} + \frac{1}{(1 + \epsilon)^2 + \Omega^2} \right] \right\}.\end{aligned}\quad (3.41)$$

<sup>9</sup>The usual notation is  $S(\omega)$ , but we need the spectral densities for several different combinations of operators, so this homemade notation is more convenient.

<sup>10</sup>With regards to squeezing, it is actually more handy to work with the scaling where SQL = 1. One reason for choosing this other scaling (corresponding to  $\hbar = 1$ ) was that it is used in the quantum memory experiment.

We obtain the final result for the measured spectrum:

$$\chi_{\theta}(\omega) = \frac{1}{2} + \eta\epsilon \left[ \frac{1 + \cos[2(\theta - \varphi/2)]}{(1 - \epsilon)^2 + \Omega^2} - \frac{1 - \cos[2(\theta - \varphi/2)]}{(1 + \epsilon)^2 + \Omega^2} \right], \quad (3.42)$$

with the combined efficiency  $\eta = \eta_{\text{de}}\eta_{\text{esc}}$ .

The two most interesting quadrature angles are  $\theta = \varphi/2$  and  $\theta = \varphi/2 + \pi/2$ , for which the spectra become

$$\chi^+ = \chi_{\frac{\varphi}{2}} = \frac{1}{2} + \frac{2\eta\epsilon}{(1 - \epsilon)^2 + \Omega^2} \quad (\text{anti-squeezing}), \quad (3.43)$$

$$\chi^- = \chi_{\frac{\varphi}{2} + \frac{\pi}{2}} = \frac{1}{2} - \frac{2\eta\epsilon}{(1 + \epsilon)^2 + \Omega^2} \quad (\text{squeezing}). \quad (3.44)$$

These two spectra are plotted in figure 3.7 for perfect efficiency,  $\eta = 1$ , and fairly weak pump,  $\epsilon = 0.3$ .

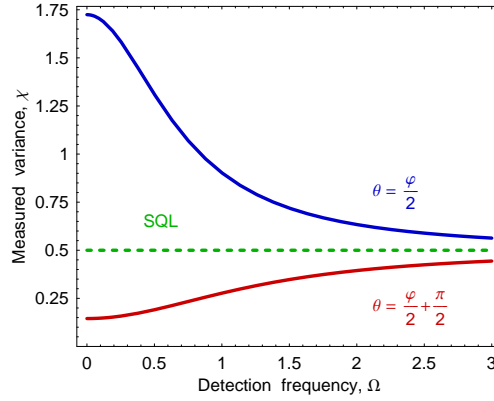


**Figure 3.7:** Spectrum of the fluctuations of the output field at angles giving maximum squeezing and anti-squeezing. The parameters are  $\epsilon = 0.3$ ,  $\eta = 1$ .

In figure 3.8 we see how the amount of squeezing (for  $\Omega = 0.25$ ) depends on the two crucial experimental parameters  $\eta$  and  $\epsilon$ . The scale is the commonly used logarithmic dB-scale with the SQL at 0 dB and -3 dB corresponding to a squeezing by a factor of two ( $\chi = 1/4$ ). For the range of parameter space accessible with our setup, we see that  $\eta$  is slightly more critical than  $\epsilon$ .

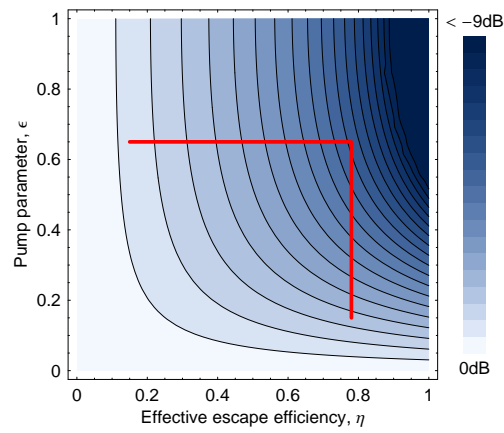


**Figure 3.8:** The amount of squeezing for different  $\eta$  and  $\epsilon$  on logarithmic scale with .5dB steps. Our best experimentally achieved values are marked by the red lines.



## Chapter 4

# Squeezing experiment

The squeezing experiment was designed and built in Århus by Jens Lykke Sørensen and Christian Schori and the experimental setup and the considerations that went into the design of it is already well described in the thesis of Schori [2002] and in a research progress report [Arcizet, 2001] as well. A very similar but earlier setup is reported in Sørensen et al. [1997], Polzik et al. [1998], and Sørensen [1998], and the general design ideas trace directly back to the Caltech group in the beginning of the 1990's [Polzik et al., 1992]. In this chapter it will be endeavoured to put the emphasis on aspects of the experiment that will avoid too much redundancy with especially the thesis of Christian Schori. However, to ensure a consistent treatment there will of course be some overlap.

We will start with a quick and dirty run down of the full experimental setup, later get more in detail with important parts, and end with some squeezing results.

### 4.1 Overview

A sketch of the experimental setup is shown in figure 4.1. Many of the mirrors and all the lenses have been left out - every beam that needs to be mode matched to a cavity requires at least two adjustable mirrors and one lens, so this makes for a lot of optical components. Furthermore, most of the beamsplitters in the sketch plus a few not shown actually consist of a polarizing beamsplitter cube (PBS) and a half-wave plate to allow for an adjustable splitting ratio. Aside from that, all of the important optics in the squeezing experiment is present in the figure.

In the following we will go through each part of the setup, with numbered references to figure 4.1:

**1. Pump laser** As the pump laser for our Ti:Sapph (2) we use a commercial Verdi V-10 from Coherent. This consists of a pack of Nd:YVO<sub>4</sub> diodes frequency doubled to produce a green output at 532 nm of 10 W. We usually only run it at 9-9.5 W.

**2. Ti:Sapph** The Titanium Sapphire laser is the source of all light consumed in the experiment. It was constructed by Lasse Leick and is described in every detail in his thesis [Leick, 1998]. It consists of a Titanium Sapphire crystal placed inside a bow-tie cavity and pumped by the Verdi output. It fluoresces in a very broad range of

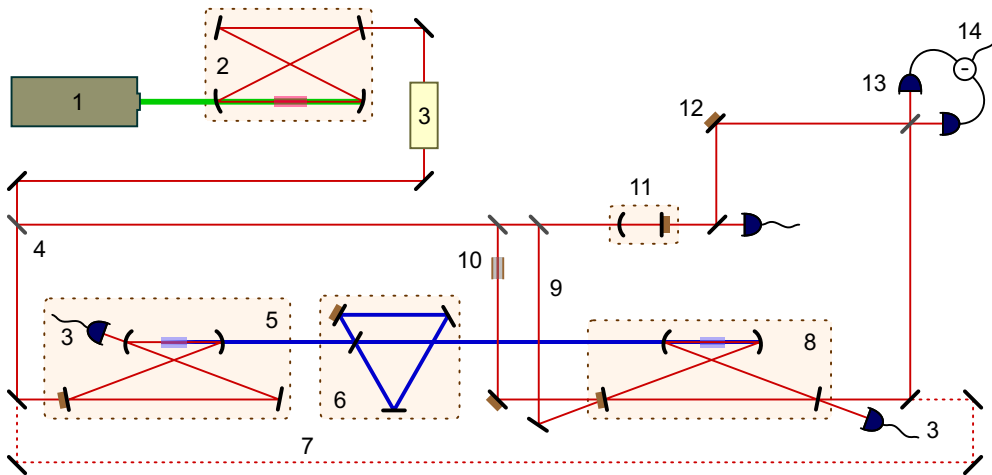


**Figure 4.1:** Our experimental setup for producing and measuring squeezed light. See the text for explanation of the various parts.

wavelengths but the present coating of the cavity mirrors narrows the usable range down to  $\sim 830\text{-}870$  nm. A birefringent filter and an etalon further restricts the lasing to just a single longitudinal mode as required, but these can be turned to tune the lasing wavelength. We have been operating at  $857\text{-}860$  nm which corresponds to phase matching of  $\text{KNbO}_3$  at close to room temperature, cf. figure 3.3. An optical isolator is placed right at the output to avoid the worst back-reflection into the laser. Usual output powers after this isolator are  $700\text{-}800$  mW. The linewidth of the laser is  $< 300$  kHz according to Arcizet [2001].

**3. Cavity stabilization system** For locking the SHG and the OPO cavities to resonance we employ the Pound-Drever-Hall technique [Drever et al., 1983, Bjorklund et al., 1983] where reflected or transmitted light from the cavity is detected, and RF sidebands of the optical carrier frequency gets demodulated to produce a DC signal which is exactly zero at resonance but positive on one side of the resonance and negative on the other side. This signal is then fed into an electronic controller which provides a suitable correction voltage to a piezo actuator glued to a mirror in the cavity. This way the optical length of the cavity is stabilized to stay on resonance. To introduce the necessary sidebands of the light we use an electro optic modulator (EOM) driven at  $20$  MHz.

**4. Auxiliary beams** By far the largest part of the infrared light is directed into the doubling cavity (5), but we also need some beams for the homodyne local oscillator and for locking the OPO, so a small part of the Ti:Sapph output is split off for these purposes. By using the same laser source for everything on the table we ensure phase coherence and the exact same wavelengths.

**5. SHG** The frequency doubling or SHG cavity is a bow-tie design with two flat and two curved mirrors. Between the curved mirrors the  $10\times 3\times 3$  mm Potassium Niobate ( $\text{KNbO}_3$ ) crystal is situated in a temperature controlled oven (or refrigerator!) and

further mounted on a translation and rotation stage to allow for optimal passage of the light - the crystal is not very homogeneous, so it is necessary to search for a line of propagation with low loss and high nonlinearity. The temperature is regulated by a peltier element and a feedback controller and is very stable (estimated to be within a few mK) as soon as it has reached its set point. This is crucial for efficient SHG because the cavity is bistable, so that a small temperature fluctuation at the peak of the phase matching curve can cause a dramatic loss in conversion efficiency. For IR pump powers of 500-560 mW the maximum observed blue output is 270 mW - usual values are 200-240 mW.

**6. “Blue” cavity** Normally, mode matching of a beam to a cavity takes place by looking at the part of the beam transmitted through the cavity while this is being scanned. When the mode matching is 100%, the transmission pattern has only one big peak corresponding to the  $TEM_{0,0}$  mode of the cavity. When it is less than 100%, several other peaks corresponding to higher order transverse Gaussian modes,  $TEM_{n,m}$ , will show up somewhere else in the pattern because the resonance frequencies depend on  $n$  and  $m$ . This way of mode matching requires the cavity to be build for resonating the incoming beam. In the case of the OPO cavity (8), this is build for resonating at 860 nm but not at 430 nm, where the mirrors are transparent. Thus we cannot mode match the blue light to the OPO in the usual fashion. Instead we have a small blue-resonant reference cavity in between the SHG and OPO, to which we mode match the blue light from the SHG.

**7. OPO cavity working as frequency doubler** To complete the SHG $\leftrightarrow$ OPO mode matching, the OPO needs to be mode matched to the blue cavity as well. This is done by changing the beam path to inject the IR directly into the OPO in the backwards direction. Then the OPO acts as a frequency doubler<sup>1</sup> and produces blue light in the direction of the blue cavity. When both SHG and OPO are mode matched properly to the blue cavity, they should as well be mode matched to each other.

**8. OPO** The parametric oscillator is almost an exact copy of the SHG cavity. The blue light enters through one of the curved mirrors and pumps the  $KNbO_3$  in a single pass. All mirrors except the output coupler (one of the flat mirrors with  $T = 12.7\%$ ) are high reflectors for the down-converted wavelength.

**9. Locking beam** Since there is no strong field at the resonance wavelength in the OPO, we need to inject a beam to get a signal to lock on. This is done through one of the high reflectors in the opposite propagation direction as the down-converted field so that the two fields do not get mixed up. The transmission signal of the locking beam is detected outside the output coupler.

**10. Coherent input beam** The OPO can also work as a classical parametric amplifier, where a coherent input in the signal mode gets amplified or deamplified depending on its phase relative to the pump. By injecting a beam into the OPO and observing the amplification or gain of the transmitted signal, we get information about the performance of the OPO, directly relatable to its squeezing capabilities. When doing the squeezing experiment, injecting this beam causes the output of the OPO to be a

<sup>1</sup>We normally refer to the specific cavity as simply the ‘OPO’, even if it is not operated as an OPO.

squeezed coherent state instead of squeezed vacuum. This would correspond to a new input field operator  $\hat{c}_{\text{in}}$  (with a decay rate  $\kappa_c$  corresponding to the transmission of the high reflecting mirror) in the equations of motion. It will not change the variance of the state, but the displacement from zero field amplitude will be visible in the reconstructed Wigner function. Since the squeezing is measured at 1.1 MHz and the linewidth of the Ti:Sapph laser is much smaller, we need to add a sideband at 1.1 MHz to the injected beam to get some power at this frequency. This is done by a tiny EOM consisting of only a KNbO<sub>3</sub> crystal with an applied voltage at 1.1 MHz.

**11. LO cleaning cavity** The local oscillator for the homodyning setup needs to have a clean Gaussian shape in order to achieve a good interferometric visibility. This is achieved by sending it through a Fabry Perot resonator which efficiently eliminates all higher order transverse modes. The cavity is locked on the side of the transmission peak which also allows us to tune the power of the LO simply by choosing how high on the side we want to lock.

**12. LO phase scan** The phase of the local oscillator relative to the OPO output can be linearly (or almost linearly) scanned by changing the beam path length with a piezo-mounted mirror.

**13. Homodyne measurement** The homodyne setup employed to detect the quadrature fluctuations of the OPO output consists of a 50/50 beamsplitter, on which the signal and LO should be close to perfectly mode matched, plus two Silicon PIN photodiode detectors, one for each beamsplitter output port. The circuitry of the detectors is tuned for a maximum gain at 1.1 MHz, giving a better signal-to-noise ratio at this frequency. The two detectors are then balanced in gain and phase and the two photocurrents are subtracted to yield the homodyne current which is proportional to the quadrature variance of the signal.

**14. Analyzer** Finally the homodyne signal is fed into a spectrum analyzer which directly shows the noise power of the signal at a given frequency. Alternatively we can demodulate the signal at 1.1 MHz, amplify it, and observe it on a digital storage oscilloscope. This gives a very clear picture of how the noise is increased or decreased at various quadratures.

## 4.2 Frequency doubling

### 4.2.1 Cavity design

The SHG cavity was designed with one important goal in mind: the best conversion efficiency of IR to blue light possible. The result was a bow-tie cavity of length  $l = 70$  cm and two curved mirrors with radii of curvature of 5 cm which focuses the beam tightly in between them. The distance between the curved mirrors can be adjusted and is quite critical for the stability of the cavity and for the focus waist size. Using the ABCD-technique [Milonni and Eberly, 1988] it can be calculated that the cavity is stable with a mirror separation of  $\sim 5.6 - 5.9$  cm, and that the waist in this region is

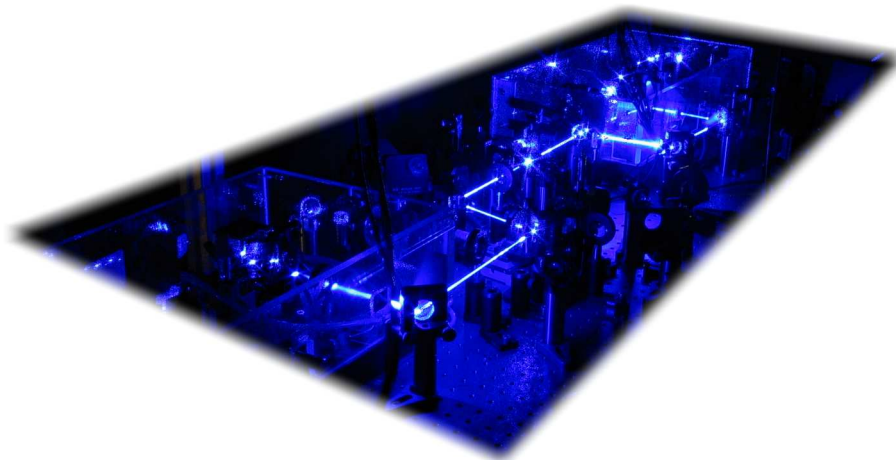


**Figure 4.2:** This photograph shows the second harmonic generator in the top part and the OPO in the left part. Both cavities are enclosed in plexiglass boxes. We see how the generated blue light propagates from the SHG to the OPO through the blue reference cavity (hardly visible - placed midway between the two other cavities).

$w_0 \approx 16 \mu\text{m}$ . According to subsection 3.1.3 the optimal waist would be

$$w_0^{\text{opt}} = \sqrt{\frac{b_{\text{opt}}}{k_\omega}} = \sqrt{\frac{\xi_{\text{opt}}/L}{2\pi n_\omega/\lambda_\omega}} = 14.5 \mu\text{m} . \quad (4.1)$$

The slightly larger than optimal waist does not cause a serious degradation of conversion efficiency; on the contrary it probably diminishes some of the severe problems caused by heating of the crystal by absorption.

The curved mirrors have a transmission at 430 nm of 91%. At 860 nm all mirrors except the input coupler are high reflectors with less than 200 ppm transmission (manufacturer's data). The input coupler transmission is  $T_1 = 6.5\%$ .

### 4.2.2 Crystal nonlinearity

We will need a parameter to quantify the nonlinearity of the  $\text{KNbO}_3$  crystal. The effective nonlinearity of this material with the chosen crystal cut and propagation direction is  $d_{\text{eff}} = -11.9 \text{ pm/V}$  [Dmitriev et al., 1997] but this number is not directly applicable to the experimental situation. Instead we use the parameter (3.10) which is the ratio of the single pass blue power production to the square of the incident IR power. All the factors in this expression are fixed except for the Boyd-Kleinman h-function. We define our single pass nonlinearity  $E_{\text{NL}}$  as the  $P_{2\omega}/P_\omega^2$  value obtained at optimal phase matching. The theoretical value (3.10) of this parameter is 2.6%/W with a maximum Boyd-Kleinman number of 1.05. Different crystals have different  $E_{\text{NL}}$ , and even a single crystal can be very inhomogeneous. The one we use for SHG typically has a value of  $E_{\text{NL}} = 1.4 - 1.5\%/W$ . For other 10 mm Potassium Niobates, up to 2%/W has been reported [Mabuchi et al., 1994].

The ways to measure the nonlinearity and the different losses as well are discussed in Schori [2002].  $E_{\text{NL}}$  can be measured either in single-pass or with cavity build-

up. The losses can be inferred from either a transmission or a reflection signal when scanning the cavity through resonance.

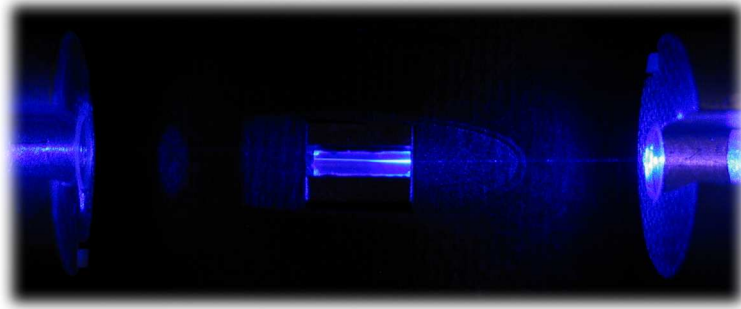


**Figure 4.3:** This photograph shows the buildup of the second harmonic blue light in the crystal, being pumped from the left. The 10 mm long crystal is placed in a temperature controlled oven and positioned between the two curved mirrors which are at the edges of the picture.

### 4.2.3 Losses

One of the most important parameters for the SHG and especially for the OPO is the intracavity loss  $\mathcal{L}$  which seriously deteriorates the performance of those devices in terms of blue light production and the amount of squeezing attainable. There are two major sources of loss of the fundamental field:

**Passive losses** The passive cavity losses,  $\mathcal{L}_c$ , comes from absorption and scattering in mirrors and crystal plus reflection on the crystal surfaces and the non-zero transmission of the high reflecting mirrors. These are all impossible to get rid of, but it has been sought to minimize the last two by high quality coatings (cleaning the components once in a while can do wonders as well!) and the bulk losses in the crystal can be minimized by translating it. The crystal is not surprisingly the main contributor of passive losses; with an empty cavity we measure  $\mathcal{L}_c = 0.1\%$ , while insertion of the crystal gives  $\mathcal{L}_c \sim 0.8 - 1.0\%$ .

**BLIIRA** Blue light induced infrared absorption is a rather annoying feature of Potassium Niobate, where - as implied by the name - the presence of blue light in the crystal induces an increased loss of infrared light dependent on the intensity of the blue. The physics behind this effect is not very clear and we will not go further into it. It has been studied at length in Mabuchi et al. [1994] and Shiv et al. [1995]. It is not easy to measure the BLIIRA losses  $\mathcal{L}_b$  in the SHG since the blue light is produced here, and so the light induced losses of the fundamental gets mixed up with the depletion of the fundamental because of the frequency conversion. So the BLIIRA is only measured in the OPO cavity, where it is inferred from the transmission or reflection signal of a probe beam for varying blue pump power in the crystal.

#### 4.2.4 Phase matching, thermal problems

The second harmonic generation at high IR and blue powers are greatly affected by thermal effects caused by heating of the crystal due to absorbed light. The dominant effect is probably thermal lensing [Polzik and Kimble, 1991, Ludlow et al., 2001], where the heating causes a local change in the refractive index giving it a gradient along the radial direction away from the beam, effectively creating a lens within the crystal. This for instance makes it a sensible task to reach the optimum phase matching temperature: when this temperature is approached from below, the blue power increases, but suddenly the resonator will become unstable and the blue power drops dramatically as shown in figure 4.4. When decreasing the temperature again it is not immediately possible to regain the same power - there is a sort of hysteresis in the system.

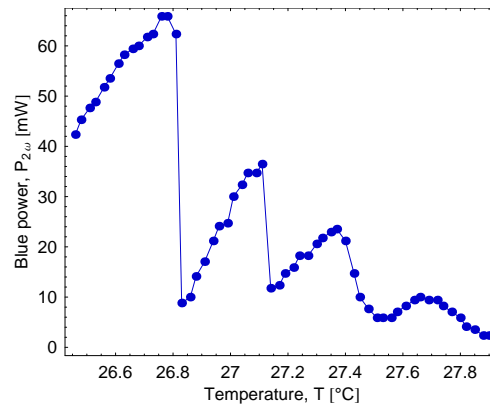


**Figure 4.4:** Second harmonic power as a function of temperature. The temperature was tuned from low to high in tiny steps to avoid large fluctuations from the electronic controller. Fundamental input power was 190 mW.

Compared to the data in figure 4.4 which does not at all look like a proper phase matching curve, the data in figure 4.5 are much closer to the expected dependence of generated blue power on the temperature. This phase matching curve was acquired at an IR power of only 13 mW which is low enough as to not cause any significant absorption and heating. A quick investigation showed that the pattern of figure 4.4 with sharp drops right after the peak of the phase matching curve starts to become clear for fundamental input powers around 50-60 mW. We need to operate at values far above this, so we cannot avoid the strong thermal effects, but in Polzik and Kimble [1991] it was found that there was no effect on the maximum attainable output power as long as this was below 0.5 W, so for our experiment (output below 300 mW) the thermal lensing is most likely more a nuisance than it is really a limiting factor in the performance of the SHG.

#### 4.2.5 Performance

When the SHG cavity is fully optimized, it can deliver up to 270 mW of second harmonic light out of the box with a pump power of 550 mW. Within the cavity this corresponds to  $\sim 320$  mW, or a conversion efficiency of 58%. Usually, though, we

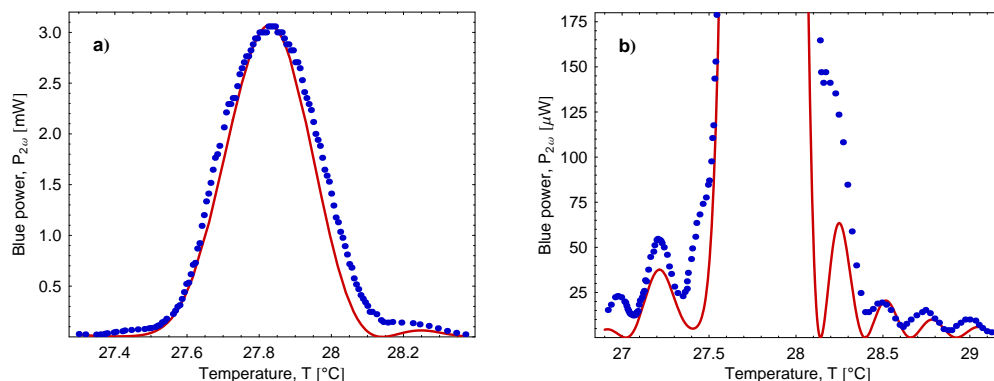


**Figure 4.5:** Two views of the same experimental phase matching curve - blue points - together with the theoretical Boyd-Kleinman function (3.11) - red line. In the measurement the fundamental power was 13 mW. The curve was reproducible with the same shape at a slightly different wavelength. The theoretical function, which employed the  $\text{KNbO}_3$  Sellmeier equations from Dmitriev et al. [1997], was normalized to the data, and the wavelength (860.225 nm) was adjusted to fit the data as well. Since the measured temperature in the oven is not necessarily the true temperature inside the crystal, the fitted wavelength is not the true wavelength of the fundamental either. **a)** In this full scale view we see that the temperature bandwidth of 0.3-0.4°C agrees well with theory/tabulated data. **b)** This view shows the entire measurement series at the lower output powers. There are some deviations from the calculated curve, but the general picture of small wiggles at either side of the peak is clear.

achieve lower values. Figure 4.6 shows the generated power for a not fully optimized cavity. Even so, the maximum 250 mW corresponding to 215 mW outside the cavity is still a decent pump for the OPO. The same figure also shows how the oven temperature must be cooled by a couple of degrees to reach optimal phase matching for high pump powers as compared to low powers. This is because the high powers inside the crystal dissipates heat, thus requiring a colder oven to maintain the right temperature.

## 4.3 OPO

### 4.3.1 Design

The OPO cavity is similar to the SHG: A bow-tie with the 10 mm temperature stabilized  $\text{KNbO}_3$  crystal placed between the 5 cm curved mirrors, the down-converted infrared escaping through one of the flat mirrors and the blue pump entering through one of the curved. The only difference is the output coupler which has a transmission of  $T_1 = 12.7\%$  and a slightly longer optical path length of 81 cm yielding a free spectral range of 370 MHz.

The output coupler has been chosen to optimize the amount of squeezing in the output field, which from figure 3.8 depends heavily on the pump parameter  $\epsilon$  (3.27) and the escape efficiency  $\eta_{\text{esc}}$  (3.26). These two parameters depend in opposite ways on  $T_1$  as can be seen from the definitions, so the best compromise has to be found.

From outside the SHG to just outside the OPO there is a quite large pump inten-

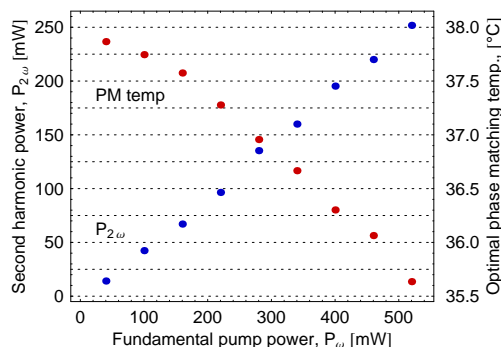


**Figure 4.6:** Generated intracavity second harmonic power (blue points, rising) and optimal phase matching temperature (red points, declining) for various infrared pump powers. The measured temperatures are those of the oven surrounding the crystal. The lower values needed for reaching phase matching at high pump powers are a clear sign of the pump and extra blue light heating the crystal.

sity propagation loss of around 25 %. Together with the blue coupling into the OPO of 91 % and an estimated reflection on the crystal surface of 2 % this gives a total transmission from outside the SHG to the OPO crystal of 67 %. If we take 270 mW as the maximum output from the SHG, this gives a pump power of 180 mW. The BLIIRA loss at this value was measured to be  $\mathcal{L}_b \approx 1.8\%$ . The pump power available for down-conversion into the resonant  $\text{TEM}_{0,0}$  is however further limited by the mode matching efficiency between the two cavities via the blue reference cavity. This mode matching is typically  $\sim 90\%$ , so the effective maximum pump value is  $P_p = 165$  mW. The passive losses in the OPO are  $\mathcal{L}_c \approx 0.7\%$ , while the nonlinearity is measured to be  $E_{\text{NL}} = 1.5\%/W$ .

Schori [2002] shows that the OPO threshold power is given by

$$P_{th} = \frac{(T_1 + \mathcal{L}_c + \mathcal{L}_b)^2}{4E_{\text{NL}}}. \quad (4.2)$$

With our parameters, inserting  $\epsilon = \sqrt{P_p/P_{th}}$  and  $\eta_{\text{esc}}$  in the squeezing expression (3.44) gives an optimum output coupling of  $T_1 = 12.1\%$  yielding a squeezing (not taking into account the finite detection efficiency) of -6.6 dB. For our value of  $T_1 = 12.7\%$  it is essentially the same. The threshold power becomes  $P_{th} = 385$  mW and the escape efficiency  $\eta_{\text{esc}} = 0.84$ .

It should be mentioned that several of these parameters may vary slightly between separate measurement sessions. Especially the blue power and the mode matchings to the blue cavity can take a long time to optimize, and even so they do not always reach the values mentioned here. A general rule is that the amount of squeezing obtained is proportional to the experimentalist's amount of patience!<sup>2</sup>

<sup>2</sup>This is probably true for any kind of experiment, though...

### 4.3.2 Parametric gain

A more direct way of estimating  $\epsilon$  is via the classical mode of operation of the OPO, the phase-sensitive parametric amplification of an injected signal beam. If we take the coupled equations of motion for the cavity field expectation values, (3.28) and its h.c., with a non-zero input field  $\langle \hat{a}_{\text{in}} \rangle$ , look for the steady state solution and square this, we get for the power  $P_c$  of the cavity field

$$\frac{P_c}{P_c^0} = \frac{1}{(1-\epsilon)^2} \cos^2 \varphi + \frac{1}{(1+\epsilon)^2} \sin^2 \varphi, \quad (4.3)$$

where  $P_c^0$  is the cavity power with no pump and therefore no amplification, and now  $\varphi$  is the phase of the pump with respect to the injected beam.

We see that, depending on the relative phase between the blue pump and the injected probe beam, the latter will be either amplified or deamplified. By observing the transmitted signal of this probe beam, we can directly infer the pump parameter from its maximum gain,

$$G = (1 - \epsilon)^{-2}. \quad (4.4)$$

Figure 4.7 shows a series of measurements of the parametric gain which gives a threshold power of  $P_{\text{thr}} = 358 \text{ mW}$ , which is on the same scale as the previously calculated  $385 \text{ mW}$ .

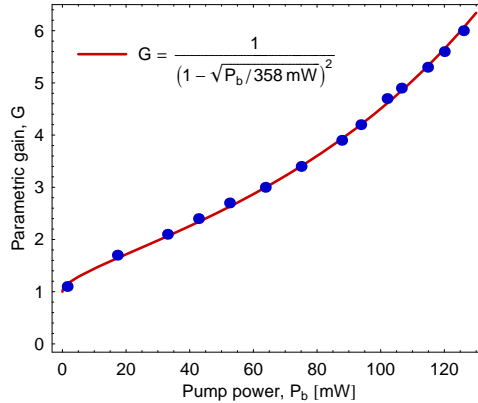


**Figure 4.7:** Maximum measured parametric gain for different pump powers -  $P_b$  is the effective pump, corrected for mode matching between SHG and OPO. Data points together with the best fit to the gain curve, (4.4), yielding a threshold power of  $P_{\text{thr}} = 358 \text{ mW}$ . The model does not take account of the intensity-dependent BLIIRA loss, which for low powers will give a smaller inferred  $P_{\text{thr}}$  than for higher powers (the difference is on the order of 10-20 mW). This can actually be seen in the plot in that the model slightly underestimates the gain in the low power region.

## 4.4 Measuring squeezing

### 4.4.1 Homodyne detector

The scheme of balanced homodyne detection, introduced by Yuen and Chan [1983], employs as already mentioned a coherent local oscillator beam mixing with the signal

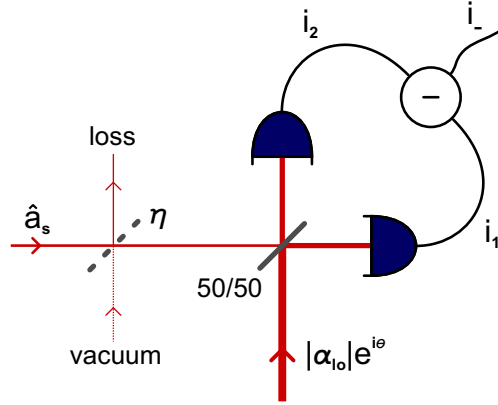


**Figure 4.8:** The homodyne detection scheme. The non-perfect detection efficiency is modeled by the fictitious beamsplitter (dashed). The local oscillator has an adjustable phase  $\theta$  relative to the signal beam. The photocurrents from the two detectors are subtracted and the resulting difference current is fed to the analysis apparatus.

on a 50/50 beamsplitter, creating a low frequency beat signal which is detectable as opposed to the  $\sim 10^{14}$  Hz of an optical signal. The photocurrents measured at the two beamsplitter output ports are subtracted, resulting in an electric current proportional to the expectation value of a certain quadrature of the quantum optic state being probed, as can be seen in a rough way from the model in figure 4.8:

The signal beam is described by the operator  $\hat{a}_s$  while the LO, which must be strong compared to the signal, is treated classically as  $|\alpha_{10}|e^{i\theta}$  with an adjustable phase relative to the signal. The two output fields are given by the usual beamsplitter relations with a  $\pi$  phase shift in one of the reflections:

$$\hat{a}_1 = \frac{1}{\sqrt{2}}(|\alpha_{10}|e^{i\theta} + \hat{a}_s), \quad (4.5)$$

$$\hat{a}_2 = \frac{1}{\sqrt{2}}(|\alpha_{10}|e^{i\theta} - \hat{a}_s). \quad (4.6)$$

The photocurrents produced in the detectors are proportional to the number of photons (or the photon flux) in the detected fields:

$$i_1 \propto \hat{n}_1 = \hat{a}_1^\dagger \hat{a}_1, \quad i_2 \propto \hat{n}_2 = \hat{a}_2^\dagger \hat{a}_2. \quad (4.7)$$

Subtracting the two currents gives

$$i_- = i_1 - i_2 \propto \hat{a}_1^\dagger \hat{a}_1 - \hat{a}_2^\dagger \hat{a}_2 = |\alpha_{10}|(\hat{a}_s e^{-i\theta} + \hat{a}_s^\dagger e^{i\theta}) = \sqrt{2}|\alpha_{10}|\hat{q}_\theta. \quad (4.8)$$

We can monitor this signal directly on the oscilloscope, which is what we do for the homodyne tomography in the next chapter. We can also feed the signal to a spectrum analyzer which measures the power spectrum (3.40). In the simplified approach taken here, this just corresponds to the variance of the current  $\langle(\Delta i_-)^2\rangle \propto |\alpha_{10}|^2 \langle(\Delta \hat{q}_\theta)^2\rangle$ . So the homodyne detection gives a signal which is proportional to the fluctuations of a selectable quadrature of the signal beam. It is also proportional to the power of the local oscillator, but this is kept constant, so it just defines our shot noise level.

For the homodyne scheme to work, the two arms of the setup must be finely balanced; this means the same transmission and reflection of the beamsplitter and the same electronic gain of the detectors. Our detectors are far from being perfect - one of them has to be attenuated by 6 dB for the coarse balancing with the other. The fine balancing of the two detectors is done by applying a strong classical modulation on the local oscillator beam. This modulation should be cancelled out in the difference current if the detectors are balanced in gain and phase - we achieve a suppression of 25-30 dB.

#### 4.4.2 Inefficient detection

From section 3.2.4 we know that the squeezing in the output field from the OPO is limited by the escape efficiency  $\eta_{esc}$ , and that the measured amount of squeezing is further limited by the non-unity detection efficiency  $\eta_{de}$ . The cause for the degradation is the same for both limiting factors: In the photon picture, the noise reduction is caused by correlations between photons created in pairs. If one photon of a pair is lost, either inside the cavity or simply because it is not detected, then the correlation is lost for this pair. All the different kinds of losses that arise in the detection can be modeled by a fictitious beamsplitter with intensity transmission coefficient  $\eta$  inserted in the beam path [Leonhardt, 1997]. This beamsplitter mixes in coherent vacuum through the unused port, thus decreasing the deviation from the SQL in the field fluctuations.

There are three main sources for the non-perfect detection efficiency: The quantum efficiency of the detectors, estimated to be  $\eta_{qe} = 0.98$  [Schori, 2002]. The propagation loss from the OPO to the homodyne setup; this gives a transmission coefficient of  $\eta_{prop} = 0.98$ . Finally, and most seriously, the imperfect mode match between signal beam and local oscillator. Only the part of the signal being inside the spatial mode of the LO is detected. The amount of mode matching can be determined by looking at the interference fringes between the LO and a strong beam from the OPO. The internal OPO cavity mode serves as a fixed spatial reference in the sense that a strong coherent beam injected and mode matched into the OPO will exit with exactly the same spatial mode as the squeezed output. With the LO and this reference beam adjusted to have the same power they can be optimized for best possible visibility  $V$  in the interference. We usually obtain a visibility of 98%. The transmission coefficient related to this mode matching is given by  $\eta_{mm} = V^2 = 0.96$  [Lam, 1998].

In conclusion, with all our sources of signal loss/vacuum admixture, the effective escape efficiency in the experiment is

$$\eta = \eta_{esc}\eta_{qe}\eta_{prop}\eta_{mm} = 0.84 \cdot 0.98 \cdot 0.98 \cdot 0.96 = 0.77 . \quad (4.9)$$

This number may also vary slightly from time to time: The homodyne mode matching is not always this good, and the cavity losses can change as well leading to a different  $\eta_{esc}$ .

#### 4.4.3 Spectrum analyzer

The difference signal from the homodyne detection is fed directly into a HP Agilent ESA-L spectrum analyzer which is set to measure at one specific frequency only ( $\omega/2\pi = 1.1$  MHz) instead of sweeping a frequency range as is the usual mode of operation for a spectrum analyzer. The instrument measures the power in the signal

within a specified resolution bandwidth (RBW) around the detection frequency. As mentioned in section 3.2.4, the level of the spectrum analyzer output is proportional to the RBW, but this is only a change of the shot noise level - the relative noise reductions (or enhancements) remain the same. A number of measurements are then carried out during some time interval, and if the noise level changes during this time, it will show up in the noise trace on the screen.

Every measurement point is integrated across a specified video bandwidth (VBW). A small VBW will average out the fluctuations, leading to a smoother curve, but this may also smooth out the sharp peak at the maximum squeezing quadrature [Bachor and Ralph, 2004]. We usually operate with RBW = 30 kHz, VBW = 100 Hz.

When we perform a measurement of a squeezed vacuum we need to acquire three traces: With both LO and signal blocked we obtain the electronic noise from the detection circuit. Unblocking the LO we obtain the shot noise level - the noise of the coherent vacuum. It is preferable to have this level as high above the electronic noise as possible. However, if the LO becomes too strong, the detectors will saturate. Usually we are around 8-10 dB above the electronic noise. The last trace acquired is with both LO and signal unblocked and scanning the LO phase, showing the amplification or deamplification of the vacuum noise.

#### 4.4.4 5 dB squeezed light

With the given losses, the total decay rate (HWHM of the resonance) of the OPO is

$$\frac{\kappa_1 + \kappa_L}{2\pi} = \frac{T_1 + \mathcal{L}_c + \mathcal{L}_b}{2\pi \cdot 2\tau} = \frac{370 \text{ MHz} (0.127 + 0.007 + 0.018)}{4\pi} = 4.5 \text{ MHz} . \quad (4.10)$$

At the detection frequency  $\omega/2\pi = 1.1 \text{ MHz}$ , this gives us the scaled parameter

$$\Omega = \frac{\omega}{\kappa_1 + \kappa_L} = 0.25 . \quad (4.11)$$

If we can further reach the parameters mentioned earlier;  $\eta = 0.77$  and

$$\epsilon = \sqrt{\frac{P_b}{P_{\text{thr}}}} = \sqrt{\frac{165 \text{ mW}}{385 \text{ mW}}} = 0.65 , \quad (4.12)$$

then it should be possible to reach a squeezing (3.44) and anti-squeezing (3.43) of, respectively

$$\chi^- = \frac{1}{2} - \frac{2\eta\epsilon}{(1+\epsilon)^2 + \Omega^2} = 0.14 = -5.5 \text{ dB}_{\text{sql}} \quad (4.13)$$

$$\chi^+ = \frac{1}{2} + \frac{2\eta\epsilon}{(1-\epsilon)^2 + \Omega^2} = 5.9 = 10.7 \text{ dB}_{\text{sql}} . \quad (4.14)$$

The  $\text{dB}_{\text{sql}}$  denotes that it is relative to the SQL of 1/2.

Figure 4.9 shows a SA trace of some of the best squeezing we have achieved. The average electronic noise has been subtracted from the two other traces and they have been normalized to the shot noise level. The result is a nice example of the characteristic ‘‘McDonald’s’’ or ‘‘gull wing’’ squeezing trace, extending from -5 dB to +9 dB. The gain was measured prior to this to be  $G = 8$ , corresponding to a pump parameter of exactly  $\epsilon = 0.65$ , so the resulting amounts of squeezing and anti-squeezing are not exactly the anticipated values, but they are reasonably close. The most probable

reason for the discrepancy is a degradation of the pump efficiency between the gain and the squeezing measurements - inserting  $\chi^- = -5$  dB in (3.44) and  $\chi^+ = 9$  dB in (3.43) returns the parameter values  $\eta = 0.76$  and  $\epsilon = 0.57$ .

The result obtained here is very close to that reported by Schori [2002] - he got  $\chi^- = -4.5$  dB,  $\chi^+ = 8 - 9$  dB - so it seems like this is as far as the current machinery can be pushed in terms of squeezing performance. For better results it would be necessary with higher numbers of either  $\eta_{\text{esc}}$  or  $\epsilon$  and preferably both. A higher pump efficiency could be achieved with more blue light, but this would at the same time increase the light-induced losses, leading to a lower escape efficiency. Another option would be to lower the threshold power by decreasing the output coupler transmission, but this would likewise decrease  $\eta_{\text{esc}}$ , and referring to figure 3.8 we see that of the two parameters,  $\eta_{\text{esc}}$  is the most important to increase. It certainly seems that the main limiting factor of the current setup is the  $\text{KNbO}_3$  crystal with its highly unattractive BLIRA losses. For comparison, the experiment by Lam et al. [1999] reaching -7 dB of squeezing had less than 0.2 % of total losses, making an escape efficiency of  $\eta_{\text{esc}} = 0.96$  possible while the pump power could go all the way to the threshold. Their OPO was significantly different from ours - a monolithic 7.5 cm long  $\text{MgO}:\text{LiNbO}_3$  crystal - and the wavelength was different as well - 1064 nm.

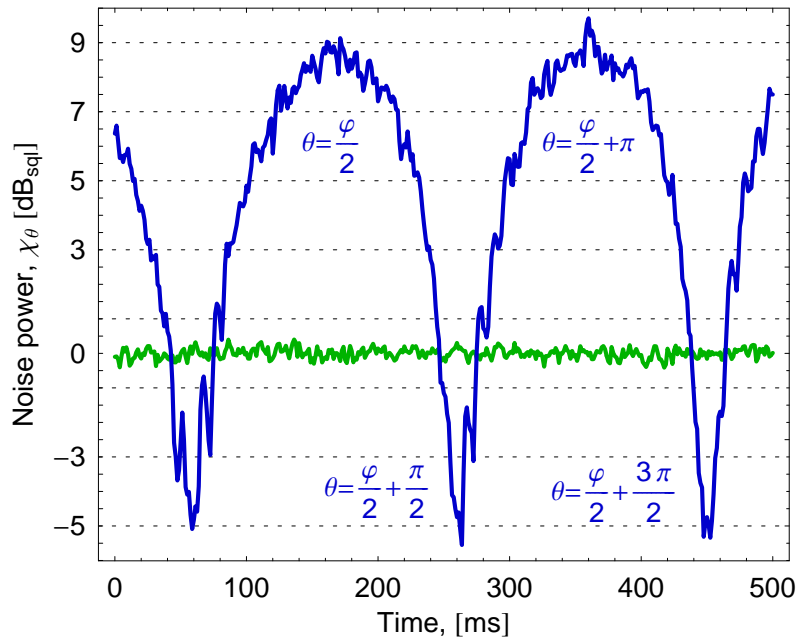


**Figure 4.9:** A spectrum analyzer trace showing 5 dB of squeezing. The electronic noise has been subtracted from the traces. RBW = 30 kHz, VBW = 100 Hz. The local oscillator phase was scanned linearly.

#### 4.4.5 Stability

Looking at the sketch of the setup, figure 4.1, one can see that it is actually one big interferometer with the local oscillator in one arm and everything else (SHG, OPO,

...) in the other arm. The two arms meet at the homodyne beamsplitter and it is clear that such a setup is very sensitive to phase jitter along the beam paths. We certainly observe this in practice when looking at the fluctuations of the spectrum analyzer traces. However, if we are standing very still in the lab, it is once in a while possible to reach a few seconds of stable phase as witnessed in figure 4.10. This is not impressive, and it is definitely not enough to keep the phase set at the maximum squeezing level. If we need to do that we must implement an electronic phase lock.

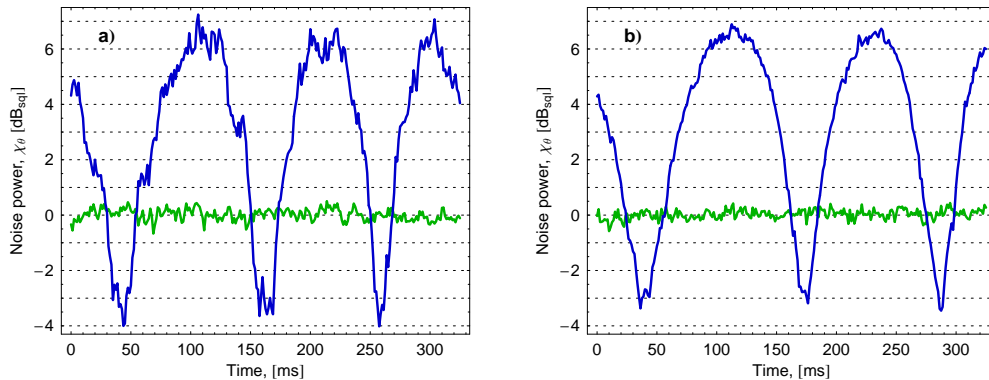


**Figure 4.10:** Two squeezing traces demonstrating the phase stability of the setup. **a)** A single recorded trace showing about  $-3.5$  dB squeezing. **b)** An averaged trace of 5 recordings taken within 10 seconds. The curve has been smoothed out and while the broad anti-squeezing top has retained its level, the narrow squeezing dip has suffered from the smoothing phase jitter and has decreased to  $-3$  dB. It should be noted that this fairly good trace was selected from maybe 10-15 traces, where for most of them the phase drifted a lot more.



## Chapter 5

# Quantum state tomography

As briefly introduced in section 2.3.2, it is possible to calculate or *reconstruct* a quantum state from a set of many similar homodyne measurements of identically prepared states. We have reconstructed the Wigner functions and density matrices for a number of different squeezed states, including squeezed coherent beams. The results are presented in this chapter.

### 5.1 Introduction

#### 5.1.1 Motivation

To fully describe a squeezed vacuum state, the variance of different quadrature phases is all we need to know. So in principle the measurement described in section 4.4.4 exhausts the amount of information we can extract about the output of the DOPO. However, we chose also to perform a reconstruction of the Wigner function, figure 2.7, for two reasons. The first was that a 3D plot of the Wigner function simply is a very nice way of pictorially representing the state. It is definitely not as quantitatively accurate as the McDonalds trace, but it gives a conceptually clearer view of the state.

The second, and more important reason was to gain knowledge about the methods involved in this reconstruction, as we will need it in the future for characterizing a single photon Fock state, as described in section 6.2. The way of describing a state entirely through its quadrature variances is basically limited to Gaussian states, for which the variances are the only parameters besides the location in phase space (amplitude/phase or position/momentum) necessary to characterize the state. For more complicated states this is not sufficient. The single photon Fock state, for instance, is very poorly described by its quadrature variance, which is just  $3/2$  in all directions (2.21). We need a more detailed description. For a general quantum state, pure or mixed, the density matrix or equivalently the Wigner function gives the full quantum picture of the state. So, if it is possible to obtain the Wigner function or the density matrix, then why not do so? And this is indeed possible, in particular for (but not limited to) quantum optical states via the method of quantum state tomography.

### 5.1.2 Presentation of the idea

As mentioned in section 2.3.2, it is not possible to measure points of the Wigner function directly due to the uncertainty principle, but it can be inferred from the marginal distributions through the relation (2.35). The marginal distribution  $\text{Pr}_\theta(q')$  along an angle  $\theta$  is like a shadow or a projection of the Wigner function: For every point  $q'$ , the probability density is the Wigner function integrated along the perpendicular direction  $p'$ . If the angle is changed, the Wigner function will be revealed from a different perspective and more information about it is gained. Looking at the “shadow” from all angles will fully reveal the Wigner function. This procedure is equivalent to the way 3D images of human bodies are obtained in medical tomography, hence the name.

In practice, quantum tomography is performed by sampling - for a series of different quadrature angles between 0 and  $\pi$  - a large number of homodyne measurements and thus obtaining a probability distribution for each individual angle. The data set must be sufficiently large in order to ensure good statistics. The Wigner function is then found by carrying out a numerical version of the inverse transformation of (2.35).

Thus, the full quantum state is determined, but the uncertainty principle is not violated since it takes several measurements of - in principle - an ensemble of identically prepared samples of the state. In the case of a continuous wave light mode this just means that the state should not change within the time of data acquisition.

The fact that the Wigner function (or any  $s$ -parameterized quasi-probability distribution) can be reconstructed from the marginal probability distributions was realized by Vogel and Risken [1989], and the first experimental realization of the method was carried out by Smithey et al. [1993], who reconstructed the Wigner function of a weakly squeezed state. They also introduced the term “optical homodyne tomography”. Breitenbach et al. [1997] reconstructed a strongly squeezed coherent state and investigated the photon number distributions, while Lvovsky et al. [2001] were the first to do a tomographic measurement of the single photon Fock state, showing negative values of the Wigner function. A different method for reconstructing the density matrix (and subsequently the Wigner function) was developed by D’Ariano et al. [1994] and Leonhardt et al. [1996]. This method can be used to directly build the density matrix on the fly from statistical averages of sampled quadrature data. As explained in section 5.4.1 we also implemented this method, but with dissatisfactory result.

These methods for reconstructing the Wigner function or density matrix, developed through the first half of the 90’s, are excellently summarized in the book “Measuring the quantum state of light” [Leonhardt, 1997] by one of the pioneering researchers. It is basically a cookbook in the numerical implementation of the methods, and it is based on this we have reconstructed the squeezed states.

## 5.2 Noise traces

In a spectrum analyzer, the noise power  $\langle(\Delta i_-)^2\rangle$  of the input signal is immediately calculated and displayed. It does not tell us about the raw signal  $i_-$ , which is the direct measure of the probed quadrature (4.8) and as such is what we need for building

up histograms of the marginal probability distributions. To record the difference photocurrent we first mix it with an electrical local oscillator at 1.1 MHz and then amplify it after a 30 kHz low-pass filter. This corresponds to the demodulation taking place in the spectrum analyzer, where the signal within the RBW of 30 kHz around 1.1 MHz is detected. The amplified signal is then digitized, in this case we use a LeCroy 9354C digital storage oscilloscope with a vertical resolution of 8 bit and capable of a sampling rate of 2 GSa/s. However, because of the detection bandwidth we only sample at 50 kSa/s. In order for the numerical method to produce a faithful reconstruction, we need to be sure that there are no phase drifts between LO and signal beam within the detection period. Therefore we record each trace for 2 seconds while the LO phase angle is scanned about  $2\pi$ , giving a total of 100,000 points per trace. In this section, a selection of the acquired noise traces for the various states of the detected light field is presented.

### 5.2.1 Electronic noise, coherent vacuum and bright coherent beam

Figure 5.1 is the noise recorded with no light incident on the detectors, that is, the electronic noise of the detection circuit, while figure 5.2 shows the vacuum noise with a local oscillator of 5 mW. The power (variance) of the vacuum trace is only 3 dB above the electronic level - this means that electronic noise comprises as much as half of the noise in the vacuum trace! For the noise power levels measured by the spectrum analyzer, the noise in a 5 mW LO is 8-10 dB above electronics, amounting to electronic noise that is less than a fifth of that in the new acquisition scheme. We have good reason to believe that the majority of the added noise is due to the mixer (Mini-Circuits ZP-3LH) which did not behave quite as expected. Later, in figure 5.5, we will also see that there is a strange 13 Hz oscillation of the electronic noise power. This is still unaccounted for, but is likely to also originate in the mixing process.

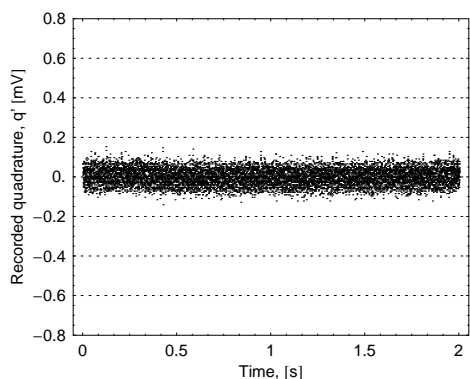


**Figure 5.1:** Noise of the electronic detection circuit. The full dataset consists of 100,000 points within 2 seconds.

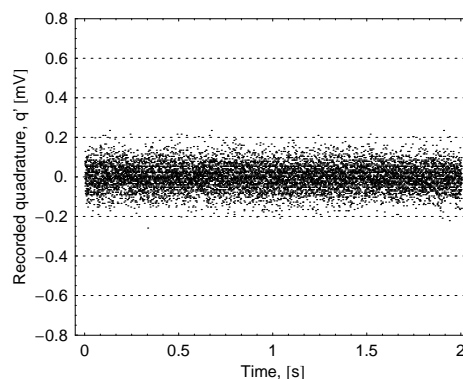


**Figure 5.2:** Noise of the vacuum state with a local oscillator of 5 mW. Only twice as much noise as the pure electronic noise.

When measuring variances, as in the spectrum analyzer traces, the electronic noise can easily be compensated for. The different noise terms are uncorrelated, and so they add in quadrature [Bachor and Ralph, 2004]:  $\langle(\Delta i_{\text{total}})^2\rangle = \langle(\Delta i_{\text{elec}})^2\rangle + \langle(\Delta i_{\text{other}})^2\rangle$ . The interesting noise is therefore recovered just by subtracting the electronic variance from the total trace. When measuring the raw currents, it is clearly not as simple to

distinguish the signals from the photodetectors and from the circuitry. Therefore, the data we use for the reconstructions include the electronic noise, with the effect that the inferred amount of squeezing is far lower than it really is (see next subsection). All the noise traces have been calibrated so that the variance of the vacuum trace equals the SQL of  $1/2$ . We should just keep in mind that this level as well as all other traces is strongly biased by the incorporation of the electronic noise.

An advantage of the direct quadrature measurements over the variance approach is that it is possible to distinguish bright states from vacuum. Here, “bright” means a field excitation different from zero, but in our case still a very faint beam ( $\alpha \approx 2$ ) since we are limited by the amplitude resolution of the oscilloscope. As mentioned in the setup overview (section 4.1), we produce this excitation by a 1.1 MHz modulation of a coherent beam injected into the OPO and further propagating towards the homodyne detector. This beam may then be squeezed if the pump beam is switched on, or it may just be a coherent state. For the case of no pump we get the trace in figure 5.3. We see how the quadrature mean value oscillates as the detected quadrature angle is scanned via the LO phase. The noise on the other hand is constant and of the same magnitude as the vacuum as expected. If we monitored this state on the spectrum analyzer instead, we would not be able to tell it from the vacuum.

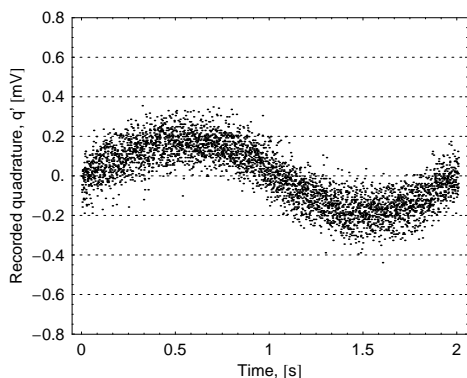


**Figure 5.3:** The signal of a “bright” coherent state. The excitation can be read off to be  $|\alpha|^2 = (q^2 + p^2)/2 \approx 2$ .

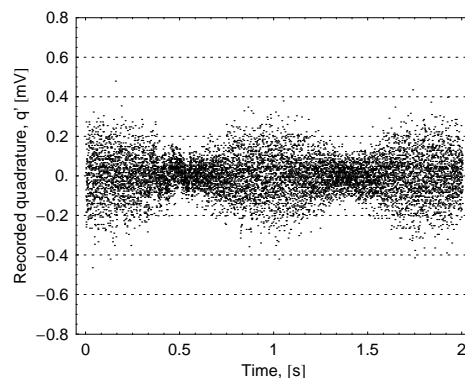


**Figure 5.4:** The squeezed vacuum state. Because of large electronic noise it is hard to see that it is squeezed below the level of figure 5.2, but it is.

If we for a moment forget about the electronic noise and trust the scaling of the noise trace, we get that the photon number of the state - by (2.26) equal to the squared magnitude of the classical excitation  $\alpha = (q + ip)/\sqrt{2}$  - is  $\langle \hat{n} \rangle = |\alpha|^2 = (q^2 + p^2)/2 \approx 2$ . Since it is a freely propagating field (in contrast to a cavity field), it is in fact a photon flux; the number of photons per second per Hz bandwidth. It should also be noted that it is the number of photons in the sideband at 1.1 MHz. The total number is way higher but we do not detect the carrier frequency.

### 5.2.2 Squeezed vacuum

A trace for a squeezed vacuum is shown in figure 5.4. This is, also even more so than the Wigner function plots, the most obvious illustration of the squeezing of the vacuum fluctuations: The noise is quite apparently being amplified or deamplified

depending on the phase.

How good is the squeezing? We can try to recreate the usual McDonalds variance trace from the squeezed vacuum, coherent vacuum and electronic data. For this we just need to group the data points together and calculate the variance for the individual consecutive groups, corresponding to the spectrum analyzer's integration over the VBW. This is done in figure 5.5 a). for the three traces. In figure 5.5 b) the mean electronic noise has been subtracted from the two other traces in the exact same way as we did earlier for the spectrum analyzer traces. We see here how high the electronic noise floor is, and that it severely limits the directly detected noise reduction: In a) the squeezing below shot noise level is -2 dB, while the compensated traces in b) show a reduction of -4 to -6 dB.

For comparison we measured the same state on the spectrum analyzer, the result given in figure 5.6. This gives a far more trustworthy number of -3 to -4 dB. The reason for the larger noise reduction of figure 5.5 b) is probably the proximity of the electronic noise level to the other levels, which makes the subtraction unreliable. In any case, this is not so relevant since we can only use the numbers from figure 5.5 a), that is, the -2 dB. To retrieve the full potential squeezing we would need less electronic noise or a stronger local oscillator.

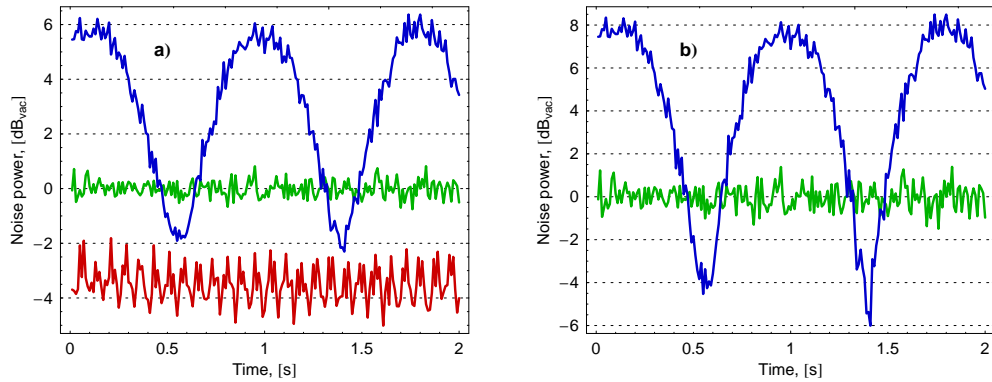


**Figure 5.5:** Calculated variances for the traces in figs. 5.1, 5.2 and 5.4. **a)** All three traces. The electronic noise is very high, and there are also some peculiar oscillations. **b)** The mean electronic noise has been subtracted from the vacuum and the squeezed vacuum traces. The amount of squeezing given here is not far from the "real" squeezing in the beam. However, because it is not easy to subtract the electronic noise in the quadrature distributions, it is the data from **a)** that will be used for the reconstruction, reducing the apparent squeezing to -2 dB.

In fact, the degrading effect of the electronic noise floor can be incorporated into the effective escape/detection efficiency. From (3.43) and (3.44), the total efficiency can be estimated from the observed squeezing and anti-squeezing:

$$\eta = 2 \frac{(\chi^+ - \frac{1}{2})(\frac{1}{2} - \chi^-)}{\chi^+ + \chi^- - 1}. \quad (5.1)$$

Let  $E$  denote the amount of electronic noise (on the usual scale, with  $\text{SQL} = 1/2$ ). The effect of adding the electronic noise to the other measured noise levels is just to lift all variances by  $E$  - the vacuum level becomes  $1/2 + E$  instead of  $1/2$ , and the same

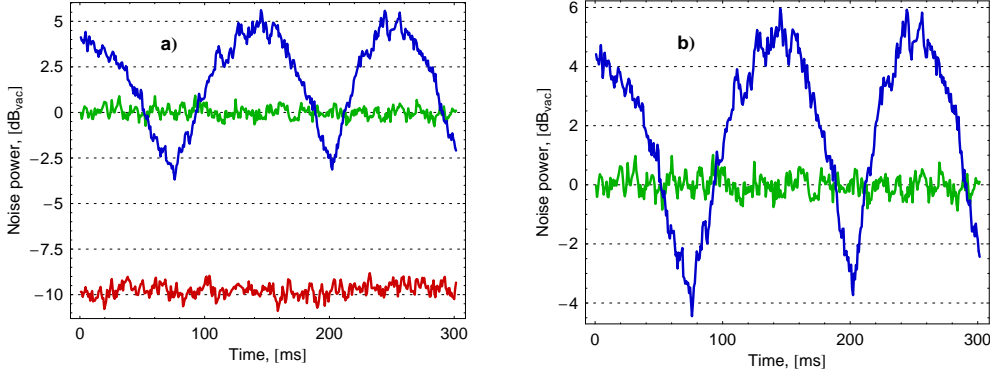


**Figure 5.6:** For reference, these are the spectrum analyzer traces of the same states as in figure 5.5. The electronic noise is much less here, so the large amount of extra noise in the tomography detection circuit must occur in the stages after the photocurrent subtraction, since everything before is common for the two measurements.

for  $\chi^+$  and  $\chi^-$ . Normalizing all levels to the new vacuum level and inserting in (5.1) gives for the total efficiency

$$\eta = \frac{1}{1 + 2E} \eta_c, \quad (5.2)$$

with  $\eta_c$  the “clean” efficiency before addition of electronic noise - this is the effective escape efficiency we have used before. So, effectively the electronic noise reduces the efficiency by a factor  $\eta_{el} = 1/(1 + 2E)$ .<sup>1</sup>

Taking from the corrected spectrum analyzer trace, figure 5.6 b), the estimated values  $\chi_+ = 6$  dB and  $\chi_- = -4$  dB gives for the clean efficiency  $\eta_c = 0.75$ , while the total measured efficiency from figure 5.5 a) is  $\eta = 0.42$ , using  $\chi_+ = 6$  dB and  $\chi_- = -2$  dB. This means that the electronic efficiency factor is  $\eta_{el} = \eta/\eta_c = 0.56$ , corresponding to  $E = 0.39$ , which is a level of  $E/(1/2 + E) = -3.6$  dB below the measured vacuum level, in good agreement with the data, figure 5.5 a).

The very poor detection efficiency caused by the amount of electronic noise is a dominant problem of this measurement series. Because of that, the reconstructed states are quite far away from the true states, but even so, they still show all their characteristic features, so the results and the road towards them provide us with a good understanding of the workings of optical homodyne tomography, which was our primary objective.

### 5.2.3 Bright squeezed state

In the description of squeezed vacuum we have two phases to care about: Half the pump phase  $\varphi/2$ , which is the direction of the anti-squeezing axis, and the local oscillator phase  $\theta$ , determining the quadrature  $q_\theta$  to be probed. Since vacuum has no phase,  $\varphi/2$  can be arbitrarily set to, for instance, 0. In the case of a coherent input at the fundamental wavelength into the OPO, the relative phase between this beam and the pump becomes important. We choose to set the phase of the input beam  $\varphi_{in}$  to 0,

<sup>1</sup>Again, a scaling to SQL = 1 would be a little more natural to use. The formulas (5.1) and (5.2) would then be  $\eta = (\chi_+ - 1)(1 - \chi_-)/(\chi_+ + \chi_- - 2)$  and  $\eta = \eta_c/(1 + E)$ .

causing the Wigner function to be centered on the positive  $q$ -axis. In reality it is not the phase of the pump, but the phase of the input beam we change, but we have the freedom of choosing one phase arbitrarily.

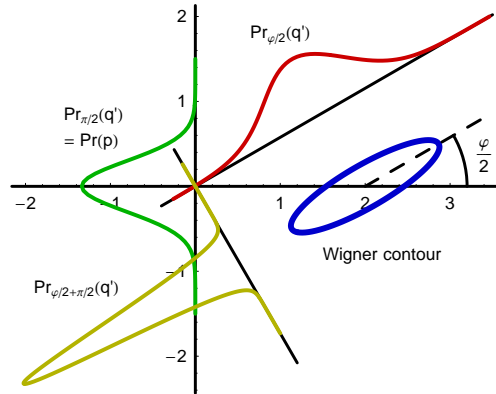


**Figure 5.7:** A bright squeezed state with phase  $\theta_{in} = 0$  and a squeezing angle somewhere between amplitude and phase. The marginal distributions for various quadrature angles are shown. The distributions oscillate around 0 while “breathing” - this is what we see in the noise traces.

The situation is now as depicted in figure 5.7: Depending on the pump phase, the coherent beam can now be squeezed in either its amplitude ( $\varphi/2 = \pi/2$ ), its phase ( $\varphi/2 = 0$ ), or something in-between. The figure also shows the quadrature distributions  $Pr_{\theta}(q')$  for various detection angles  $\theta$ , and how the distribution oscillates around 0 while the width is changed.<sup>2</sup>

Figures 5.8, 5.9, and 5.10 show, respectively, the noise traces obtained for an amplitude squeezed state, a phase squeezed state, and a state with an intermediate squeezing angle (corresponding to figure 5.7). We see how the amplitude squeezed state has been decreased in the  $q$  (amplitude) quadrature, not only the noise but also the amplitude itself. Conversely, the phase squeezed state has been amplified in the  $q$  quadrature - for both amplitude and noise - while the decreased phase fluctuations leads to a narrower trace in the  $p$  quadrature.

## 5.3 Inverse Radon transformation

### 5.3.1 The reconstruction method

Implementing the inversion of the Radon transformation (2.35) is by far the simplest of the two reconstruction methods we have employed. This inverse Radon transfor-

<sup>2</sup>An alternative, but equivalent picture of this is the freely propagating wave packet: For a freely propagating beam (as opposed to detection on the photodiode surface,) the wavepacket  $|\psi(q)|^2$  in the coordinate representation corresponds to the measured quadrature distribution  $Pr_0(q)$  in the  $\theta = 0$  direction. While propagating, the wave packet oscillates back and forth while “breathing” - its width changes. In the  $q/p$ -diagram, this would amount to the contour rotating around  $(0,0)$  with the relative pump/input phase  $\varphi/2$  kept constant. This oscillation takes place at the optical frequency of the light, while in the other picture the oscillation time is determined by the local oscillator phase, controlled by us.

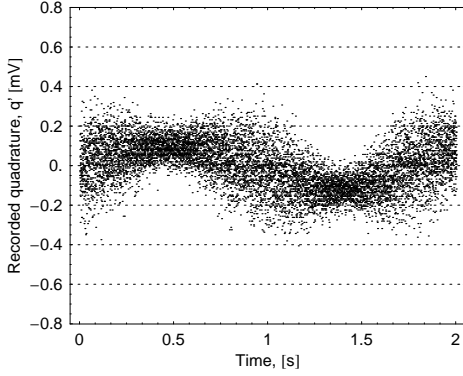


**Figure 5.8:** The amplitude squeezed bright state, with its quite characteristic noise trace.

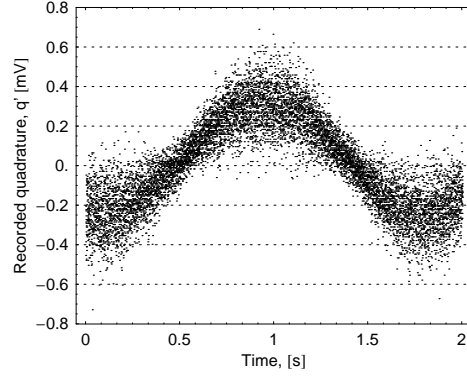


**Figure 5.9:** The phase squeezed bright state. The noise in the amplitude quadrature is strongly increased.

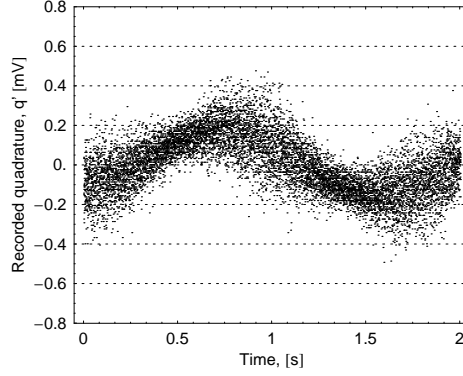


**Figure 5.10:** When the pump and the input beam are not either in or out of phase, the squeezing will take place in an intermediate quadrature as shown here.

mation is given by [Leonhardt, 1997]

$$W(q, p) = \frac{1}{4\pi^2} \int_{-\infty}^{\infty} \int_0^{\pi} \int_{-\infty}^{\infty} \text{Pr}_{\theta}(q') |r| \exp[ir(q \cos \theta + p \sin \theta - q')] dr d\theta dq'. \quad (5.3)$$

The r-factors can be extracted as an integration kernel:

$$K(x) = \int_{-\infty}^{\infty} |r| e^{irx} dr; \quad (5.4)$$

$$W(q, p) = \frac{1}{4\pi^2} \int_{-\infty}^{\infty} \int_0^{\pi} \text{Pr}_{\theta}(q') K(q \cos \theta + p \sin \theta - q') d\theta dq'. \quad (5.5)$$

The kernel is not a regular function and so, for the numerical implementation, it needs to be regularized or filtered. One way of doing that is by stopping the integration at the spatial cutoff frequency  $k_c$ :

$$K(x) = \int_{-k_c}^{k_c} |r| e^{irx} dr. \quad (5.6)$$

The cutoff frequency determines the spatial resolution of the reconstructed Wigner function - the smaller features we need to resolve, the higher we must set the cutoff. But it should not be set too high either. The regularized kernel is an oscillating function, so far away from the location in phase space of the center of the Wigner function there will always be oscillations, but a too high frequency leads to large unwanted - and unphysical - oscillations close to the center as well. Therefore  $k_c$  must be carefully chosen, either based on a priori knowledge of the state or by trial-and-error. For all the states measured here, a value of  $k_c = 4$  turned out to be the best compromise. In section 5.3.3, after the presentation of the various reconstructed Wigner functions, it will be shown how the quality of the reconstruction depends on the various adjustable parameters, including the filtering,  $k_c$ .

For the reconstruction we only need data within a phase angle of  $\pi$ . Therefore, we crop the data set manually, retaining the points between two squeezing minima (for squeezed vacuum) or the points between a maximum and a minimum  $q'$  value (for bright states). These arbitrary croppings correspond to setting the phases  $\varphi/2 = \pi/2$  or  $\varphi_{\text{in}} = 0$ , respectively. To populate the marginal distribution histograms, we partition the new data set into a number  $N_\theta$  of equal sized subsets. We take all points in one partition to have the same  $\theta$ , and because we scan the phase linearly, the  $N_\theta$  angles are evenly distributed between 0 and  $\pi$ . For each  $\theta$ -partition, we now build a histogram of the  $q'$  distribution, choosing a suitable bin width  $dq'$ . Because of the limited vertical resolution (8 bit = 256 channels), we always choose  $dq'$  to be a multiple of the spacing between the amplitude channels. This ensures that each bin contains the same number of channels, thus avoiding the artificial bias that could otherwise arise from uneven binning. With the marginal distributions so prepared, the Wigner function is calculated by replacing the integrals in (5.5) by summations.

### 5.3.2 Gallery of reconstructions

In figs. 5.11 to 5.15 the results of the reconstruction of the noise traces in the previous section are visualized in 3D plots as well as contour plots which more clearly show the shape, orientation and location in phase space. All reconstructions employed the same parameters:  $k_c = 4$ ,  $N_\theta = 20$  and  $dq' = 0.41$ , the last number corresponding to 6 amplitude channels per  $q'$  bin. The small wiggles on the function floors are artifacts from the numerical reconstruction. The parameters were chosen to minimize those wiggles.

Note that for some of the plots, the coordinate system is not centered on (0,0).

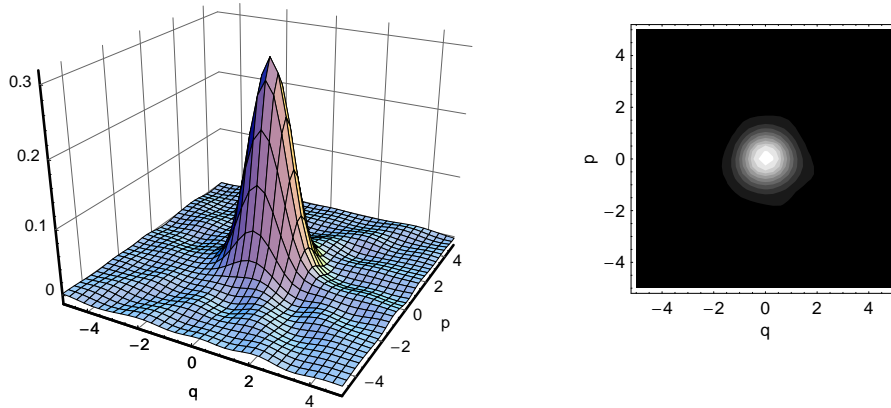


**Figure 5.11:** Coherent vacuum state. All datasets have been calibrated to yield the uncertainty in this function equal to the SQL - the standard deviation can be seen to be  $\sqrt{1/2} = 0.71$ .

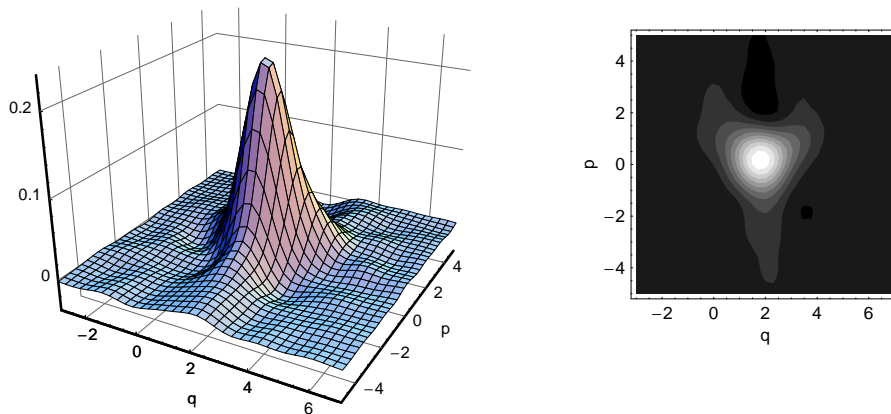


**Figure 5.12:** Bright coherent state. Centered at  $(2,0)$ , the excitation is  $|\alpha|^2 = (q^2 + p^2)/2 = 2$ .

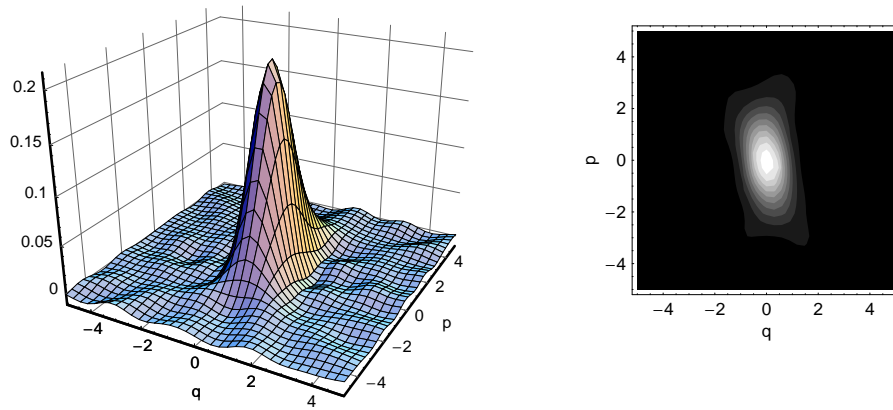


**Figure 5.13:** Squeezed vacuum state. The squeezing is in the  $q$ -direction by our choice of  $\varphi/2 = \pi/2$ . The ratios of the minor and the major axes to the vacuum diameter are 0.8 and 1.8, respectively, corresponding to -2 dB squeezing and 5 dB anti-squeezing - agreeing well with the variance trace in figure 5.5 a).

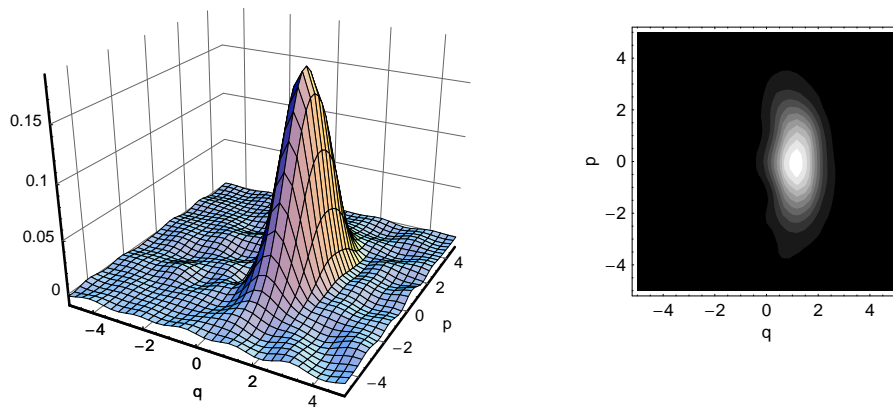


**Figure 5.14:** Bright amplitude-squeezed state. Compared to the coherent state in figure 5.12 this one has a weaker amplitude as well as less noise in the amplitude at the expense of increased phase noise.

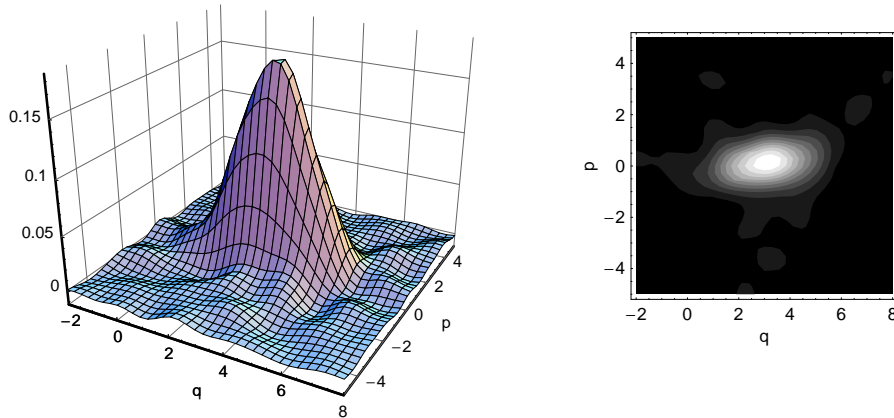


**Figure 5.15:** *Bright phase-squeezed state. This state has a stronger, but also more noisy amplitude than the coherent state. The phase, on the other hand, is less uncertain.*

### 5.3.3 Optimization

As we see, the Wigner functions can be quite nicely reconstructed using the inverse Radon transformation. However, a major drawback of this method is the need to manually find a best cutoff frequency for the regularization. This optimum frequency is not very solidly grounded in neither the physics nor the numerics - one can certainly make a qualified guess, but it will still be necessary to check other values to see whether they offer a more correct picture. And it is not very appealing that one has to judge the quality of the reconstruction based on presupposed ideas of what the function *should* look like. The simple regularization method used here is not the only one possible. For instance, Breitenbach [1998] uses a slightly more sophisticated method which is able to quantify the amount of distortion to the Wigner function caused by the regularization. But even with this method it was necessary for him to search for the best parameter.

Figure 5.16 shows the effect of either too low or too high cutoff frequency. A too low value will smooth out the function, while a high value will introduce increasingly more small wiggles.

The optimization of the  $N_\theta$  and  $dq'$  parameters are more straightforward: The finer the data partition, the better result - this means a high  $N_\theta$  and a low  $dq'$ . This is only as long as we do not dilute the data set too much. For example, it does not make any sense to make  $dq'$  smaller than the amplitude resolution.

In the Wigner functions presented earlier we used the parameters  $N_\theta = 20$  and  $dq' = 0.41 = 6 \text{ AR}$ , with AR denoting the amplitude resolution of the data. Figure 5.17 shows the reconstruction results with a lower number of angle partitions, while the results with fewer  $q'$  partitions are shown in figure 5.18.

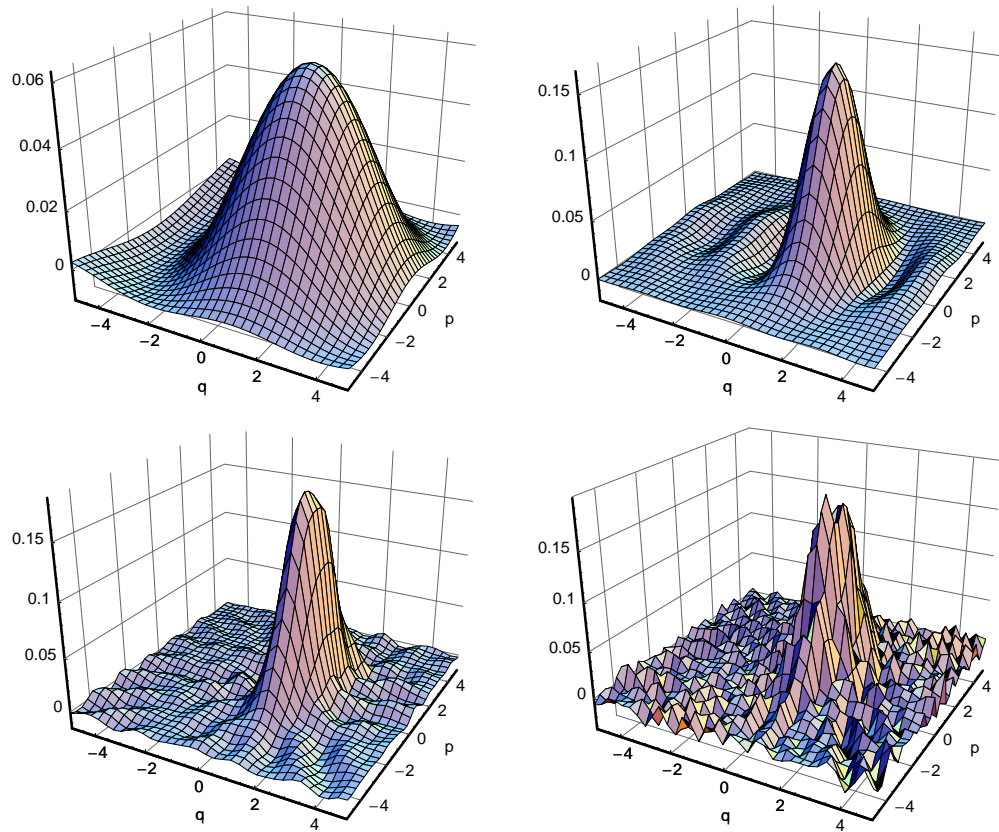


**Figure 5.16:** The effect of wrong choices for the cutoff frequency. These figures should be directly compared to the amplitude squeezed state in figure 5.14 with a cutoff parameter of  $k_c = 4$ . From top left, the parameters for the four figures are  $k_c = 1$ ,  $k_c = 2.5$ ,  $k_c = 5.5$  and  $k_c = 9$ . The 2.5 and 5.5 values are almost acceptable, but they are clearly worse than 4, showing how precisely this parameter must be chosen.

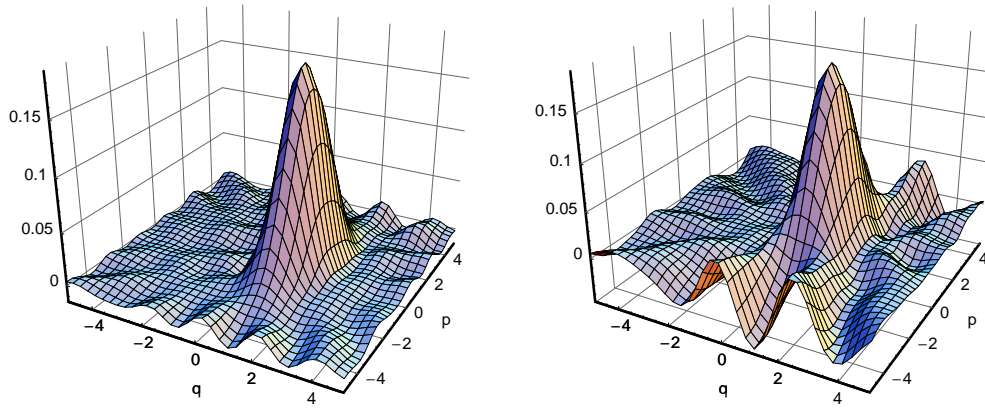


**Figure 5.17:** The effect of a coarser partition of the quadrature angles.  $N_\theta = 10$  in the left picture and  $N_\theta = 6$  in the right.

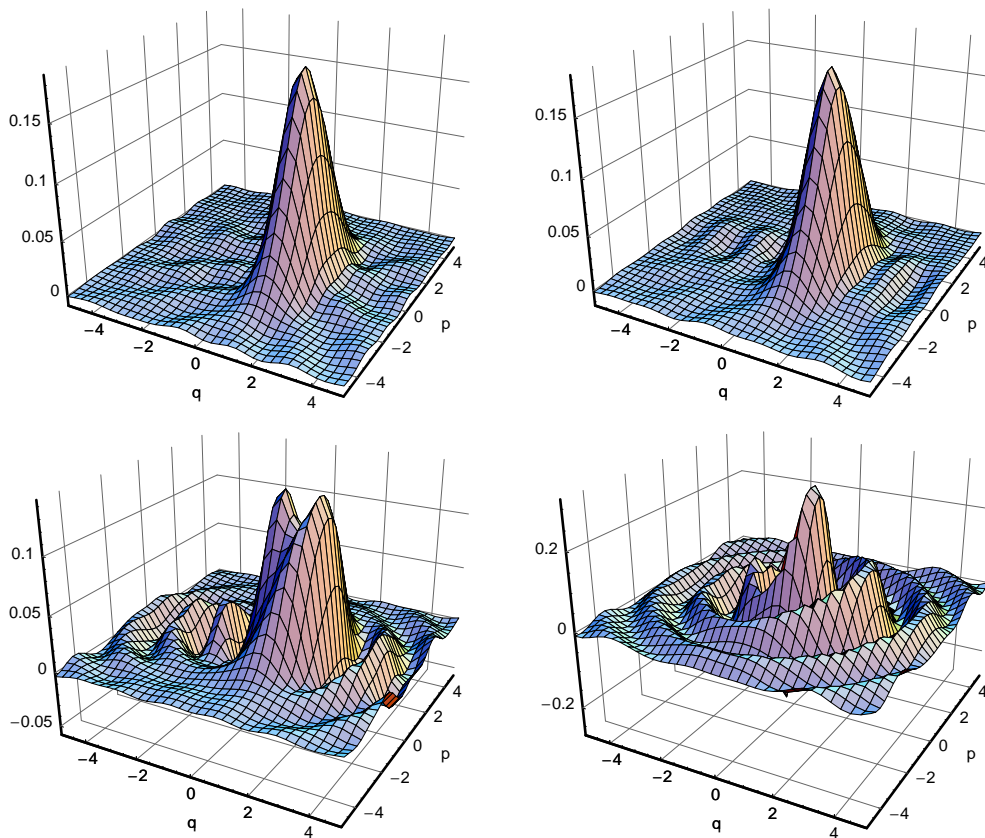


**Figure 5.18:** The effect of a coarser partition of the quadrature amplitudes. From top left,  $dq' = 0.67 = 10 \text{ AR}$  (16 bins),  $dq' = 0.89 = 13 \text{ AR}$  (12 bins),  $dq' = 1.1 = 16 \text{ AR}$  (10 bins) and  $dq' = 1.3 = 20 \text{ AR}$  (8 bins).

## 5.4 Density matrices

### 5.4.1 Two reconstruction procedures

As soon as the Wigner function of a state is known, it is possible to calculate the density matrix as well. In the Fock state representation, using (2.36) it is given by

$$\begin{aligned}\rho_{mn} &= \langle m | \hat{\rho} | n \rangle = \text{Tr}[\hat{\rho} |n\rangle \langle m|] \\ &= 2\pi \int_{-\infty}^{\infty} \int_{-\infty}^{\infty} W(q, p) W_{mn}(q, p) dq dp ,\end{aligned}\quad (5.7)$$

where  $W_{mn}(q, p)$  is the Wigner function of the operator  $|n\rangle \langle m|$ . It is given explicitly by [Breitenbach, 1998]

$$W_{mn}(q, p) = \frac{(-1)^n}{\pi} \sqrt{\frac{2^{m+n} n!}{2^n m!}} (q - ip)^{m-n} e^{-(q^2 + p^2)} L_n^{m-n}(2q^2 + 2p^2) . \quad (5.8)$$

$L_n^{m-n}$  are the associated Laguerre polynomials.

Numerically we calculate the density matrix by sampling the Wigner function in a sufficiently large number of points  $(q, p)$  and performing (5.7) as a summation.

As mentioned in the introduction, there is another way of reconstructing the density matrix, the “sampling method” (in lack of a more descriptive name) introduced by D’Ariano et al. [1994]. This method samples the density matrix elements directly from the data, using as an integration kernel the so-called *pattern functions*  $f_{mn}(q')$ , which are oscillatory functions closely related to the wavefunctions of the Fock states. They are efficiently generated numerically via recursion relations for the wavefunctions [Leonhardt et al., 1996].

The sampling method has the advantage over the inverse Radon transformation that there is no parameter like the cutoff frequency of the filtering that needs to be optimized based on more or less qualified guesses. Instead, another cutoff is necessary, namely the dimension of the reconstructed density matrix. It must be assumed that the matrix elements become negligible for high quantum numbers,  $m, n$ , such that the matrix can be truncated beyond a certain index/dimension  $d$ . This truncation point makes more sense physically than the spatial cutoff frequency of the inverse Radon method.

In principle, therefore, it should be more straight-forward to obtain a reliably reconstructed density matrix this way, so we implemented the sampling method as well. However, it turned out that this method required even more parameter tuning than the Radon inversion, and even for the best results there were strange artifacts for especially the higher quantum numbers. Although it cannot be completely ruled out that some of those artifacts are indeed features of the dataset, it seems much more likely that they originate in the statistical processing of the data. Indeed, since there is no spatial filtering involved, the sampling method is more sensitive to statistical errors.

In the end, the density matrices presented in the next section were calculated by the first method, that is, via the already reconstructed Wigner functions from the last section. These functions - and hence the density matrices - may be filtered, in effect smoothing out any finer details of the state, but the results are definitely more trustworthy than those obtained by the sampling method - at least for the datasets at our disposal.

### 5.4.2 Reconstructed density matrices

For the calculation of the density matrices we used almost the same Wigner functions as presented in section 5.3.2, with the only difference that the  $dq'$  bin width was improved from 6 AR to 2 AR, which made a small, but noticeable difference to the resulting matrix.

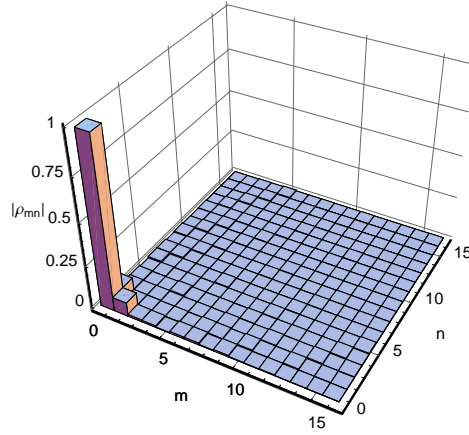


**Figure 5.19:** Reconstructed density matrix of the vacuum state, calculated from the Wigner function in figure 5.11.

For the vacuum state, the density matrix should be 1 in  $m, n = 0$  and 0 everywhere else. Figure 5.19 shows that this is indeed the case for the reconstructed matrix. The small, but nonzero first off-diagonal elements are insignificant; a calculation of the theoretical density matrix for a coherent state shows that this corresponds to a mean photon number of  $\sim 1/200$  - essentially vacuum.

The reconstructed density matrix of the bright coherent state is shown in figure 5.20. Calculating the mean photon number gives

$$\langle \hat{n} \rangle = |\alpha|^2 = \sum_{n=0}^{n_{max}} n \rho_{nn} = 2.42, \quad (5.9)$$

corresponding to an excitation of  $\alpha = 1.56$ . The calculated photon number variance is however  $\langle (\Delta \hat{n})^2 \rangle = 2.65$ , which means that the state is more noisy than an ideal coherent state. This extra photon number noise can of course be attributed to the electronic noise. It is also the reason why the mean photon number of 2.42 is larger than the estimate of 2, based on the state's position in phase space, figure 5.12.

For a coherent state, the theoretically predicted density matrix is, from (2.23):

$$\rho_{mn}^{coh} = e^{-|\alpha|^2} \frac{\alpha^m (\alpha^*)^n}{\sqrt{m!n!}}, \quad (5.10)$$

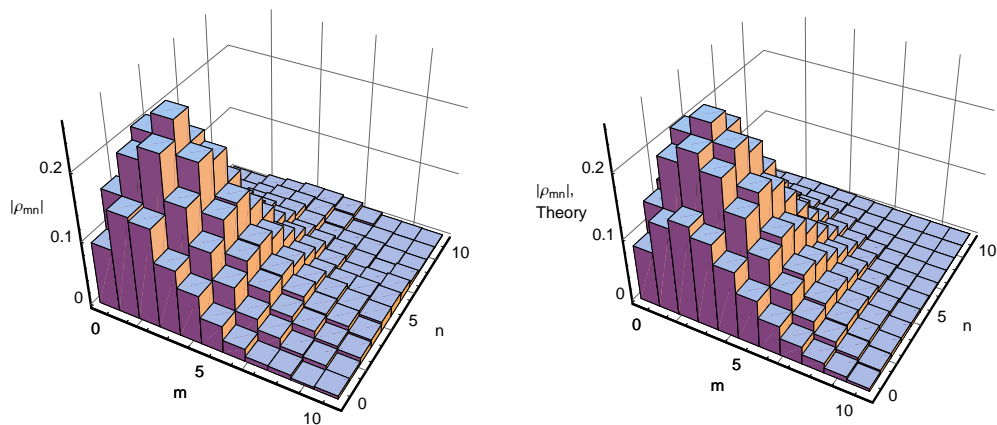


**Figure 5.20:** *Left:* Reconstructed density matrix for the coherent state. *Right:* Theoretically expected density matrix for a coherent state with mean photon number  $|\alpha|^2 = 2.42$ , corresponding to the measured value.

The theoretical density matrix with  $\alpha = 1.56$  is also shown in figure 5.20 for comparison. In spite of the extra noise in the measured matrix, the two matrices are still quite similar.

The last thing to remark here, which is not shown, is that the measured density matrix is almost purely real, as was also expected from our choice of phase,  $\varphi_{\text{in}} = 0$ .

The rest of the reconstructed density matrices can be seen in figure 5.21; squeezed vacuum, bright amplitude-squeezed, bright phase-squeezed, and bright with intermediate squeezing angle. A lot could be said about the structure of these matrices, but we will limit the further discussion to the squeezed vacuum, which is the most interesting case from our perspective.

At a first glance at the squeezed vacuum density matrix, the most striking feature is the comparatively small odd matrix elements (that is, where  $m - n$  is odd). This is a sign of the state's Wigner function being symmetric in phase space;  $W(-q, -p) = W(q, p)$ . A quick look at the expression (5.8) for  $W_{mn}$  reveals that it is either symmetric or anti-symmetric:

$$W_{mn}(-q, -p) = (-1)^{m-n} W_{mn}(q, p). \quad (5.11)$$

Thus, the integration in (5.7) yields 0 for  $m - n$  odd. This is what we see in the reconstruction. That the odd matrix elements are not completely 0 must mean that the reconstructed Wigner function is not fully symmetric.

Apart from this information, there is not a lot of obvious information to be obtained from the off-diagonal elements, so instead we take a closer look at the diagonal elements - the photon number probabilities. Theoretically, (2.53), only even numbers of photons should have a non-zero probability, in accord with the pair-production process taking place in the parametric down-conversion. However, because of the non-unit detection efficiency, not all photons will be detected, and hence the ideal

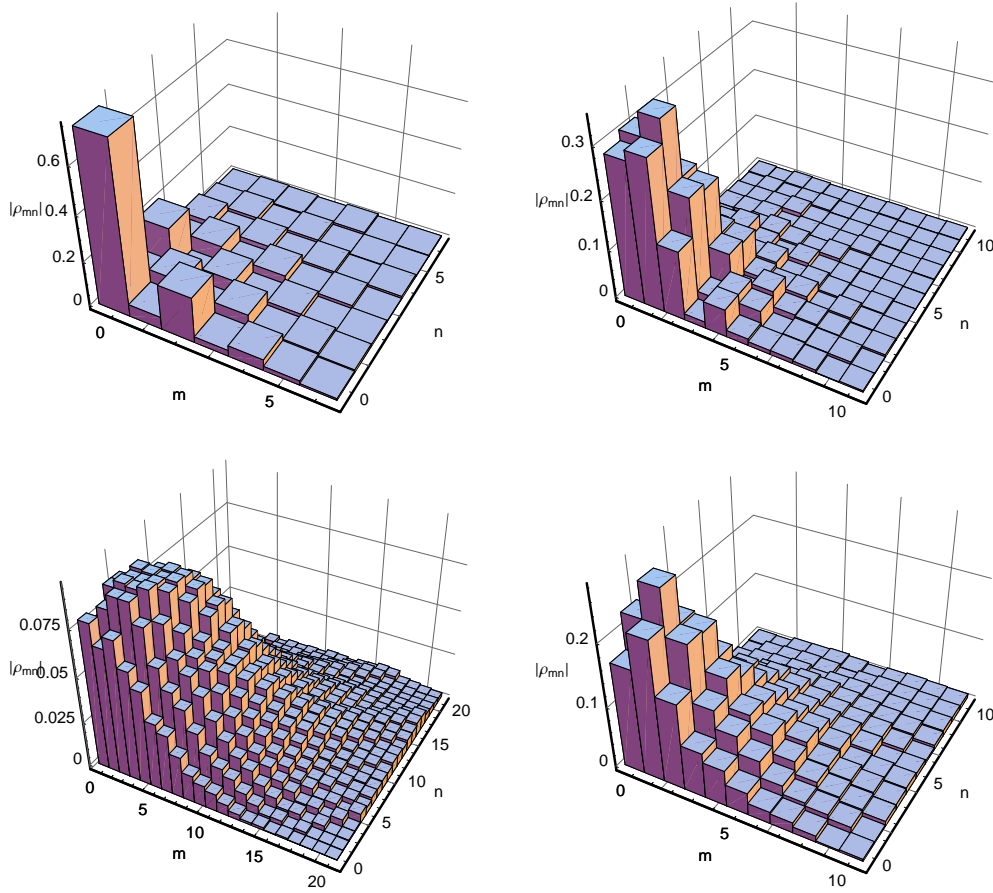


**Figure 5.21:** Reconstructed density matrices for the various squeezed states. *Top left:* squeezed vacuum, *top right:* bright amplitude squeezed, *bottom left:* bright phase squeezed, *bottom right:* bright state with squeezing angle intermediate between phase and amplitude.

pair-wise pattern will be smeared out. Simple probabilistic considerations [Leonhardt, 1997] gives the photon number probability as a function of detection efficiency:

$$p_n(\eta) = \sum_{m=n}^{\infty} \binom{m}{n} \eta^n (1-\eta)^{m-n} p_m(\eta=1), \quad (5.12)$$

where  $p_m(\eta=1)$  is the ideal probability (2.53).

In figure 5.22 the measured photon number probabilities are shown as the blue (left) bars. There are clearly no signs of the expected oscillation in the photon numbers, which is of course because of the poor detection efficiency  $\eta = 0.42$ . The red (middle left) bars of the figure shows the efficiency-corrected theoretically expected values using the same mean photon number as measured -  $\langle \hat{n} \rangle = 0.54$ . Before losses, the mean photon number is  $0.54/0.42 = 1.3$ , corresponding to a squeezing parameter (2.52) of  $r = \sinh^{-1}(\langle \hat{n} \rangle^{1/2}) = 0.97$ . This is in good agreement with the value  $r = 1.04$

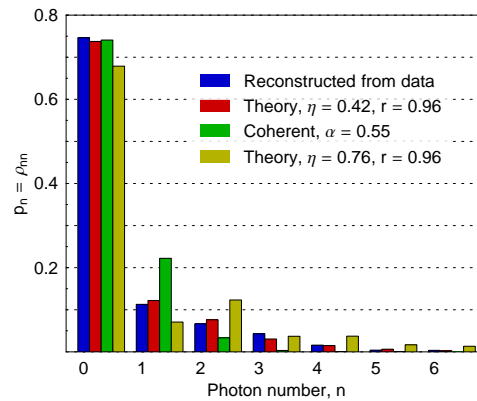


**Figure 5.22:** Squeezed vacuum reconstructed photon number probabilities (blue). Because of the poor detection efficiency, it is not possible to observe the expected alternating pattern. Had we had a better overall efficiency - something like  $\eta = 0.76$  - this pattern would have been apparent (yellow). Still, the statistics is clearly distinct from a coherent state with Poissonian distribution (green).

inferred from the  $-2$  dB/6 dB of figure 5.5.

To see that the state measured really *is* different from just a weak coherent state, the green (middle right) bars in figure 5.22 show the photon numbers for a coherent state which has the same vacuum contribution as our measured state. We see that the probability of one photon is only half as big for the measured state compared to the coherent, while the probability for two photons is twice as big. This at least gives an indication of the pair-wise nature of the state.

The yellow (right) bars in the figure shows the expected numbers for a detection efficiency of  $\eta = 0.76$ , which was the efficiency before the addition of the electronic noise. If we could regain this efficiency, we would clearly be able to see the alternating pattern of the photon number probabilities.



## Chapter 6

# Future plans

So far only one kind of non-classical light has been described in detail; single mode squeezed light. Vacuum states or weak coherent fields with decreased noise in one quadrature can have important applications in for example increased capacity of standard optical communications, better signal-to-noise ratio in spectroscopy, and, perhaps in particular, in interferometric measurements such as gravitational wave detection [Bachor and Ralph, 2004]. With respect to the line of research into light-atom interfaces pursued by the QUANTOP lab, however, the squeezed light production is mostly a prerequisite for more advanced nonclassical light sources, as already mentioned in the introduction.

We are currently well underway towards two distinctly different sources of non-classical light: EPR-entangled beams and single photons. The entangled light has already been produced with this experiment in Århus [Schori et al., 2002b, Schori, 2002], and it should be just a matter of time to get this back. The single photon source, on the other hand, is a completely new branch of the experiment, where the Ti:Sapph laser and the blue light generator will be reused while everything else is new. Common for all the different sources we are working on is their narrow bandwidth and frequency tunability, which make atomic transitions accessible for the light. This chapter describes the new developments of the experiment.

### 6.1 EPR entangled light beams

In section 3.2 we developed the theory for the output field of the degenerate OPO and saw that correlations between sidebands within a cavity bandwidth of the central frequency  $\omega_0$  causes a reduction of the vacuum noise in certain quadratures of the light field. It was also mentioned how in a nondegenerate OPO it is used that the photon pairs are down-converted into cavity modes symmetric around the central frequency. The formalism of the DOPO can be extended to the NDOPO in a very straight-forward way, but the final result is at the same time very similar and distinctly different: The individual modes will be extra noisy in both quadratures while a combined measurement of the quadratures of the two modes may show noise reduction. So now the quantum correlation is between two separate modes - they have become entangled. This phenomenon is also known as two-mode squeezing and was suggested in Reid and Drummond [1988] and Reid [1989]. Exactly the same state of two quadrature entangled vacuums can be generated by mixing two identical single-mode squeezed vacuums on a 50/50 beamsplitter [Braunstein and van Loock, 2004].

### 6.1.1 NDOPO output

The derivation of the NDOPO theory is completely parallel to the DOPO theory in section 3.2, so in the following we mainly reference the formulas there and just state the corresponding NDOPO results. We will make two simplifications (without loss of generality) for the sake of clarifying the notation: The pump phase is taken to be  $\varphi = 0$ , and when we get to the quadratures, only the position  $q = q_0$  and momentum  $p = q_{\pi/2}$  quadratures will be considered.

We start out with the NDOPO interaction Hamiltonian, which is slightly different from the DOPO:

$$\hat{H}_{\text{int}} = i\hbar g(\beta \hat{a}_s^\dagger \hat{a}_i^\dagger - \beta^* \hat{a}_s \hat{a}_i). \quad (6.1)$$

This Hamiltonian reflects the process of simultaneous generation (or absorption) of two photons, one in the signal ( $s$ ) and one in the idler mode ( $i$ ). In the experiment the two modes are very close in frequency - they are separated by 2 spectral ranges = 740 MHz - and we will assume that the cavity decay rates are equal for the two modes. A treatment with asymmetric losses is given in Schori et al. [2002b].

The equations of motion for the cavity modes are the same as for the DOPO, (3.18). In frequency space, corresponding to (3.21), the equations of motion become

$$-i\omega \tilde{a}_s(\omega) = g|\beta| \tilde{a}_i^\dagger(-\omega) - (\kappa_1 + \kappa_L) \tilde{a}_s(\omega) + \sqrt{2\kappa_1} \vec{a}_s(\omega) + \sqrt{2\kappa_L} \vec{b}_s(\omega), \quad (6.2)$$

where the arrows should indicate input fields. The equations for  $\tilde{a}_s^\dagger(-\omega)$ ,  $\tilde{a}_i(\omega)$ , and  $\tilde{a}_i^\dagger(-\omega)$  are completely analogous. Note that the frequency sidebands are now relative to the individual signal or idler frequencies:  $\tilde{a}_m(\pm\omega) \equiv \tilde{a}(\omega_m \pm \omega)$ , with  $m = s, i$ . We have two independent sets of coupled equations:  $\tilde{a}_s(\omega)$  is coupled to  $\tilde{a}_i^\dagger(-\omega)$  and  $\tilde{a}_s^\dagger(-\omega)$  is coupled to  $\tilde{a}_i(\omega)$ .

Proceeding to the output fields (cf. (3.24)), they become - letting them be symbolized by no tilde, hat, arrow or anything:

$$\begin{aligned} a_s(\omega) &= C_1(\omega) \tilde{a}_i^\dagger(-\omega) + C_2(\omega) \tilde{b}_i^\dagger(-\omega) + A_1(\omega) \vec{a}_s(\omega) + A_2(\omega) \vec{b}_s(\omega) \\ a_s^\dagger(-\omega) &= C_1(\omega) \tilde{a}_i(\omega) + C_2(\omega) \tilde{b}_i(\omega) + A_1(\omega) \vec{a}_s^\dagger(-\omega) + A_2(\omega) \vec{b}_s^\dagger(-\omega) \\ a_i(\omega) &= C_1(\omega) \tilde{a}_s^\dagger(-\omega) + C_2(\omega) \tilde{b}_s^\dagger(-\omega) + A_1(\omega) \vec{a}_i(\omega) + A_2(\omega) \vec{b}_i(\omega) \\ a_i^\dagger(-\omega) &= C_1(\omega) \tilde{a}_s(\omega) + C_2(\omega) \tilde{b}_s(\omega) + A_1(\omega) \vec{a}_i^\dagger(-\omega) + A_2(\omega) \vec{b}_i^\dagger(-\omega). \end{aligned} \quad (6.3)$$

The  $\omega$ -dependent prefactors have the following expressions:

$$\begin{aligned} C_1(\omega) &= \frac{2\kappa_1 g |\beta|}{(\kappa_1 + \kappa_L - i\omega)^2 - g^2 |\beta|^2} \\ C_2(\omega) &= \frac{2\sqrt{\kappa_1 \kappa_L} g |\beta|}{(\kappa_1 + \kappa_L - i\omega)^2 - g^2 |\beta|^2} \\ A_1(\omega) &= \frac{\kappa_1^2 - (\kappa_L - i\omega)^2 + g^2 |\beta|^2}{(\kappa_1 + \kappa_L - i\omega)^2 - g^2 |\beta|^2} \\ A_2(\omega) &= \frac{2\sqrt{\kappa_1 \kappa_L} (\kappa_1 + \kappa_L - i\omega)}{(\kappa_1 + \kappa_L - i\omega)^2 - g^2 |\beta|^2}. \end{aligned} \quad (6.4)$$

The two modes do not interfere with each other, so the commutation relation is

$$[\vec{a}_m(\omega), \vec{a}_n^\dagger(\omega')] = \delta(\omega - \omega') \delta_{mn}, \quad m, n = i, s. \quad (6.5)$$

For the input field covariances, we get that of all the possible combinations, only four become nonzero (coherent inputs):

$$\langle \vec{a}_s(\omega), \vec{a}_s^\dagger(\omega') \rangle = \delta(\omega - \omega'), \quad (6.6)$$

and the similar equation for  $\vec{b}_s$ ,  $\vec{a}_i$ , and  $\vec{b}_i$ . This gives the following output field covariances, which are no longer completely analogous to the DOPO case:

$$\begin{aligned} \langle a_s^\dagger(\omega), a_s(\omega') \rangle &= [C_1(-\omega)C_1(\omega') + C_2(-\omega)C_2(\omega')] \delta(\omega - \omega') \\ \langle a_s(\omega), a_s^\dagger(\omega') \rangle &= [A_1(\omega)A_1(-\omega') + A_2(\omega)A_2(-\omega')] \delta(\omega - \omega') \\ \langle a_s(\omega), a_s(\omega') \rangle &= 0 \\ \langle a_s^\dagger(\omega), a_s^\dagger(\omega') \rangle &= 0 \\ \langle a_s^\dagger(\omega), a_i(\omega') \rangle &= 0 \\ \langle a_s(\omega), a_i^\dagger(\omega') \rangle &= 0 \\ \langle a_s(\omega), a_i(\omega') \rangle &= [A_1(\omega)C_1(\omega') + A_2(\omega)C_2(\omega')] \delta(\omega + \omega') \\ \langle a_s^\dagger(\omega), a_i^\dagger(\omega') \rangle &= [C_1(-\omega)A_1(-\omega') + C_2(-\omega)A_2(-\omega')] \delta(\omega + \omega'). \end{aligned} \quad (6.7)$$

For the remaining 8 combinations, having the idler operators first, the results are the same.

### 6.1.2 Two-mode squeezing

Considering only the non-zero, normal ordered combinations, the spectral densities at the detection frequency  $\omega$  become, with the scaled parameters  $\eta_{\text{esc}}$ ,  $\epsilon$ ,  $\Omega$ :

$$\begin{aligned} \langle a_s^\dagger, a_s \rangle_\omega &= \frac{4\epsilon^2 \eta_{\text{esc}}}{[(1-\epsilon)^2 + \Omega^2][(1+\epsilon)^2 + \Omega^2]} \\ \langle a_s^\dagger, a_i^\dagger \rangle_\omega &= \langle a_s, a_i \rangle_\omega = \frac{2\epsilon(1+\epsilon^2 + \Omega^2)\eta_{\text{esc}}}{[(1-\epsilon)^2 + \Omega^2][(1+\epsilon)^2 + \Omega^2]}. \end{aligned} \quad (6.8)$$

The position quadrature fluctuation spectrum for a single mode is

$$\begin{aligned} \langle : \tilde{q}_s, \tilde{q}_s : \rangle_\omega &= \frac{1}{2} \langle : (a_s + a_s^\dagger), (a_s + a_s^\dagger) : \rangle_\omega \\ &= \frac{1}{2} (2 \langle a_s^\dagger, a_s \rangle_\omega) \\ &= \frac{4\epsilon^2 \eta_{\text{esc}}}{[(1-\epsilon)^2 + \Omega^2][(1+\epsilon)^2 + \Omega^2]}. \end{aligned} \quad (6.9)$$

For the momentum quadrature the result is exactly the same. This means that the individual modes have increased noise in both quadratures - actually, they are thermal states, see figure 2.2 [Braunstein and van Loock, 2004].

If we now instead look at the fluctuations in the difference or sum  $\tilde{q}_s \mp \tilde{q}_i$  between

the position quadratures of the two modes, we get

$$\begin{aligned}
\langle : (\tilde{q}_s \mp \tilde{q}_i), (\tilde{q}_s \mp \tilde{q}_i) : \rangle_\omega &= \frac{1}{2} \langle : (a_s + a_s^\dagger \mp a_i \mp a_i^\dagger), (a_s + a_s^\dagger \mp a_i \mp a_i^\dagger) : \rangle_\omega \\
&= \langle a_s^\dagger, a_s \rangle_\omega + \langle a_i^\dagger, a_i \rangle_\omega \mp \langle a_s, a_i \rangle_\omega \mp \langle a_s^\dagger, a_i^\dagger \rangle_\omega \\
&= \frac{8\epsilon^2 \eta_{\text{esc}} \mp 4\epsilon(1 + \Omega^2 + \epsilon^2) \eta_{\text{esc}}}{[(1 - \epsilon)^2 + \Omega^2][(1 + \epsilon)^2 + \Omega^2]} \\
&= \mp 2\eta_{\text{esc}} \frac{2\epsilon}{(1 \pm \epsilon)^2 + \Omega^2}.
\end{aligned} \tag{6.10}$$

This corresponds to the results for the single-mode squeezing spectra (3.43) and (3.44) except for a factor of two: The noise of the sum or difference of two independent variables is the sum of their noises, so for the combined quadratures the SQL is 1 - twice as big as for the individual quadratures, and the variance/power spectrum of the difference and sum is

$$\begin{aligned}
\chi(\tilde{q}_s \mp \tilde{q}_i) &= 1 + \langle : (\tilde{q}_s \mp \tilde{q}_i), (\tilde{q}_s \mp \tilde{q}_i) : \rangle_\omega \\
&= 1 \mp 2\eta_{\text{esc}} \frac{2\epsilon}{(1 \pm \epsilon)^2 + \Omega^2}.
\end{aligned} \tag{6.11}$$

What we see here is that the difference between the position quadratures of the two modes is squeezed below the SQL, while the sum is anti-squeezed. The conjugate variable of  $\tilde{q}_s - \tilde{q}_i$  is the momentum difference  $\tilde{p}_s - \tilde{p}_i$ , so this should have increased noise to satisfy the uncertainty principle. And this is indeed so: For the momentum quadrature, the signs have just been changed - anti-squeezing in the difference and squeezing in the sum. Only simultaneous measurement of the quadratures of the two modes will reveal this phase-sensitive variation of the noise. The individual modes are equally (and increased) noisy in all quadratures.

### 6.1.3 Entanglement

The so prepared *two-mode squeezed vacuum* state is the archetype of a continuous variable entangled state. This state is analogous to the state introduced in the very famous EPR paper [Einstein et al., 1935], which concerned two particles with perfect correlation in the relative position and the total momentum. The EPR state is however unphysical, since it has infinite uncertainty in the position sum and momentum difference [Bachor and Ralph, 2004]. The two-mode squeezed state is a physical realization of the EPR state, with the  $q$  and  $p$  quadratures playing the role of the particle position and momentum. The Wigner function of the two-mode squeezed vacuum is

$$\begin{aligned}
W(q_s, p_s, q_i, p_i) &= \\
&= \frac{1}{\pi^2} \exp \left\{ -\frac{e^{-2r}}{2} [(q_s + q_i)^2 + (p_s - p_i)^2] - \frac{e^{2r}}{2} [(q_s - q_i)^2 + (p_s + p_i)^2] \right\}, \tag{6.12}
\end{aligned}$$

which approaches the original EPR state  $C\delta(q_s - q_i)\delta(p_s + p_i)$  in the limit of  $r \rightarrow \infty$  [Braunstein and van Loock, 2004].

Entanglement of the two modes means that they are inseparable, that is, the total density operator *cannot* be written as a sum of product states [Werner, 1989]:

$$\hat{\rho}^{(total)} = \sum_k p_k \hat{\rho}_k^{(s)} \otimes \hat{\rho}_k^{(i)}. \tag{6.13}$$

Since it is not easy to check the separability of the density operators, many other conditions for inseparability exist. For the system at hand, a useful criterium is the one by Duan et al. [2000b], which (in a simplified form) states that a state is inseparable if

$$\langle(\Delta(\tilde{q}_s - \tilde{q}_i))^2\rangle + \langle(\Delta(\tilde{p}_s + \tilde{p}_i))^2\rangle < 2. \quad (6.14)$$

This criterium is fulfilled for our two-mode squeezed state as soon as we have some squeezing,  $\epsilon > 0$ . A measurement of the sum of the variances in (6.14) can serve to quantify the amount of entanglement achieved. Had the two modes been coherent vacuums, the state would have been separable, and the sum of variances would be at the SQL = 2. For the original EPR state, the sum is 0, which is maximum entanglement.

The paradox in the EPR paper consists of the fact that a measurement of the position of one particle immediately will give full information of the position of the other particle. If, on the other hand, the momentum of the first particle is observed, the momentum of the other particle is immediately known with certainty. Since the uncertainty principle prohibits the position and momentum of the second particle to be exactly determined simultaneously, this collapse of the wavefunction of the second particle must originate in the observation of the first particle, even though the particles could be widely separated. This was Einstein's "spooky action at a distance". Since our two-mode squeezed state is not maximally entangled, we cannot get exact information about one mode from measurement on the other. We can, however, get increased knowledge about it (reduced uncertainty). In Reid [1989] the conditional variance of  $q_s$  inferred from a measurement of  $q_i$  is shown to be

$$\langle(\Delta\tilde{q}_s)^2\rangle_i = \langle(\Delta\tilde{q}_s)^2\rangle - \frac{\langle\tilde{q}_s, \tilde{q}_i\rangle^2}{\langle(\Delta\tilde{q}_i)^2\rangle}, \quad (6.15)$$

and similarly for the variance  $\langle(\Delta\tilde{p}_s)^2\rangle_i$  of the signal momentum conditioned on the measurement of the idler momentum. The product of these conditional variances gets below the Heisenberg limit of 1/4 for any amount of squeezing, but this is not a violation of the uncertainty principle; we cannot measure both position and momentum of the idler mode simultaneously in the first place, so it is not possible to infer both position and momentum of the signal either. If, on the other hand, we believe in local realism, that is, no action at a distance, and the signal and idler mode are spatially separated, then the signal quadratures must initially be determined within these variances, and that would violate the uncertainty principle. A number of different experiments (most notably the ones by Freedman and Clauser [1972] and Aspect et al. [1982]) have been performed to test the validity of quantum mechanics based on the Bell inequalities [Bell, 1987], and although not being fully conclusive, there is striking evidence that the non-locality of quantum mechanics holds true.

These were some words on the fundamental physical aspects of entanglement, which is one of the most peculiar and characteristic features of quantum mechanics. Our primary interest in this phenomenon, however, is the applications in the field of quantum information, where entanglement plays a very central role. It is a vital ingredient in almost all quantum information machinery imaginable: Quantum computers, quantum cryptography, quantum memory, quantum teleportation, dense coding, ... The sources used for producing entangled states in the early (1970's, 1980's) tests of quantum mechanics would not have been appropriate for all these

demanding quantum information applications. Beginning in the 1990's a number of different "entangled state generators" were developed, and they become ever more useful.

The experiment by Ou et al. [1992] was probably the first demonstration of a practically applicable entangled state, while at the same time it was also the first to demonstrate the EPR paradox in the original continuous variable (cv) setting. This experiment was very similar to ours, producing a two-mode squeezed state from an OPO. The only major difference was their use of type II phase matching, thus producing polarization nondegenerate beams where our two modes are nondegenerate in frequency. In spite of this early cv source, the discrete variable (dv) entangled states were for a long time dominant in the picture, especially because of the relatively easy generation of polarization correlated photon pairs through single-pass spontaneous down-conversion, as in Kwiat et al. [1995]. Such entangled photon pairs have spawned remarkable results, maybe most notably the first ever demonstration of quantum teleportation by Bouwmeester et al. [1997]. An important extension to the family of entangled states came when Bouwmeester et al. [1999] managed to prepare a so-called *GHZ* or *tripartite* entangled state, where three photons became correlated. In the cv regime, quantum teleportation was carried out by Furusawa et al. [1998] with an EPR-state prepared by the mixing of two squeezed vacuum states. By combining three squeezed vacuum states, Aoki et al. [2003] prepared a cv GHZ state and recently used this to set up a teleportation scheme between three parties [Yonezawa et al., 2004]. Another noticeable development was that by Bowen et al. [2002], obtaining cv polarization entanglement in the Stokes operators of the light field<sup>1</sup> instead of the usual quadrature entanglement.

So far only entangled states of light have been mentioned, but also entanglement of massive particles has been achieved. Of the most noteworthy experiments are the entanglement between two atoms in a high-Q microwave cavity by Hagley et al. [1997] and the deterministic entanglement of two trapped ions by Turchette et al. [1998]. Last, but not least, the neighbouring experiment in our lab was the first to generate entanglement between macroscopic objects - two ensembles of  $10^{12}$  cesium gas atoms became entangled during a period of 0.5 ms [Julsgaard et al., 2001].

An extensive summary of - in particular - cv entanglement theory and experiments and applications to quantum information is given in the excellent review article by Braunstein and van Loock [2004].

After this small historical detour, we will now return to the experiment and briefly describe the alterations to the setup necessary for the generation of the entangled beams.

#### 6.1.4 Experimental setup

Almost all of the setup of the squeezed light experiment is reused, with some important additions. See figure 6.1. The OPO, when resonant on  $\omega_0$ , is already producing down-converted light into all longitudinal cavity modes within the phase matching bandwidth. In the homodyne detection only the part of the light field with frequency equal to the local oscillator frequency is detected. As our signal and idler modes we

<sup>1</sup>The Stokes operators describe the polarization state of the light:  $\hat{S}_x$  is the difference between vertical and horizontal polarization,  $\hat{S}_y$  between  $+45^\circ$  and  $-45^\circ$  polarization, and  $\hat{S}_z$  between right- and left-circular polarization.

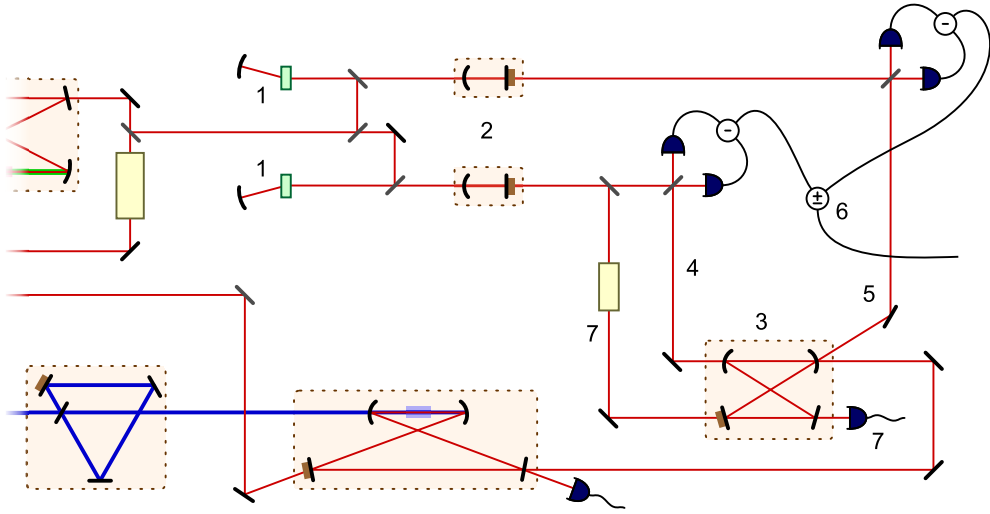


**Figure 6.1:** The setup for producing and characterizing EPR-entangled beams. **1)** A part of the main laser beam is split off before the 20 MHz EOM and is further split in two. One part is shifted in frequency by +370 MHz, the other part by -370 MHz, by passing them through an AOM in double-pass. **2)** The frequency shifted beams are cleaned and stabilized in mode cleaning Fabry-Perot cavities. They are used as local oscillators in either homodyne arrangement. For this their phases can be scanned by piezo-mounted mirrors, which are not shown here. **3)** The output from the OPO is directed into an empty bow-tie cavity acting as a frequency filter. The cavity is kept on resonance with the signal frequency ( $\nu_0 + 370$  MHz), while the idler frequency ( $\nu_0 - 370$  MHz) is completely off-resonant. Thus, **4)** the signal part of the output is transmitted and **5)** most of the remaining OPO output is reflected, including the idler. **6)** The quadratures of the two modes are detected in individual homodyners, and the currents from the two detections are summed or subtracted (possibly with a scaling factor on one of the currents) to reveal the quadrature correlations between the two modes. **7)** To lock the filter cavity on the signal frequency, part of the up-shifted local oscillator is split off to introduce a counter-propagating locking beam, which is modulated at a frequency far from the 20 MHz used for the OPO locking, since this beam also gets into the OPO where it should not cause instabilities in the lock. For any practical applications of the entangled beams, they will of course propagate through some physical interesting objects (like atoms, for instance) before being detected. This particular setup is only for characterizing the entanglement.

will use the cavity modes separated by one free spectral range  $\nu_{\text{FSR}} = 370$  MHz at either side of the central frequency:  $\omega_s = \omega_0 + 2\pi\nu_{\text{FSR}}$ ,  $\omega_i = \omega_0 - 2\pi\nu_{\text{FSR}}$ . For the characterization of the entanglement we want to measure the quadratures of each of the two modes individually, and therefore two homodyne setups are needed with local oscillators at  $\omega_s$  and  $\omega_i$ , respectively. To produce those frequencies, two small parts are separated from the main laser beam. Each of the beams has its frequency shifted by double-passing a 185 MHz acousto optical modulator and subsequently they are passed through a mode cleaning cavity similar to the one used for the local oscillator in the degenerate case.

In the output of the OPO the signal and idler occupy the same spatial mode and thus need to be separated. In most experiments of this kind the two modes are fre-

quency degenerate but polarization nondegenerate - as already mentioned this was the case in Ou et al. [1992]. When this is the case, the modes can easily be separated on a polarizing beamsplitter. It is not quite as easy to split two modes based on different but close-lying frequencies. In our experiment a filter cavity actively locked to resonate at the signal frequency is employed. The bow-tie cavity has a bandwidth of 38 MHz - wider than the OPO, to transmit the full OPO spectrum - and a free spectral range of 1.5 GHz - exactly twice the splitting between signal and idler. Thus, when the cavity is resonant on the signal mode, this gets completely transmitted (equal in/out coupling transmissions), while the idler mode, being in between two resonances gets completely reflected, along with most of the other (uninteresting) output modes from the OPO.

This way the signal and idler will be spatially separated. Should it be necessary to get a "pure" idler mode, without contamination from all the other modes, a similar filter cavity could be build to resonate and transmit the idler frequency. As long as we just characterize the fields in homodyne detection this is not needed. To measure the correlations between the two modes, the individual difference photocurrents from the two homodyne setups, probing the individual field quadratures, will be subtracted or added and monitored on a spectrum analyzer. Scanning the local oscillator phases can then provide different combinations of the measured quadratures of the two modes, which should reveal the expected reduction or increase of the total noise. This was done by Schori et al. [2002b] who measured a degree of entanglement (noise reduction below the SQL) of -4.3 dB (corrected for electronic noise). As expected from (3.44) and (6.11) this is basically the same result as the -4.5 dB observed in single-mode squeezing.

## 6.2 Single photons

In the quantum description of light, the photon is the most fundamental entity, acting either as a particle or as a wavepacket with a certain spatial extent (wave-particle duality). It is highly non-classical, with a non-Gaussian distribution in phase space, and with negative regions of the Wigner function. Our main motivation for developing a source of single photons is to investigate whether the atomic quantum memories being developed elsewhere in the QUANTOP lab are feasible for storing the quantum state of a single photon.

This section gives a detailed account of the plans for this source.

### 6.2.1 Requirements

For a machine producing single photons capable of interacting with atomic systems we have certain wishes and demands.

The most obvious requirement is for the photon to have the **correct wavelength** corresponding to the atomic transitions in use. In our case, the relevant transitions are the 852 nm  $6S_{1/2} \rightarrow 6P_{3/2}$  transition of cesium which is used in the atomic clock and the room temperature gas cell experiments and the 795 nm  $5S_{1/2} \rightarrow 5P_{1/2}$  transition of rubidium used in the BEC experiment. Besides the coarse wavelength selection, a precise **tunability** is also necessary to hit the exact frequencies needed for the atomic interactions. The light-atom interaction schemes used in the QUANTOP lab employ off-resonant coupling, that is, the light is detuned from the atomic transition, hence to a good approximation suppressing absorption and leaving only dispersive effects.

The detunings are on the order of a few hundreds of MHz. To avoid absorption of the light, it should be **narrowband**, that is, the bandwidth should be considerably smaller than this detuning.

Furthermore, the photon must be **short** and **localized**: The photon should be spatially and temporally confined - we need to know where and when the photon appears! In a quantum memory experiment, for instance, several processes take place consecutively, so it is necessary to know when the photon has arrived. Certain light-atom interface proposals [Hammerer et al., 2004] employ multiple passes of the light through the atomic medium. To avoid the photon "biting its own tail" within the atoms, it should have a small longitudinal extent, so that it can be fully contained on the optical table outside the atoms between the passes. This requirement is in contrast to the demand of narrow bandwidth since for a Fourier limited pulse, the temporal width is inversely proportional to the spectral width. Thus it may be necessary to compromise between those two wishes. The requirement of localization also goes for the transverse directions: If we just wish to do intensity measurements (photon counting), the transverse spatial mode is not so important. If we, however, want to do field measurements (homodyning), a **good transverse spatial mode** ( $TEM_{0,0}$ ) is essential, since a poor mode matching to the local oscillator effectively couples in vacuum, decreasing the efficiency (as in section 4.4.2). Apart from the good spatial mode matching, the homodyning of pulses (as opposed to cw beams) also requires the temporal overlap to be very good. This forces us to chop the local oscillator beam into pulses of the same shape as the photon wavepacket. We actually expect this to be one of the most demanding parts of the experiment.

A very important goal is to reach as **high efficiency** as possible, that is, when we believe we have a photon, there *should* also be one. If the probability of having a photon is only  $\eta$ , the measured state will have a proportion  $1 - \eta$  of vacuum mixed into the state, and of course we want to be as close to the single photon Fock state as possible. For the same reason, the probability of getting more than one photon should be negligible. Another property which may conflict with this last point but is less important (although preferable) is a **high production rate**. This will allow for faster data acquisition which is not only a convenience, but may also be necessary to obtain enough data to allow for good statistics. A homodyne measurement is in principle just one big interferometer, and as such is very sensitive to tiny vibrations somewhere along the beam paths. We can therefore not expect phase stability for a long time, and so fast data taking becomes important.

Single photon sources are loosely grouped in three classes: *Spontaneous* or random sources, which have low production rates, and where the single photons arrive at random. There is no knowledge about when the photons arrive, so experiments employing this kind of source use postselection based on coincidence measurements to identify successful events. A typical example is just a strongly attenuated laser beam with mean photon number close to zero. In *heralded* sources, the photons also arrive at random (probabilistically), but here knowledge about their production can prepare other parts of the experiment for the photon's arrival. Finally, *on-demand* sources (or push-button sources or single photon guns) are very desirable - it would be optimal to produce a photon deterministically at a given time and position just by the push of a button. This is a very non-trivial task, but there is rapid progress going on with for example quantum dots [Santori et al., 2002] and single atoms in high-Q cavities [Kuhn et al., 2002]. Our source will only be of the heralded kind, but this is probably the only major disadvantage it will have compared to other sources, while it will be superior on most other specifications.

### 6.2.2 Implementation: NDOPO far below threshold

As will be discussed in this and the following section, almost all of our requirements for the single photon source can be met by a nondegenerate type I phase matched OPO operating far below threshold. This is very fortunate since we now have a great deal of experience with this kind of device. By operating the OPO very far below threshold (low pump powers), the stimulated emission of signal and idler photons is negligible, meaning that there is a low probability of more than one photon pair to be generated at a time. To our knowledge, the only work done previously in this direction was that by Lu and Ou [2000] who measured the correlations between photons created pairwise in a *degenerate* type I OPO far below threshold, but apparently without ever separating the photon pairs so as to prepare single photon states.<sup>2</sup> By using frequency nondegenerate down-conversion, we can separate the signal and idler photons in much the same way as with the EPR beams. A localized single photon can then be prepared in the signal path by detecting an idler photon - the idler acts as a trigger that announces when we can expect the signal photon to arrive.

Thus it appears that our development should end up in a novel source of single photons, which will have a range of very advantageous properties. In the following, the properties of the NDOPO far below threshold is considered. In the next section, a detailed account of the various design considerations will be given. Most of the experiment is still on the drawing board, so in the end it might be different from what is described here. Also, different schemes for the implementation with atoms could require certain changes.

A fairly detailed theory of the OPO far below threshold is given in Lu and Ou [2000], which is based on the general OPO theory of Collett and Gardiner [1984] - the same as in this thesis. We can completely reuse the formulas from the NDOPO sections 6.1.1 and 6.1.2, with the added assumption of "far below threshold", meaning  $\epsilon = g|\beta|/(\kappa_1 + \kappa_L) \ll 1$ . From (6.8) we have the spectra of the signal and idler output fields, dropping the  $\epsilon$  terms from the denominator:

$$S_{s,i}(\omega) \equiv \langle a_{s,i}^\dagger a_{s,i} \rangle_\omega = \frac{4\epsilon^2 \eta_{\text{esc}}}{(1 + \Omega^2)^2}, \quad (6.16)$$

of course centered around the individual signal or idler frequencies  $\omega_s, \omega_i$ . This will be the spectrum of the generated photons. It is a squared Lorentzian with a FWHM of  $\Delta\Omega = 2\sqrt{\sqrt{2} - 1} = 2 \cdot 0.64$  - in regular frequency units the photon bandwidth is then

$$\Delta\nu_{\text{ph}} = \frac{\Delta\Omega(\kappa_1 + \kappa_L)}{2\pi} = 0.64\Delta\nu_{\text{cav}}, \quad (6.17)$$

which is a little narrower than the bandwidth of the cavity. The spectrum signifies the photon flux per Hz bandwidth, so the total photon flux (production rate) of either signal or idler out of the OPO is

$$\begin{aligned} R_{\text{out}} &= \int_{-\infty}^{\infty} \frac{d\omega}{2\pi} S(\omega) = \int_{-\infty}^{\infty} \frac{d\omega}{2\pi} \frac{4\epsilon^2 \eta_{\text{esc}}}{\left(1 + \left(\frac{\omega}{\kappa_1 + \kappa_L}\right)^2\right)^2} \\ &= \epsilon^2 \eta_{\text{esc}} (\kappa_1 + \kappa_L) = \epsilon^2 \kappa_1. \end{aligned} \quad (6.18)$$

<sup>2</sup>It seems like also the group of H. Weinfurter looked briefly into this topic, but they have no publications on it - it is mentioned in the thesis of Oberparleiter [2002].

Using the expression (4.2) for the threshold power, the rate can be expressed in terms of more experimental parameters:

$$R_{\text{out}} = \frac{P_p}{P_{th}} \frac{T_1 \nu_{\text{FSR}}}{2} = 2E_{\text{NL}} P_p \frac{T_1}{(T_1 + \mathcal{L})^2} \nu_{\text{FSR}} . \quad (6.19)$$

The signal photon, which will be our single photon state, is prepared by detecting the idler photon, called the trigger photon from now on. The temporal mode of the signal photon is centered around the detection time of the trigger photon, with an extent given by the intensity cross-correlation function  $\Gamma_{s,i}^{(2,2)}(\tau) = \langle \hat{a}_i^\dagger(t) \hat{a}_s^\dagger(t+\tau) \hat{a}_s(t+\tau) \hat{a}_i(t) \rangle$  between the two fields. In Lu and Ou [2000] it is calculated to be

$$\Gamma_{s,i}^{(2,2)}(\tau) = \epsilon^2 \kappa_1^2 e^{-2(\kappa_1 + \kappa_L)|\tau|} , \quad (6.20)$$

that is, the photon wavepacket has the shape of a double-sided decaying exponential with a  $1/e$  temporal width of

$$\Delta\tau_{\text{ph}} = \frac{1}{\kappa_1 + \kappa_L} = \frac{1}{\pi\Delta\nu_{\text{cav}}} \approx \frac{1}{5\Delta\nu_{\text{ph}}} . \quad (6.21)$$

When we think of the length of the photon, we think of the “full” length, not the  $1/e$  width. A better measure is one inverse cavity bandwidth, because there is a 96% probability of the photon being detected within this range. Let us denote this definition of the temporal/spatial photon length by  $\Lambda_{\text{ph}}^\tau / \Lambda_{\text{ph}}$ :

$$\Lambda_{\text{ph}}^\tau = \pi\Delta\tau_{\text{ph}} = \Delta\nu_{\text{cav}}^{-1} , \quad \Lambda_{\text{ph}} = c\Lambda_{\text{ph}}^\tau = c/\Delta\nu_{\text{cav}} . \quad (6.22)$$

Integration of the correlation function gives the total production rate of the prepared single photons:

$$R_{\text{sp}} = \int_{-\infty}^{\infty} \Gamma_{s,i}^{(2,2)}(\tau) d\tau = \frac{\epsilon^2 \kappa_1^2}{\kappa_1 + \kappa_L} = \epsilon^2 \kappa_1 \eta_{\text{esc}} = R_{\text{out}} \eta_{\text{esc}} . \quad (6.23)$$

A signal photon is only prepared when a trigger photon is detected, and only a proportion  $\eta_{\text{esc}}$  of the produced trigger photons escape from the cavity - therefore the number of prepared photons is reduced compared to the total rate. Actually, because of inefficient single photon counters, this rate should be further reduced by the detector quantum efficiency as well as the propagation efficiency from OPO to trigger photon counter:

$$R_{\text{sp}} = R_{\text{out}} \eta_{\text{esc}} \eta_{\text{qe}}^t \eta_{\text{prop}}^t . \quad (6.24)$$

We can, obviously, not be sure of having a signal photon every time the trigger detector fires; there will be a number of inefficiencies in the setup which will cause loss of the signal photon such that the actual state is a mixture of single photons and vacuum. The escape efficiency from the OPO is just one of those sources of loss. Others will be mentioned in the next section.

The down-conversion with weak pumping is a Poissonian process, so for a given production rate  $R_{\text{sp}}$ , the probability of having  $N$  photons within a time interval  $t$  is

$$P(N) = \frac{e^{-R_{\text{sp}}t} (R_{\text{sp}}t)^N}{N!} . \quad (6.25)$$

There is a certain risk of having more than one photon within the given time interval. The probability of more than one photon, conditioned on having *at least* one is

$$P(N \geq 2 | N \geq 1) = \frac{P(N \geq 2)}{P(N \geq 1)} = \frac{1 - P(0) - P(1)}{1 - P(0)} = 1 - \frac{R_{\text{sp}} t}{e^{R_{\text{sp}} t} - 1}. \quad (6.26)$$

The time interval in question is usually the integration time of the signal detector. To guarantee as pure a state as possible, this number should be minimized.

### 6.2.3 Planned setup

**Benchmarks.** So, what do we want to achieve? We want a NDOPO single photon source where the two most important parameters are; 1 - the photon length and bandwidth - not spectrally wider than at most  $\sim 100$  MHz, but at the same time with a spatial extent of not more than a few meters, to make it fit on a table. 2 - a high efficiency (photon-to-vacuum ratio) to be able to clearly distinguish the nonclassical features of the single photon state. Assuming a negligible number of detections with two or more photons, the initial signal state after detection of a trigger photon is  $|\psi_s\rangle_{\text{initial}} = |1\rangle$ . If only a ratio  $\eta$  of the signal photons are detected, the measured state is  $|\psi_s\rangle_{\text{measured}} = (1 - \eta)|0\rangle + \eta|1\rangle$ . If the total efficiency  $\eta$  gets below 50%, the single photon state has been admixed so much with the vacuum, that the negativity of the Wigner function disappears [Leonhardt, 1997]. The higher efficiency we can attain, the closer is the measured state to the initial single photon state.

Regarding the wavelength, we start out by running at the 852-860 nm range, so that we can reuse as much of the current setup as possible and run the squeezing/EPR experiment in parallel - and, not to forget, staying with the cesium wavelength at 852 nm. Sticking to this colour, we also decided to keep using potassium niobate as the nonlinear medium. An alternative would be to have a periodically poled crystal fabricated, but we believe that the bulk losses might be a little too high for our purpose. However, it will definitely be an option in the future, especially if we wish to move on to the rubidium wavelengths.

**Reaching the benchmarks - OPO design.** Clearly, it would be convenient if we could use the already existing OPO for this project as well. However, it soon turns out that it is not very well suited for producing short photons - it is too long itself! In its current state it has a bandwidth of around 8 MHz, corresponding to a photon length of  $\Lambda_{\text{ph}} \approx 40$  m. Changing the output coupler to have a very high transmission of  $T_1 = 50\%$  would give a photon of 10 m - still quite long. Another problem with the current cavity is its passive stability which is not good enough. See the discussion on that below.

It appears that we could benefit from designing a brand new OPO. How short should it be then, and what finesse should it have? We have found that a photon length of 3 m ( $\sim 64$  MHz bandwidth) is a good compromise in many ways. This requires a cavity bandwidth of  $\Delta\nu_{\text{cav}} = c/\Lambda_{\text{ph}} = 100$  MHz. In terms of cavity length, output coupler transmission and cavity losses, the cavity bandwidth is given by

$$\Delta\nu_{\text{cav}} = \frac{\nu_{\text{FSR}}}{\mathcal{F}} = \frac{c}{l_{\text{cav}}} \frac{T_1 + \mathcal{L}}{2\pi}, \quad (6.27)$$

and inserting for example  $T_1 = 0.20$ ,  $\mathcal{L} = 0.01^3$ ,  $l_{\text{cav}} = 0.10$  m gives exactly  $\Delta\nu_{\text{cav}} =$

<sup>3</sup>The pump power will be very low, so BLIIRA losses are low as well.

100 MHz. The escape efficiency, which should be as close to unity as possible, becomes with these parameters

$$\eta_{\text{esc}} = \frac{T_1}{T_1 + \mathcal{L}} = 0.95, \quad (6.28)$$

which is fairly high, but could be better. Taking instead  $T_1 = 0.30$  and  $l_{\text{cav}} = 0.15$  m would give the same bandwidth but with a better escape efficiency of  $\eta_{\text{esc}} = 0.97$ .

For cavity lengths of this magnitude, a traveling wave ring cavity is not really feasible, so instead we look towards a standing wave design. The physical length should then be half of the values just calculated, and further corrected for the increased optical path length in the crystal. We have carried out a detailed analysis of various cavity geometries<sup>4</sup> and found that a suitable design is a semi-monolithic cavity with a curved output coupler and the 1 cm long crystal coated to be highly reflecting for the infrared wavelength at one end surface and transmitting at the other. Both surfaces should have high transmission for blue. We have not yet settled conclusively on the final design of the OPO, as its properties may have to depend on the performance of other parts of the experiment - in particular the local oscillator shaper.

**Cavity stability, locking.** The locking of a single photon producing linear cavity is a bit more tricky than the locking of the squeezing bow-tie cavity. We cannot afford to inject any locking beam while measuring since this would definitely ruin the single photon state. An alternative, used for instance by Lu and Ou [2000] would be to alternate single photon production and measurement by locking beam injection via a mechanical beam chopper. We believe, however, that it should be possible to build a cavity which is passively stable on resonance for longer periods of time (at least several seconds), especially because the cavity linewidth is quite broad. This will require a very temperature stable oven for the crystal, and probably also a good sealing from the environment to avoid air flows and acoustic vibrations. It has been discussed to put the cavity into a low vacuum chamber, which would have the added benefit of reducing condensation on the crystal surface when operating it at the 4-5°C required for 852 nm. These topics still require further consideration.

A sketch of the full setup plan is shown in figure 6.2. Even though the OPO design is the most delicate part of the planning, attention to the other elements is required as well.

**Filter cavity.** As in the EPR experiment, we look at the symmetrical longitudinal cavity modes closest to the center frequency. To split the trigger photon (either  $\omega_0 + \omega_{\text{FSR}}$  or  $\omega_0 - \omega_{\text{FSR}}$ ) from the rest of the OPO modes, we will also use the same idea: A filter cavity resonant on the trigger frequency transmits the trigger photons and reflects all non-resonant modes. Since the phase matching bandwidth is very broad ( $\sim 20$  nm) there will certainly be some modes further away from the center frequency that are resonant in the filter cavity. Thus, an interference filter with a bandwidth of  $\sim 0.3$  nm is placed right in front of the trigger photon detector to get rid of what might be left of modes from the OPO, while at the same time efficiently taking care of any blue light from the pump. Figure 6.3 shows how these two filters can suppress all other modes than the filter mode.

<sup>4</sup>There is no room in this outlook for these calculations. We employ the ABCD-formalism to find the cavity stability criteria and beam size within the crystal, which has a further implication on the effective nonlinearity, calculated from the Boyd-Kleinman theory.

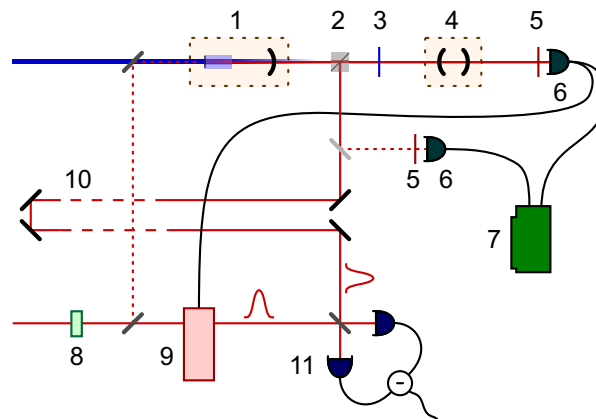


**Figure 6.2:** Setup plan for the single photon experiment. **1)** The OPO will be constructed as a semi-monolithic linear cavity, about 5 cm long. The  $\text{KNbO}_3$  crystal is highly reflecting for the down-converted wavelength on the outer end surface and highly transmitting on the inner end surface. **2,3,4)** To split the trigger photon from the rest of the modes, a small Fabry-Perot cavity resonant on the trigger frequency acts as a filter, transmitting the trigger and reflecting the rest. A quarter-wave plate and a polarizing beamsplitter directs the back-reflected light away from the OPO. **5)** To eliminate any remaining modes that might be transmitted through the filter cavity and to get rid of any stray light, a 0.3 nm interference filter is placed in front of the single photon detectors, **6)**, which are avalanche photo diodes with  $\sim 45\%$  quantum efficiency. **7)** For measuring coincidences between trigger and signal photons, the measured photodetection events are collected on a time-correlation computer board. **8)** An AOM is used to shift a part of the main laser beam in frequency to match the non-degenerate down-converted fields of the OPO, separated by one free spectral range from the center frequency. **9)** To make the temporal mode of the local oscillator simulate that of the single photon, a Pockels cell pulse shaper is inserted in the beam. **10)** The prepared single photon has to be delayed until the local oscillator pulse is ready. This is done by a  $\sim 15$  m long optical delay line across the table. **11)** Finally, single photon and local oscillator are mixed and detected in a dc homodyne system and the photocurrent is sampled on the computer.

The filter cavity will be quite short, linear, and with two curved mirrors. The non-resonant light reflected off of it will propagate back in the same direction as where it came from. A combination of a polarizing beamsplitter and a quarter-wave plate is employed to direct it away from the OPO. This reflected light then contains most of the down-converted modes, including the signal. When the signal is measured by homodyning, it is not necessary to separate it from the other modes. For coincidence measurements, though, where the signal is detected on a single photon detector, it should be separated. It may be necessary with a filter cavity as well, but we will first try to use just the interference filter. This way photons from some of the other modes will be detected as well, but since they are not correlated with the trigger photon, they will just form a flat background level on top of which the double-exponential signal should be visible.

The line-shape of the trigger photon filter cavity will be even wider than the OPO, and it should also be possible to make it passively stable between locking sessions. Another idea is to make a digital locking loop by observing the count rate from the

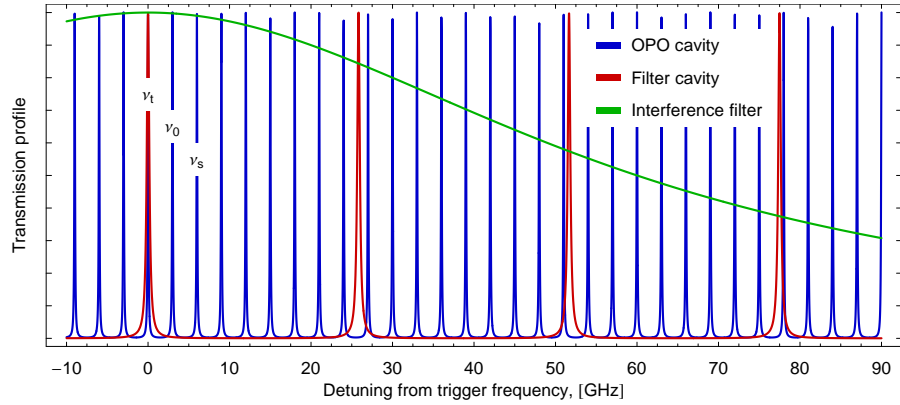


**Figure 6.3:** An example of a possible OPO/filter configuration. The OPO is taken to have a bandwidth  $\Delta\nu_{\text{cav}} = 100$  MHz and a finesse  $\mathcal{F} = 30$ . The filter has a bandwidth of 370 MHz and a finesse of 70, corresponding to a physical length of 0.6 cm. The bandwidth of the interference filter is 0.3 nm or 120 GHz. It appears to be possible to suppress to a fairly good extent all other modes than the trigger.

trigger photon detector - the count rate will be maximized on resonance.

The filter cavity bandwidth has an impact on the spectral profile of the transmitted trigger photon, which again alters the correlation time between trigger and signal and therefore the length of the prepared single photon. The trigger photon profile after filtering is the product of its original line-shape and the line-shape of the filter cavity. If the filter is broad compared to the photon it has only a weak impact, but if it is of the same order of magnitude, the correlation time is markedly increased [Lu and Ou, 2000]. Thus, to preserve the short signal photons, we should choose a broadband filter cavity, but since the filter should effectively reflect all other modes than the resonant ones, this is in contrast to the demand on the OPO to have a low finesse, that is, with a short relative distance between neighbouring longitudinal modes. A compromise must be found here.

**Single photon counting modules.** To measure single photons we have two avalanche photo diode modules (APDs) of models Perkin-Elmer SPCM-AQR-12 & -13 with a specified quantum efficiency of  $\eta_{\text{qe}} \approx 45\%$  around 860 nm. Even though at first sight this number seems devastating for our attempt to measure single photons with high efficiency, it is far from that critical: in the field (homodyne) measurement, the APD is only used for the trigger, so the quantum efficiency only acts to decrease the preparation rate of signal photons, as given in (6.24). Another more critical parameter of the APDs is the dark count rate  $R_{\text{dark}}$ . Even with no photons impinging on the photodiode, it still “clicks” once in a while as a result of thermal fluctuations in the diode material. It is not possible to distinguish these dark counts from true photon detections. Thus for a proportion of trigger events given by  $R_{\text{dark}}/(R_{\text{sp}} + R_{\text{dark}})$  there will be no signal photon, effectively decreasing the efficiency by a factor of

$$\eta_{\text{dark}} = \frac{R_{\text{sp}}}{R_{\text{sp}} + R_{\text{dark}}} . \quad (6.29)$$

The dark count rate of the detectors is measured to be around  $240 \text{ s}^{-1}$  and  $180 \text{ s}^{-1}$ , respectively. For single photon production/trigger detection rates that will be on the order of  $10^5 \text{ s}^{-1}$  this loss factor is negligible.

The APDs are - by their nature - extremely sensitive to light. They have an advised maximum count rate of  $10^6 \text{ s}^{-1}$ . Therefore, it is crucial to shield them as much as possible from all other light than the down-converted photons. This is done by a housing of cardboard and plastic, and most importantly the narrowband interference filter, placed right in front of the diodes.

For coincidence measurements, the output from the two APDs are collected on an Ortec 9353 time correlation board.

**Local oscillator.** For the homodyne measurement we need a local oscillator which should be mode matched both spatially and temporally with the signal photon on the beamsplitter. This is a quite demanding task - a pulse of a few ns length should hit the beamsplitter at exactly the same time as the photon.

We have ordered a "pulse shaper" that should be able to chop an optical beam into pulses with a rise time of 3-4 ns. It is a Pockels cell which employs the electro-optic effect of a nonlinear crystal to rotate the beam's polarization by  $90^\circ$ , thus letting the light pass a build-in polarizer that otherwise blocks the beam. The polarization rotation requires a field of several kilovolts, and applying such a voltage in a few nanoseconds is on the edge of the technological capabilities. The length of our single photon is in reality determined by the performance of this device.

Another specification of the pulse shaper being a limiting factor is its repetition rate. It does not really matter that we can produce millions of photons per second, when the local oscillator pulses can only be produced with a rate of 50-100 kHz.

A third, very important parameter of the pulse shaper is the extinction ratio - no polarizer is perfect, a small fraction of the local oscillator beam will slip through even when it is turned off. Since our homodyne detectors will have an integration time considerably longer than the duration of the photon, and there will be a weak constant level of the local oscillator, this will give an extra contribution of the vacuum to the detector signal. If the detector integration time is  $t_{\text{det}}$  and the pulse shaper extinction ratio is  $E_{\text{ps}}$ , this gives a loss factor

$$\eta_{\text{LOext}} \approx 1 - E_{\text{ps}} \frac{t_{\text{det}} - \Lambda_{\text{ph}}^\tau}{\Lambda_{\text{ph}}^\tau}. \quad (6.30)$$

The shape of the LO pulse will not fit exactly to the photon shape and this will also lead to a decrease in the temporal mode matching efficiency. This might very well be one of the greatest loss factors in the experiment, but it is hard to anticipate how bad it will be.

Another remark on the local oscillator: To homodyne the signal photon at a frequency  $\nu_{\text{FSR}}$  away from the center frequency, the local oscillator beam should also be shifted with the same amount. This will probably be done by double-pass of an AOM. This actually sets a lower limit to the length of the OPO cavity, since AOMs with a modulation depth higher than  $\sim 1.5 \text{ GHz}$  are hard to get. In double-pass this gives a 3 GHz shift, corresponding to a cavity length of 10 cm.

**Delay line.** To have the local oscillator pulse produced so that it arrives at the beamsplitter at exactly the same time as the signal photon, the trigger APD sends an electronic signal to the pulse shaper upon detection of a trigger photon. At the moment

$t_0$  when the trigger photon fires the APD, half of the signal photon wavepacket is already “in front” of the trigger photon. Since we do not initiate the production of the local oscillator until after  $t_0$ , it will be necessary to have the signal photon delayed while waiting for the LO pulse to be produced. For a photon length of 3 m this is not a problem. What is worse is the electronic delay in the APD (around 10-15 ns) and the pulse shaper (around 30 ns), which lead to a total time delay of up to 50 ns before the LO production initiates. All this while, the signal photon has to be kept on the sideline, waiting for the right time to hit the beamsplitter. This photon delay line should be  $\sim 15$  meters long and will be made up of several passes across the optical table. Such a long optical path with several mirrors will of course have to be extremely stable to keep a good pointing stability and hence spatial mode matching with the local oscillator. This part of the experiment might also prove to be a critical point. Another option would be to couple the photon into an optical fiber, which would be a lot more handy, but unfortunately the coupling efficiencies are not very attractive - 80% is normally attainable, which would be problematic for our attempt to stay well above 50% efficiency.

**Homodyne detectors.** From the discussion above about the local oscillator, it is clear that the detectors used in the homodyne measurement should be very fast, to avoid integrating over long periods with no signal. They should not be too fast, though, since they need to measure the full photon width. In the time-domain photon homodyning, we will not be looking at an optical sideband as in the squeezing experiment, but rather at the full spectrum all the way down to dc, so it will also be necessary to take care of low-frequency electronic noise and to have a flat frequency response over a wide frequency range. Such homodyne detection systems suitable for time-domain analysis of weak fields have already been developed by Hansen et al. [2001] and Zavatta et al. [2002]. Further, the board or instrument for sampling the homodyne data should also be very fast - the total integration time is set by the slowest part of the apparatus.

**Recap.** This section has been a series of rather hand-waving arguments for the various parameters in the setup, in particular the imperfections. Some of them definitely need to be considered in more detail - especially the impact of the various spectral filtering on the photon shape and the spatiotemporal mode matching between the single photon and the classical local oscillator. The latter has been thoroughly studied by Grosshans and Grangier [2001] and Aichele et al. [2002]. However, these two papers are mainly concerned with the standard way of preparing a single photon from a biphoton state, namely via single pass spontaneous parametric down-conversion using a pulsed pump laser. This gives very poorly defined spatial modes of the two (spatially nondegenerate) photons. Spatial filtering in the form of pinholes is then needed, which is qualitatively different from our setup where the photon spatial mode is defined by the OPO cavity. On the other hand, the pulsed down-conversion scheme has the advantage that the local oscillator can be produced directly from the laser pulses, which immediately gives a local oscillator shape closely related to the photon shape. When we have some information on the shape of our local oscillator pulses, we should investigate how to make them resemble the photon shape as well as possible - or conversely, make the photon match the local oscillator, perhaps by a clever choice of filtering.

With regards to the all-important benchmark of overall efficiency of the single

photon preparation and detection, we have estimated very roughly that it should be possible to reach something like  $\eta = 60 - 70\%$ . It is hard to give a more precise estimate as long as we have very little idea about what kind of LO-to-signal mode matching we can achieve. It should be possible, though, to get past the efficiencies measured by other groups doing homodyne tomography on quantum states of light. In the experiment in Konstanz, a total efficiency of 61% was achieved [Lvovsky and Shapiro, 2002, Lvovsky et al., 2001], while an experiment in Florence reached 59% [Zavatta et al., 2004]. Both employed the generation scheme just mentioned, and thus had a poor mode matching (66% in Konstanz), constituting the majority of the experimental losses. With our better defined spatial mode, it should be possible to reach a mode matching on the order of maybe 90%, but we will then have other important loss factors such as the OPO escape efficiency and propagation losses caused by the many needed optical elements (delay line, filter cavity...)

To sum up: With this experiment we expect to accomplish a heralded source of frequency tunable, meter-long photons which can be prepared and measured with a high efficiency, conditioned on the detection of a trigger photon. The source is designed to be compatible with other experiments involving quantum interfaces between light and atoms, but may very well prove to be useful for a variety of other research topics as well - the demand for high quality single photon sources is high.

## Chapter 7

# Summary and outlook

This work presents the path towards the experimental generation of highly interesting nonclassical states of light. We have demonstrated the production of squeezed vacuum and squeezed coherent light states with down to -5 dB of noise suppression via the process of frequency degenerate down-conversion in an optical parametric oscillator operating below threshold. It has further been shown how the directly observed quadrature measurements can be used to reconstruct the full quantum state in the shape of the Wigner function and the density matrix. Finally, it was discussed how the experimental setup can be extended to produce two other, very non-classical light states: EPR-entangled beams, closely related to squeezed light, can be generated by employing the non-degenerate modes of the OPO. The same principle, but with a weakly pumped OPO, is employed to produce correlated pairs of single photons, where the detection of one of them immediately prepares the other in a well-defined spatiotemporal mode.

The immediate utilization of these various non-classical states of light will be as input for the other experiments of the QUANTOP lab dealing with light-atom interfaces using atomic gas samples of different natures: Cesium gas in glass cells at room temperature, cold, trapped cesium atoms and a rubidium BEC (to be). The formalism used to describe all three atomic systems in their interaction with light is essentially the same; the *collective spin* of the atomic sample is considered, and by polarizing all atoms in one direction, the collective spin in this direction has negligible fluctuations and can therefore to a good approximation be replaced by its mean value, while for the two remaining directions the collective spin fluctuates around zero. By rescaling the operators for these two directions, they will behave as standard position and momentum operators, making possible a direct correspondence between the description of the light and of the atoms. Recent years' research has provided evidence that the combination of macroscopic gas samples and multi-photon light pulses constitutes a system well suited for various quantum information tasks within the more general setting of continuous variable quantum information as summarized in the compendium "Quantum Information with Continuous Variables" [Braunstein and Pati, 2003]. In a contribution herein, Kuzmich and Polzik introduce the mentioned physical system and the formalism and review a number of protocols that can be - or have been - implemented. See also Brian Julsgaard's thesis for details [Julsgaard, 2003]. Of the most relevant proposals, Kuzmich and Polzik [2000] devise protocols

for atom-light and atom-atom teleportation, Duan et al. [2000a] show how to entangle atomic ensembles just by using coherent light pulses, Kozhekin et al. [2000] propose a quantum memory for light and Fiurášek et al. [2004] suggest to use such a memory for optimal cloning of coherent light states. On the experimental side, the entanglement between two atomic ensembles was carried out - as already mentioned - by Julsgaard et al. [2001], while the atomic quantum memory was demonstrated recently [Julsgaard et al., 2004] after preliminary “memory” experiments by Hald et al. [1999] and Schori et al. [2002a] employing the squeezed vacuum source. Also, the quantum repeater proposed by Duan et al. [2001] has been partially implemented recently by Matsukevich and Kuzmich [2004].

A quantum memory is meant to be a device able to coherently store and readout any quantum state of light. So far, the memory implemented in the QUANTOP lab has only been proven to work for weak coherent states, and thus it remains to be demonstrated that storage of a nonclassical light state is possible. Squeezed light was recorded, but only in one quadrature, so the full quantum memory of a squeezed state has not been shown yet. A qualitatively different demonstration of the nonclassical capabilities of the memory will be to store one half of a pair of EPR beams, where subsequent measurement should verify that the stored and the un-stored halves are still entangled. The EPR beams are further quite useful for various teleportation schemes [Kuzmich and Polzik, 2000]. For the memories, however, the true test of their applicability as universal quantum memories is whether it is possible to store faithfully the fragile and highly nonclassical single photon state with its non-Gaussian phase space distribution and negativity of the Wigner function. The accomplishment of a reversible storage and readout of a single photon - the natural qubit carrier - will be a demanding task, but could, upon success, truly pave the road towards an operational quantum network architecture.

The major advantage of our nonclassical light sources is the possibility to adopt the output to the other experimental setups of the lab, and we can benefit from having at least two distinctly different atomic systems to interplay with: The room temperature gas cells offer a simple setup with easy access and have proved to be capable of working as a quantum memory. This is thus the natural first place to connect our experiment. However, being at room temperature, the gas is quite dilute (low optical depth), resulting in a weak interaction between light and atoms. Since a certain amount of interaction is necessary, this system requires long optical pulses, which seems to be incompatible with our short photons. The cold, trapped atoms, on the other hand, offer a much higher optical depth and in addition longer coherence time, allowing for longer-lasting storage, but these experiments (cold cesium and rubidium BEC) are not nearly as developed as the gas cell experiment when it comes to the various light-atom interfaces. With time, though, they will certainly also profit from the interaction with our provided light, and, all in all, this promises to lead to substantial progress towards the implementation of a quantum network.

## Appendix A

# Properties of the squeezed states

### Properties of the squeezing operator

The squeezing operator  $\hat{S} \equiv \hat{S}(\zeta) = e^{\frac{1}{2}\zeta^* \hat{a}^2 - \frac{1}{2}\zeta \hat{a}^{\dagger 2}}$  is a unitary operator,  $\hat{S}^\dagger(\zeta) = \hat{S}^{-1}(\zeta) = \hat{S}(-\zeta)$ . As defined in section 2.4.1 with  $\zeta$  negative,  $\zeta = -r e^{i\varphi}$ , the squeezing operator evolves the  $\hat{a}$  and  $\hat{a}^\dagger$  operators into

$$\hat{S}^\dagger \hat{a} \hat{S} = \hat{a} \cosh r + \hat{a}^\dagger e^{i\varphi} \sinh r \quad (\text{A.1})$$

$$\hat{S}^\dagger \hat{a}^\dagger \hat{S} = \hat{a}^\dagger \cosh r + \hat{a} e^{-i\varphi} \sinh r . \quad (\text{A.2})$$

This can be calculated using the *operator expansion theorem* [Mandel and Wolf, 1995, 10.11-1]:

$$e^{x\hat{A}} \hat{B} e^{-x\hat{A}} = \hat{B} + x[\hat{A}, \hat{B}] + \frac{x^2}{2!} [\hat{A}, [\hat{A}, \hat{B}]] + \dots . \quad (\text{A.3})$$

The same formula gives the action of the displacement operator (also unitary)  $\hat{D} \equiv \hat{D}(\alpha)$ :

$$\hat{D}^\dagger \hat{a} \hat{D} = \hat{a} + \alpha \quad (\text{A.4})$$

$$\hat{D}^\dagger \hat{a}^\dagger \hat{D} = \hat{a}^\dagger + \alpha^* . \quad (\text{A.5})$$

### Squeezed state quadrature variance

We wish to calculate the quadrature variance  $\langle (\Delta \hat{q}_\theta)^2 \rangle = \langle \hat{q}_\theta^2 \rangle - \langle \hat{q}_\theta \rangle^2$  of a squeezed state  $|\alpha, \zeta\rangle = \hat{D} \hat{S} |0\rangle$ . We start with the first term of the variance:

$$\begin{aligned} \langle \hat{q}_\theta^2 \rangle &= \langle \alpha, \zeta | \hat{q}_\theta^2 | \alpha, \zeta \rangle \\ &= \frac{1}{2} \langle 0 | \hat{S}^\dagger \hat{D}^\dagger (\hat{a}^2 e^{-2i\theta} + \hat{a}^{\dagger 2} e^{2i\theta} + \hat{a} \hat{a}^\dagger + \hat{a}^\dagger \hat{a}) \hat{D} \hat{S} | 0 \rangle . \end{aligned} \quad (\text{A.6})$$

Looking at the action of the displacement operator on the first term, we use the unitarity of  $\hat{D}$  and (A.4):

$$\begin{aligned} \frac{1}{2} \langle 0 | \hat{S}^\dagger \hat{D}^\dagger \hat{a}^2 e^{-2i\theta} \hat{D} \hat{S} | 0 \rangle &= \frac{1}{2} e^{-2i\theta} \langle 0 | \hat{S}^\dagger \hat{D}^\dagger \hat{a} \hat{D} \hat{D}^\dagger \hat{a} \hat{D} \hat{S} | 0 \rangle \\ &= \frac{1}{2} e^{-2i\theta} \langle 0 | \hat{S}^\dagger (\hat{a} + \alpha) (\hat{a} + \alpha) \hat{S} | 0 \rangle \\ &= \frac{1}{2} e^{-2i\theta} (\langle 0 | \hat{S}^\dagger \hat{a}^2 \hat{S} | 0 \rangle + \alpha^2) . \end{aligned} \quad (\text{A.7})$$

The  $\hat{a}\alpha$  terms vanish in the last line because the squeezing operator only turns them into terms linear in  $\hat{a}$  and  $\hat{a}^\dagger$  which have zero mean value. The other terms in (A.6) act similarly under the displacement operator, so continuing this gives

$$\langle \hat{q}_\theta^2 \rangle = \frac{1}{2} e^{-2i\theta} \langle 0 | \hat{S}^\dagger \hat{a}^2 \hat{S} | 0 \rangle + \frac{1}{2} e^{2i\theta} \langle 0 | \hat{S}^\dagger \hat{a}^{\dagger 2} \hat{S} | 0 \rangle + \langle 0 | \hat{S}^\dagger \hat{a} \hat{a}^\dagger \hat{S} | 0 \rangle - \frac{1}{2} + C , \quad (\text{A.8})$$

where we put  $C = \frac{1}{2} (e^{-2i\theta} \alpha^2 + e^{2i\theta} \alpha^{*2} + 2|\alpha|^2)$  - the contribution from the coherent excitation. We have used the commutator  $[\hat{a}, \hat{a}^\dagger] = 1$ . Using the unitarity of  $\hat{S}$ , this can be written

$$\begin{aligned} \langle \hat{q}_\theta^2 \rangle &= \frac{1}{2} e^{-2i\theta} \langle 0 | \hat{S}^\dagger \hat{a} \hat{S} \hat{S}^\dagger \hat{a} \hat{S} | 0 \rangle + \frac{1}{2} e^{2i\theta} \langle 0 | \hat{S}^\dagger \hat{a}^\dagger \hat{S} \hat{S}^\dagger \hat{a}^\dagger \hat{S} | 0 \rangle \\ &\quad + \langle 0 | \hat{S}^\dagger \hat{a} \hat{S} \hat{S}^\dagger \hat{a}^\dagger \hat{S} | 0 \rangle - \frac{1}{2} + C \end{aligned} \quad (\text{A.9})$$

Using (A.1) and (A.2) and observing that only the  $\hat{a}\hat{a}^\dagger$  terms in the products become non-zero, we get

$$\begin{aligned} \langle \hat{q}_\theta^2 \rangle &= \frac{1}{2} e^{-2i(\theta-\varphi/2)} \cosh r \sinh r + \frac{1}{2} e^{2i(\theta-\varphi/2)} \cosh r \sinh r + \cosh^2 r - \frac{1}{2} + C \\ &= \frac{1}{2} \sinh 2r \cos(2(\theta - \varphi/2)) + \frac{1}{2} \cosh 2r + C , \end{aligned} \quad (\text{A.10})$$

using the trigonometric identities  $\sinh r \cosh r = \frac{1}{2} \sinh 2r$  and  $\cosh^2 r = \frac{1}{2} \cosh 2r + \frac{1}{2}$ .

The second term in the variance is easily calculated to be

$$\langle \hat{q}_\theta \rangle^2 = \frac{1}{2} (\langle 0 | \hat{S}^\dagger \hat{D}^\dagger (\hat{a} e^{-i\theta} + \hat{a}^\dagger e^{i\theta}) \hat{D} \hat{S} | 0 \rangle)^2 = \frac{1}{2} (\alpha e^{-i\theta} + \alpha^{*2} e^{i\theta})^2 = C , \quad (\text{A.11})$$

so that the variance becomes

$$\langle (\Delta \hat{q}_\theta)^2 \rangle = \frac{1}{2} \sinh 2r \cos(2(\theta - \varphi/2)) + \frac{1}{2} \cosh 2r . \quad (\text{A.12})$$

This is the result stated in (2.42). To get from this expression to (2.43) only takes a few trigonometric transformations.

## Photon number expectation value

In terms of the quadrature operators, the number operator can be written

$$\begin{aligned}
 \hat{n} &= \hat{a}^\dagger \hat{a} = \hat{a}^\dagger e^{i\theta} e^{-i\theta} \hat{a} \\
 &= \frac{1}{2} (\hat{q}_\theta - i\hat{q}_{\theta+\pi/2})(\hat{q}_\theta + i\hat{q}_{\theta+\pi/2}) \\
 &= \frac{1}{2} (\hat{q}_\theta^2 + \hat{q}_{\theta+\pi/2}^2 + i[\hat{q}_\theta, \hat{q}_{\theta+\pi/2}]) \\
 &= \frac{1}{2} (\hat{q}_\theta^2 + \hat{q}_{\theta+\pi/2}^2 - 1) .
 \end{aligned} \tag{A.13}$$

The expectation value of the number operator in a squeezed state can now be calculated using (A.10) (including the  $\theta$ -dependent expression for  $C$ ) and setting  $\theta = \varphi/2$ :

$$\begin{aligned}
 \langle \hat{n} \rangle &= \frac{1}{2} (\langle \hat{q}_{\varphi/2}^2 \rangle + \langle \hat{q}_{\varphi/2+\pi/2}^2 \rangle - 1) \\
 &= \frac{1}{2} (\cosh 2r + 2|\alpha|^2 - 1) \\
 &= \sinh^2 r + |\alpha|^2 .
 \end{aligned} \tag{A.14}$$

Thus, the photon number in a squeezed state is  $\sinh^2 r$  higher than for the corresponding coherent state.



## Appendix B

# Various OPO equations

This appendix takes some of the load off the derivation of the output field of the OPO in section 3.2, and should as such be read in connection with that section.

### Rotating frame

The full Hamiltonian for the internal cavity mode of the OPO is

$$\begin{aligned}\hat{H} &= \hat{H}_{\text{free}} + \hat{H}_{\text{int}} \\ &= \hbar\omega_0\hat{a}^\dagger\hat{a} + \frac{i\hbar g}{2}(\beta e^{i\varphi}\hat{a}^{\dagger 2} - \beta^* e^{-i\varphi}\hat{a}^2),\end{aligned}\quad (\text{B.1})$$

with  $\beta = |\beta|e^{-i2\omega_0 t}$ . Inserting this in the Langevin equation (3.18) gives

$$\frac{d\hat{a}}{dt} = -i\omega_0\hat{a} + g\beta e^{i\varphi}\hat{a}^\dagger - (\kappa_1 + \kappa_L)\hat{a} + \sqrt{2\kappa_1}\hat{a}_{\text{in}} + \sqrt{2\kappa_L}\hat{b}_{\text{in}}, \quad (\text{B.2})$$

and similarly for  $\hat{a}^\dagger$ .

The first term on the right hand side corresponds to the very fast optical cycles of the field. We can get rid of that by transforming to a frame rotating at the optical frequency:

$$\hat{a}' = e^{i\omega_0 t}\hat{a}, \quad \hat{a}'^\dagger = e^{-i\omega_0 t}\hat{a}^\dagger, \quad (\text{B.3})$$

For the new rotating frame annihilation operator, the equation of motion becomes

$$\begin{aligned}\frac{d\hat{a}'}{dt} &= i\omega_0 e^{i\omega_0 t}\hat{a} + e^{i\omega_0 t}\frac{d\hat{a}}{dt} \\ &= g|\beta|e^{-i2\omega_0 t}e^{i\varphi}\hat{a}^\dagger e^{i\omega_0 t} - (\kappa_1 + \kappa_L)\hat{a}e^{i\omega_0 t} + \sqrt{2\kappa_1}\hat{a}_{\text{in}}e^{i\omega_0 t} + \sqrt{2\kappa_L}\hat{b}_{\text{in}}e^{i\omega_0 t} \\ &= g|\beta|e^{i\varphi}\hat{a}'^\dagger - (\kappa_1 + \kappa_L)\hat{a}' + \sqrt{2\kappa_1}\hat{a}'_{\text{in}} + \sqrt{2\kappa_L}\hat{b}'_{\text{in}}.\end{aligned}\quad (\text{B.4})$$

### Frequency space commutation relation

For the frequency space annihilation and creation operators,

$$\tilde{a}(\omega) = \frac{1}{\sqrt{2\pi}} \int_{-\infty}^{\infty} e^{i\omega t}\hat{a}(t)dt, \quad \tilde{a}^\dagger(\omega) = \frac{1}{\sqrt{2\pi}} \int_{-\infty}^{\infty} e^{-i\omega t}\hat{a}^\dagger(t)dt, \quad (\text{B.5})$$

the commutation relation is, by direct calculation

$$\begin{aligned}
[\tilde{a}(\omega), \tilde{a}^\dagger(\omega')] &= \frac{1}{2\pi} \int_{-\infty}^{\infty} e^{i\omega t} \hat{a}(t) dt \int_{-\infty}^{\infty} e^{-i\omega' t'} \hat{a}^\dagger(t') dt' \\
&\quad - \frac{1}{2\pi} \int_{-\infty}^{\infty} e^{-i\omega' t'} \hat{a}^\dagger(t') dt' \int_{-\infty}^{\infty} e^{i\omega t} \hat{a}(t) dt \\
&= \frac{1}{2\pi} \int_{-\infty}^{\infty} \int_{-\infty}^{\infty} e^{i(\omega t - \omega' t')} [\hat{a}(t), \hat{a}^\dagger(t')] dt dt' \\
&= \frac{1}{2\pi} \int_{-\infty}^{\infty} e^{i(\omega - \omega')t} dt \\
&= \delta(\omega - \omega').
\end{aligned} \tag{B.6}$$

## Simplified notation for the output field

With the cavity field (3.22) and the input-output relation (3.23), the output field from the OPO becomes

$$\begin{aligned}
\tilde{a}_{\text{out}}(\omega) &= \\
&\frac{1}{(\kappa_1 + \kappa_L - i\omega)^2 - g^2|\beta|^2} \left[ (\kappa_1^2 - (\kappa_L - i\omega)^2 + g^2|\beta|^2) \tilde{a}_{\text{in}}(\omega) + 2\kappa_1 g|\beta| e^{i\varphi} \tilde{a}_{\text{in}}^\dagger(-\omega) \right. \\
&\quad \left. + 2\sqrt{\kappa_1 \kappa_L} (\kappa_1 + \kappa_L - i\omega) \tilde{b}_{\text{in}}(\omega) + 2\sqrt{\kappa_1 \kappa_L} g|\beta| e^{i\varphi} \tilde{b}_{\text{in}}^\dagger(-\omega) \right], \tag{B.7}
\end{aligned}$$

and dividing through everywhere by the square of the total decay rate  $\kappa_1 + \kappa_L$ :

$$\begin{aligned}
\tilde{a}_{\text{out}}(\omega) &= \frac{1}{\left(1 - \frac{i\omega}{\kappa_1 + \kappa_L}\right)^2 - \left(\frac{g|\beta|}{\kappa_1 + \kappa_L}\right)^2} \times \\
&\left\{ \left[ \frac{\kappa_1^2}{(\kappa_1 + \kappa_L)^2} - \left(\frac{\kappa_L - i\omega}{\kappa_1 + \kappa_L}\right)^2 + \frac{g^2|\beta|^2}{(\kappa_1 + \kappa_L)^2} \right] \tilde{a}_{\text{in}}(\omega) \right. \\
&\quad + 2 \frac{\kappa_1}{\kappa_1 + \kappa_L} \frac{g|\beta|}{\kappa_1 + \kappa_L} e^{i\varphi} \tilde{a}_{\text{in}}^\dagger(-\omega) \\
&\quad + 2 \sqrt{\frac{\kappa_1}{\kappa_1 + \kappa_L} \frac{\kappa_L}{\kappa_1 + \kappa_L}} \frac{\kappa_1 + \kappa_L - i\omega}{\kappa_1 + \kappa_L} \tilde{b}_{\text{in}}(\omega) \\
&\quad \left. + 2 \sqrt{\frac{\kappa_1}{\kappa_1 + \kappa_L} \frac{\kappa_L}{\kappa_1 + \kappa_L}} \frac{g|\beta|}{\kappa_1 + \kappa_L} e^{i\varphi} \tilde{b}_{\text{in}}^\dagger(-\omega) \right\}, \tag{B.8}
\end{aligned}$$

and introducing new variables,  $\eta_{\text{esc}} = \kappa_1/(\kappa_1 + \kappa_L)$ ,  $\Omega = \omega/(\kappa_1 + \kappa_L)$ , and  $\epsilon = g|\beta|/(\kappa_1 + \kappa_L)$ :

$$\begin{aligned}
\tilde{a}_{\text{out}}(\omega) &= \frac{1}{(1 - i\Omega)^2 - \epsilon^2} \times \\
&\left\{ [\eta_{\text{esc}}^2 - (1 - \eta_{\text{esc}} - i\Omega)^2 + \epsilon^2] \tilde{a}_{\text{in}}(\omega) + 2\eta_{\text{esc}} \epsilon e^{i\varphi} \tilde{a}_{\text{in}}^\dagger(-\omega) \right. \\
&\quad \left. + 2\sqrt{\eta_{\text{esc}}(1 - \eta_{\text{esc}})} (1 - i\Omega) \tilde{b}_{\text{in}}(\omega) + 2\sqrt{\eta_{\text{esc}}(1 - \eta_{\text{esc}})} \epsilon e^{i\varphi} \tilde{b}_{\text{in}}^\dagger(-\omega) \right\}. \tag{B.9}
\end{aligned}$$

# Bibliography

- T. Aichele, A. I. Lvovsky, and S. Schiller. Optical mode characterization of single photons prepared by means of conditional measurements on a biphoton state. *Eur. Phys. J. D*, 18:237, 2002.
- T. Aoki, N. Takei, H. Yonezawa, K. Wakui, T. Hiraoka, A. Furusawa, and P. van Loock. Experimental creation of a fully inseparable tripartite continuous-variable state. *Phys. Rev. Lett.*, 91:080404, 2003.
- O. Arcizet. Toward the production of an EPR state of light. Research progress report, June 2001.
- A. Arie. Quasi-phase-matched nonlinear frequency conversion. Lecture notes, Q&NLO2004 Ph.D School at the Technical University of Denmark, Sept. 2004.
- J. A. Armstrong, N. Bloembergen, J. Ducuing, and P. S. Pershan. Interactions between light waves in a nonlinear dielectric. *Phys. Rev.*, 127(6):1918, 1962.
- A. Aspect, P. Grangier, and G. Roger. Experimental realization of Einstein-Podolsky-Rosen-Bohm gedankenexperiment: A new violation of Bell's inequalities. *Phys. Rev. Lett.*, 49:91, 1982.
- H.-A. Bachor and T. C. Ralph. *A guide to experiments in quantum optics*. WILEY-VCH Verlag GmbH & Co. KGaA, 2. edition, 2004.
- J. S. Bell. *Speakable and unspeakable in quantum mechanics*. Cambridge University Press, 1987.
- C. H. Bennett, G. Brassard, C. Crépeau, R. Jozsa, A. Peres, and W. K. Wootters. Teleporting an unknown quantum state via dual classical and Einstein-Podolski-Rosen channels. *Phys. Rev. Lett.*, 70:1895, 1993.
- C. H. Bennett and D. P. DiVincenzo. Quantum information and computation. *Nature*, 404:247, 2000.
- J. Bertrand and P. Bertrand. A tomographic approach to Wigner's function. *Found. Phys.*, 17:397, 1987.
- G. C. Bjorklund, M. D. Levenson, W. Lenth, and C. Ortiz. Frequency modulation (FM) spectroscopy. *Appl. Phys. B*, 32:145, 1983.
- D. Bouwmeester, J.-W. Pan, M. Daniell, H. Weinfurter, and A. Zeilinger. Observation of three-photon Greenberger-Horne-Zeilinger entanglement. *Phys. Rev. Lett.*, 82:1345, 1999.

- D. Bouwmeester, J.-W. Pan, K. Mattle, M. Eibl, H. Weinfurter, and A. Zeilinger. Experimental quantum teleportation. *Nature*, 390:575, 1997.
- W. P. Bowen, N. Treps, R. Schnabel, and P. K. Lam. Experimental demonstration of continuous variable polarization entanglement. *Phys. Rev. Lett.*, 89:253601, 2002.
- G. D. Boyd and D. A. Kleinman. Parametric interaction of focused Gaussian light beams. *J. Appl. Phys.*, 39(8):3597, 1968.
- S. L. Braunstein and A. K. Pati, editors. *Quantum information with continuous variables*. Kluwer Academic Press, 2003.
- S. L. Braunstein and P. van Loock. Quantum information with continuous variables. arXiv:quant-ph/0410100v1, 2004.
- G. Breitenbach. *Quantum state reconstruction of classical and nonclassical light and a cryogenic opto-mechanical sensor for high-precision interferometry*. PhD thesis, Universität Konstanz, 1998. URL <http://www.ub.uni-konstanz.de/kops/volltexte/1999/227/>.
- G. Breitenbach, S. Schiller, and J. Mlynek. Measurement of the quantum states of squeezed light. *Nature*, 387:471, 1997.
- H.-J. Briegel, W. Dür, J. I. Cirac, and P. Zoller. Quantum repeaters: The role of imperfect local operations in quantum communication. *Phys. Rev. Lett.*, 81:5932, 1998.
- P. Buchhave. Parametric amplification. Lecture notes, Q&NLO2004 Ph.D School at the Technical University of Denmark, Sept. 2004.
- K. E. Cahill and R. J. Glauber. Density operators and quasiprobability distributions. *Phys. Rev.*, 177:1882, 1969.
- H. J. Carmichael. Spectrum of squeezing and photocurrent shot noise: A normally ordered treatment. *J. Opt. Soc. Am. B*, 4(10):1588, 1987.
- J. I. Cirac, P. Zoller, H. J. Kimble, and H. Mabuchi. Quantum state transfer and entanglement distribution among distant nodes in a quantum network. *Phys. Rev. Lett.*, 78:3221, 1997.
- M. J. Collett and C. W. Gardiner. Squeezing of intracavity and traveling-wave light fields produced in parametric amplification. *Phys. Rev. A*, 30(3):1386, 1984.
- G. M. D'Ariano, C. Macchiavello, and M. G. A. Paris. Detection of the density matrix through optical homodyne tomography without filtered back projection. *Phys. Rev. A*, 50(5):4298, 1994.
- V. G. Dmitriev, G. G. Gurzadyan, and D. N. Nikogosyan. *Handbook of nonlinear optical crystals*. Springer series in optical sciences. Springer, 2. edition, 1997.
- R. W. P. Drever, J. L. Hall, F. V. Kowalski, J. Hough, G. M. Ford, A. J. Munley, and H. Ward. Laser phase and frequency stabilization using an optical resonator. *Appl. Phys. B*, 31:97, 1983.
- L.-M. Duan, J. I. Cirac, P. Zoller, and E. S. Polzik. Quantum communication between atomic ensembles using coherent light. *Phys. Rev. Lett.*, 85:5643, 2000a.

- L.-M. Duan, G. Giedke, J. I. Cirac, and P. Zoller. Inseparability criterion for continuous variable systems. *Phys. Rev. Lett.*, 84:2722, 2000b.
- L.-M. Duan, M. D. Lukin, J. I. Cirac, and P. Zoller. Long-distance quantum communication with atomic ensembles and linear optics. *Nature*, 414:413, 2001.
- A. Einstein, B. Podolsky, and N. Rosen. Can quantum-mechanical description of physical reality be considered complete? *Phys. Rev.*, 47:777, 1935.
- J. Fiurášek, N. J. Cerf, and E. S. Polzik. Quantum cloning of a coherent light state into an atomic quantum memory. *Phys. Rev. Lett.*, 93:180501, 2004.
- S. J. Freedman and J. F. Clauser. Experimental test of local hidden-variable theories. *Phys. Rev. Lett.*, 28:938, 1972.
- A. Furusawa, J. L. Sørensen, S. L. Braunstein, C. A. Fuchs, H. J. Kimble, and E. S. Polzik. Unconditional quantum teleportation. *Science*, 282:706, 1998.
- D. J. Griffiths. *Introduction to electrodynamics*. Prentice Hall, 3. edition, 1999.
- F. Grosshans and P. Grangier. Effective quantum efficiency in the pulsed homodyne detection of a  $n$ -photon state. *Eur. Phys. J. D*, 14:119, 2001.
- E. Hagley, X. Maître, G. Nogues, C. Wunderlich, M. Brune, J. M. Raimond, and S. Haroche. Generation of Einstein-Podolsky-Rosen pairs of atoms. *Phys. Rev. Lett.*, 79:1, 1997.
- J. Hald, J. L. Sørensen, C. Schori, and E. S. Polzik. Spin squeezed atoms: A macroscopic entangled ensemble created by light. *Phys. Rev. Lett.*, 83:1319, 1999.
- K. Hammerer, K. Mølmer, E. S. Polzik, and J. I. Cirac. Light-matter quantum interface. *Phys. Rev. A*, 70:044304, 2004.
- H. Hansen, T. Aichele, C. Hettich, P. Lodahl, A. I. Lvovsky, J. Mlynek, and S. Schiller. Ultrasensitive pulsed, balanced homodyne detector: application to time-domain quantum measurements. *Opt. Lett.*, 26:1714, 2001.
- R. W. Henry and S. C. Glotzer. A squeezed-state primer. *Am. J. Phys.*, 56:318, 1988.
- B. Julsgaard. *Entanglement and quantum interactions with macroscopic gas samples*. PhD thesis, University of Aarhus, Oct. 2003. URL [http://quantop.nbi.dk/thesis/thesis\\_brian.ps.gz](http://quantop.nbi.dk/thesis/thesis_brian.ps.gz).
- B. Julsgaard, A. Kozhekin, and E. S. Polzik. Experimental long-lived entanglement of two macroscopic objects. *Nature*, 413:400, 2001.
- B. Julsgaard, J. Sherson, J. I. Cirac, J. Fiurášek, and E. S. Polzik. Experimental demonstration of quantum memory for light. *Nature*, 432:483, 2004.
- E. Knill, R. Laflamme, and G. J. Milburn. A scheme for efficient quantum computation with linear optics. *Nature*, 409:46, 2001.
- A. E. Kozhekin, K. Mølmer, and E. Polzik. Quantum memory for light. *Phys. Rev. A*, 62:033809, 2000.

- A. Kuhn, M. Hennrich, and G. Rempe. Deterministic single-photon source for distributed quantum networking. *Phys. Rev. Lett.*, 89:067901, 2002.
- A. Kuzmich and E. S. Polzik. Atomic quantum state teleportation and swapping. *Phys. Rev. Lett.*, 85:5639, 2000.
- P. G. Kwiat, K. Mattle, H. Weinfurter, A. Zeilinger, A. V. Sergienko, and Y. Shih. New high-intensity source of polarization-entangled photon pairs. *Phys. Rev. Lett.*, 75:4337, 1995.
- P. K. Lam. *Applications of quantum electro-optic control and squeezed light*. PhD thesis, Australian National University, 1998. URL <http://eprints.anu.edu.au/archive/00002619/>.
- P. K. Lam, T. C. Ralph, B. C. Buchler, D. E. McClelland, H.-A. Bachor, and J. Gao. Optimization and transfer of vacuum squeezing from an optical parametric oscillator. *J. Opt. B: Quantum Semiclass. Opt.*, 1:469, 1999.
- L. Leick. The construction of a tisapph laser and the use hereof in measurements on a Cs MOT. Master's thesis, University of Aarhus, 1998.
- U. Leonhardt. *Measuring the quantum state of light*. Cambridge University Press, 1997.
- U. Leonhardt, M. Munroe, T. Kiss, Th. Richter, and M. G. Raymer. Sampling of photon statistics and density matrix using homodyne detection. *Opt. Comm.*, 127:144, 1996.
- Y. J. Lu and Z. Y. Ou. Optical parametric oscillator far below threshold: Experiment versus theory. *Phys. Rev. A*, 62:033804, 2000.
- A. D. Ludlow, H. M. Nelson, and S. D. Bergeson. Two-photon absorption in potassium niobate. *J. Opt. Soc. Am. B*, 18(12):1813, 2001.
- N. Lütkenhaus and S. M. Barnett. Nonclassical effects in phase space. *Phys. Rev. A*, 51(4):3340, 1995.
- A. I. Lvovsky, H. Hansen, T. Aichele, O. Benson, J. Mlynek, and S. Schiller. Quantum state reconstruction of the single-photon Fock state. *Phys. Rev. Lett.*, 87(5):050402-1, 2001.
- A. I. Lvovsky and J. H. Shapiro. Nonclassical character of statistical mixtures of the single-photon and vacuum optical states. *Phys. Rev. A*, 65:033830, 2002.
- H. Mabuchi, E. S. Polzik, and H. J. Kimble. Blue-light-induced infrared absorption in  $\text{KNbO}_3$ . *J. Opt. Soc. Am. B*, 11(10):2023, 1994.
- L. Mandel and E. Wolf. *Optical coherence and quantum optics*. Cambridge University Press, 1995.
- D. N. Matsukevich and A. Kuzmich. Quantum state transfer between matter and light. *Science*, 306:663, 2004.
- G. Milburn and D. F. Walls. Production of squeezed states in a degenerate parametric amplifier. *Optics. Comm.*, 39(6):401, 1981.
- P. W. Milonni and J. H. Eberly. *Lasers*. John Wiley & Sons, Inc., 1988.

- B. R. Mollow and R. J. Glauber. Quantum theory of parametric amplification. II. *Phys. Rev.*, 160:1097, 1967.
- C. Monroe. Quantum information processing with atoms and photons. *Nature*, 416:238, 2002.
- C. Monroe, D. M. Meekhof, B. E. King, and D. J. Wineland. A “schrödinger cat” superposition state of an atom. *Science*, 272:1131, 1996.
- M. Oberparleiter. *Effiziente Erzeugung verschränkter Photonenpaare*. PhD thesis, Ludwig-Maximilians-Universität München, Aug. 2002. URL <http://scotty.quantum.physik.uni-muenchen.de/publ/>.
- Z. Y. Ou, C. K. Hong, and L. Mandel. Coherence properties of squeezed light and the degree of squeezing. *J. Opt. Soc. Am. B*, 4(10):1574, 1987.
- Z. Y. Ou, S. F. Pereira, H. J. Kimble, and K. C. Peng. Realization of the Einstein-Podolsky-Rosen paradox for continuous variables. *Phys. Rev. Lett.*, 68:3663, 1992.
- E. S. Polzik, J. Carri, and H. J. Kimble. Spectroscopy with squeezed light. *Phys. Rev. Lett.*, 68:3020, 1992.
- E. S. Polzik and H. J. Kimble. Frequency doubling with  $\text{KNbO}_3$  in an external cavity. *Opt. Lett.*, 16(18):1400, 1991.
- E. S. Polzik, J. L. Sørensen, and J. Hald. Subthreshold tunable OPO: a source of non-classical light for atomic physics experiments. *Appl. Phys. B*, 66:759, 1998.
- M. D. Reid. Demonstration of the Einstein-Podolsky-Rosen paradox using nondegenerate parametric amplification. *Phys. Rev. A*, 40(2):913, 1989.
- M. D. Reid and P. D. Drummond. Quantum correlations of phase in nondegenerate parametric oscillation. *Phys. Rev. Lett.*, 60:2731, 1988.
- H. Risken. *The Fokker-Planck equation: Methods of solution and applications*. Springer, 2. edition, 1989.
- J. J. Sakurai. *Modern quantum mechanics*. Addison-Wesley, 1994.
- B. E. A. Saleh and M. C. Teich. *Fundamentals of photonics*. John Wiley & Sons, Inc., 1991.
- C. Santori, D. Fattal, J. Vučković, G. S. Solomon, and Y. Yamamoto. Indistinguishable photons from a single-photon device. *Nature*, 419:594, 2002.
- C. Schori. *Frequency tunable light source of continuous quadrature entanglement*. PhD thesis, University of Aarhus, Sept. 2002.
- C. Schori, B. Julsgaard, J. L. Sørensen, and E. S. Polzik. Recording quantum properties of light in a long-lived atomic spin state: Towards quantum memory. *Phys. Rev. Lett.*, 89:057903, 2002a.
- C. Schori, J. L. Sørensen, and E. S. Polzik. Narrow-band frequency tunable light source of continuous quadrature entanglement. *Phys. Rev. A*, 66(3):033802, 2002b.
- M. O. Scully and M. S. Zubairy. *Quantum optics*. Cambridge University Press, 1997.

- L. Shiv, J. L. Sørensen, E. S. Polzik, and G. Mizell. Inhibited light-induced absorption in  $\text{KNbO}_3$ . *Opt. Lett.*, 20(22):2270, 1995.
- R. E. Slusher, L. W. Hollberg, B. Yurke, J. C. Mertz, and J. F. Valley. Observation of squeezed states generated by four-wave mixing in an optical cavity. *Phys. Rev. Lett.*, 55:2409, 1985.
- D. T. Smithey, M. Beck, M. G. Raymer, and A. Faridani. Measurement of the Wigner distribution and the density matrix of a light mode using optical homodyne tomography: Application to squeezed states and the vacuum. *Phys. Rev. Lett.*, 70(9):1244, 1993.
- J. L. Sørensen. *Nonclassical light for atomic physics and quantum teleportation*. PhD thesis, University of Aarhus, Sept. 1998.
- J. L. Sørensen, J. Hald, N. Jørgensen, J. Erland, and E. S. Polzik. Squeezing with  $\chi^{(2)}$  for atomic physics and spectroscopy. *Quantum Semiclass. Opt.*, 9:239, 1997.
- M. R. Spiegel and J. Liu. *Mathematical handbook of formulas and tables*. Schaum's Outlines. McGraw-Hill, 2. edition, 1999.
- D. Stoler. Equivalence classes of minimum uncertainty packets. *Phys. Rev. D*, 1:3217, 1970.
- Q. A. Turchette, C. S. Wood, B. E. King, C. J. Myatt, D. Leibfried, W. M. Itano, C. Monroe, and D. J. Wineland. Deterministic entanglement of two trapped ions. *Phys. Rev. Lett.*, 81:3631, 1998.
- P. van Loock and S. L. Braunstein. Multipartite entanglement for continuous variables: A quantum teleportation network. *Phys. Rev. Lett.*, 84:3482, 2000.
- K. Vogel and H. Risken. Determination of quasiprobability distributions in terms of probability distributions for the rotated quadrature phase. *Phys. Rev. A*, 40(5):2847, 1989.
- R. F. Werner. Quantum states with Einstein-Podolsky-Rosen correlations admitting a hidden-variable model. *Phys. Rev. A*, 40(8):4277, 1989.
- E. Wigner. On the quantum correction for thermodynamic equilibrium. *Physical Review*, 40:749, 1932.
- L.-A. Wu, H. H. Kimble, J. L. Hall, and H. Wu. Generation of squeezed states by parametric down conversion. *Phys. Rev. Lett.*, 57:2520, 1986.
- H. Yonezawa, T. Aoki, and A. Furusawa. Demonstration of a quantum teleportation network for continuous variables. *Nature*, 431:430, 2004.
- H. C. Yuen and J. H. Shapiro. Generation and detection of two-photon coherent states in degenerate four-wave mixing. *Opt. Lett.*, 4:334, 1979.
- H. P. Yuen. Two-photon coherent states of the radiation field. *Phys. Rev. A*, 13:2226, 1976.
- H. P. Yuen and V. W. S. Chan. Noise in homodyne and heterodyne detection. *Opt. Lett.*, 8(3):177, 1983.

- B. Yurke. Use of cavities in squeezed-state generation. *Phys. Rev. A*, 29(1):408, 1984.
- A. Zavatta, M. Bellini, P. L. Ramazza, F. Marin, and F. T. Arecchi. Time-domain analysis of quantum states of light: noise characterization and homodyne tomography. *J. Opt. Soc. Am. B*, 19:1189, 2002.
- A. Zavatta, S. Viciani, and M. Bellini. Quantum-to-classical transition with single-photon-added coherent states of light. *Science*, 306:660, 2004.